Chapter 6
Feedback Control Designs

A. Schirrer, M. Kozek, F. Demourant and G. Ferreres

6.1 Introduction

A. Schirrer and M. Kozek

6.1.1 General Properties of Feedback Control

The general concept of feedback control is characterized by utilizing system output signals (measurements) to determine the control signal, thus closing a control loop by a feedback interconnection. For linear systems, this generally alters the system's eigendynamics, and this is in fact the central feature that feedback systems possess in contrast to feed-forward (input-shaping) concepts. Consequently, the main conceptual goals of feedback control concepts for linear dynamic systems are the following:

Stabilization: If stabilizability conditions are met, unstable systems can be stabilized by a suitable control law when the control loop is closed.
Shaping of the eigendynamics: The system's eigendynamics can be altered in terms of a shift of eigenvalues and/or a change of the eigenvectors, which corresponds for example, to changing system time constants or to decoupling responses.
Increase robustness: Feedback control has the potential to decrease the effects of unknown model errors or perturbations or unknown disturbances to the system's responses. This is commonly known as *disturbance rejection*. As an example, a feedback controller could achieve accurate tracking of reference signals even

A. Schirrer (✉) · M. Kozek
Vienna University of Technology, Vienna, Austria
e-mail: alexander.schirrer@tuwien.ac.at

F. Demourant · G. Ferreres
ONERA-Toulouse, Toulouse, France

M. Kozek and A. Schirrer (eds.), *Modeling and Control for a Blended Wing Body Aircraft*,
Advances in Industrial Control, DOI 10.1007/978-3-319-10792-9_6

though the system gain may be uncertain or disturbance input signals unknown to the controller. A purely feed-forward input-shaping concept cannot address these uncertainties by design.

Note, however, that these properties can also produce disadvantages because a feedback controller could also destabilize an otherwise stable system, for example, if critical model errors occur and if the feedback control law is not suitable under these conditions. Thus, the design of a feedback controller requires in-depth system analysis, design tuning, and validation to ensure that the critical requirements (stability, signal magnitude bounds, validity region of the model) are also met in reality.

Additionally, feedback control can address time- and frequency-domain specifications (rise time, overshoot, bandwidth, response magnitudes), which can also be affected by feed-forward concepts. Depending on the application and on the available design methods, the control engineer needs to be decide on the most efficient concept(s) to address these requirements. Often, a combination of methods which exploits their benefits yields high-performance, modular solutions.

6.1.2 Feedback Design Methods in the Flight Control Context

Flexible aircraft control is subject of broad research (see for example [41, 46, 48, 90], or [92]) and it bears the potential of additional weight savings and thus increased fuel efficiency. Novel concepts in civil aviation such as BWB aircraft introduce numerous new challenges to this class of multiobjective control design problems (see [57]): potential (cross-)coupling of longitudinal and lateral motion (and low-frequency flexible modes), possible open-loop instability, as well as high-performance demands in loads alleviation, vibration reduction, and maneuver shaping.

This chapter presents several state-of-the-art feedback flight control design methods for the lateral as well as the longitudinal dynamics of the considered large, flexible BWB transport aircraft model. Numerous stringent constraints and goals are given in terms of eigendynamic requirements and specifications in the time and frequency domains. The considered design methods typically address a subset of the design specifications given in Chap. 5. The control performance is validated and discussed for each approach. The following design methods are considered:

- Partial eigenstructure assignment (ACFA 2020 BWB configuration, lateral control, see Sect. 6.2).
- μ synthesis via DGK-iteration based on a parametrized linear fractional transformation (LFT) model (ACFA 2020 BWB configuration, lateral control, see Sect. 6.3).
- Convex control design via the Youla parametrization and a parametrized observer (ACFA 2020 BWB configuration, longitudinal control, see Sect. 6.4).
- Linear parameter-varying (LPV) feedback control design by a linear matrix inequality (LMI) approach (ACFA 2020 BWB configuration, longitudinal control, see Sect. 6.5).

- Structured low-order $\mathscr{H}_\infty$ design (NACRE BWB lateral control in Sects. 6.6.1–6.6.3; ACFA 2020 BWB longitudinal control in Sect. 6.6.4).

Partial eigenstructure assignment is utilized as an initial controller for the lateral control task (see robust modal control design [54, 73]) to achieve some of the lateral control goals most efficiently addressed by eigenstructure assignment, including basic damping of flexible modes. Based on this pre-shaping, the linear fractional representations (LFRs) of the parametrized, pre-shaped aircraft dynamics are obtained as shown in Sect. 4.2 and a μ synthesis design is carried out to maximize robust damping performance for the relevant flexible modes by exploiting the structured change of system dynamics as functions of the physical parameters.

The longitudinal control task is addressed by convex controller synthesis, which starts out from an linear quadratic Gaussian (LQG)-controlled plant in which rigid-body (RB) requirements are addressed. The observer-based realization is directly suited to put the system into a Youla-parametrized form, that is, to express closed-loop transfers affinely in the Youla controller parameter. A convex optimization problem for heterogenous time- and frequency-domain objectives and constraints can now be formulated and solved efficiently. Finally, the plant model within the observer is parametrized, yielding a globally LPV control law. The controller achieves high performance in terms of handling qualities, critical loads, and comfort.

Next, longitudinal control is once again addressed, however, via a direct design of an LPV controller for an LPV plant description. After a thorough open-loop analysis, the design weighting functions are prepared and optimized by considering a series of standard $\mathscr{H}_\infty$ designs at fixed parameter values. This also allows to directly tune robustness of the controller family. Then these design data are utilized in a direct LPV control design to obtain an optimized LPV controller. This allows to consider parameter rate of change bounds and to exploit the structure of the parameter dependency already in the control design and yields excellent performance in validation.

Finally, both lateral and longitudinal control tasks are addressed in the investigation of design methods of $\mathscr{H}_\infty$ and $\mathscr{H}_2/\mathscr{H}_\infty$ controllers with prescribed controller structure and (arbitrarily) low dynamic order. The involved optimization problems are generally difficult to solve (non-smooth, non-convex). However, well-performing results could be achieved via the $\mathscr{H}_\infty$ fixed-order optimization toolbox ($\mathscr{H}_\infty$ fixed-order optimization) in MATLAB®. These designs have been developed for the NACRE BWB configuration (lateral design) and for the ACFA BWB configuration (longitudinal design).

The multitude of control design studies in this context yields the important conclusion that multistage design approaches that combine the benefits of several different design methods allow to address a multitude of heterogenous specifications efficiently. These composite control concepts typically contain feedback control laws, but also complementary feed-forward controller blocks to address command shaping or (measurable) disturbance compensation. These concepts are often referred to as *two degrees of freedom control architecture*. Here, several such concepts have been developed:

- Design of a lateral comprehensive load alleviation control system as a combination of eigenstructure assignment, robust $\mathscr{H}_\infty$-control feedback design and a scheduled feed-forward command shaper.
- Design of a longitudinal gust loads alleviation by LQG pre-shaping and convex controller synthesis.
- Design of a longitudinal comprehensive load alleviation control concept combining $\mathscr{H}_\infty$ designs/LPV feedback control design with an $\mathscr{H}_\infty$ full-information feed-forward concept.

6.1.3 State of the Art

Flight and structural control laws are commonly built using optimal or robust control design methods to maximize control performance also in the presence of plant uncertainties. The DK-iteration and more recently the DGK-iteration or mixed-μ-synthesis are well-known design tools to generate robust control laws when the plant's uncertainty or possible perturbations can be modeled well by structured uncertainties [5, 76, 95].

An additional, central challenge for a control engineer is to translate the given specifications efficiently and effectively into design parameters for the utilized synthesis methods (usually from optimal or robust control). Typically, these constraints are either stated as weighting functions in the frequency-domain ($\mathscr{H}_\infty/\mathscr{H}_2$ control, DK-iterations) or as objective function weightings (as in linear quadratic (LQ) control). One design method with the capability of considering both time- and frequency-domain constraints and objectives at the same time is convex synthesis.

Convex design for the control of conventional flexible aircraft has been studied, among others, in the PhD thesis of [20] as well as by [64] (with subsequent controller order reduction), and [84] (a self-scheduling approach). In robust control applications, robust stability (RS) of the closed loop is usually the most fundamental requirement. One additional, important requirement for reliable control is the stability of the controller itself (referred to as strong stabilization, see for example [45, 86]), which is not guaranteed by standard optimal and robust design methods. This is however imperative in the case of potential actuator or sensor faults, and simple tuning often does not suffice to obtain stable controllers.

Convex synthesis of a feedback controller using the Youla parameterization has been designed based on the large 750-passenger NACRE BWB aircraft predesign model in [72]. An linear matrix inequality (LMI) formulation is taken to optimize directly for the time- and frequency-domain goals not addressed by the initial controller. A heuristic algorithm to achieve strong stabilization is proposed and allows to obtain a stable feedback law which is validated successfully on all considered parameter cases (mass cases). High control performance is achieved, including direct time-domain specifications.

A general integrated methodology for multiobjective robust control design has been presented in [69]. Previous, closely related studies have been carried out on the

large 750-passenger NACRE BWB aircraft predesign model: for LQ-based lateral control designs see [70], the application of a genetic algorithm for parameter optimization of a multiobjective $\mathscr{H}_\infty$ DK-iteration design has been treated in [71]. Using a Youla parameterization of the feedback control loop, a convex controller synthesis for lateral BWB control has been performed in [73] with a subsequent scheduled feed-forward control design in [72]. Longitudinal BWB control using LPV control concepts has been studied in [89]. All these works investigate control designs on the large 750-passenger NACRE BWB aircraft predesign model and represent the early results achieved in the ACFA 2020 project.

The subsequent feedback control designs reported in this chapter have initially been published in the following papers: the lateral designs in Sects. 6.2 and 6.3 are adopted from [74], the longitudinal convex synthesis design in Sect. 6.4 has been shown in [24], and the LPV feedback design approach in Sect. 6.4 is detailed in [88]. Finally, the structured longitudinal design in Sect. 6.6.4 has been published in [42].

6.2 Robust Eigenstructure Assignment

A. Schirrer and M. Kozek

6.2.1 Methodology

Methods of robust eigenstructure assignment extend classical pole placement control design in several ways [54]: First, only a partial eigenstructure assignment of a few, relevant system poles to desired closed-loop positions is possible. The remaining system poles will generally be shifted slightly as well, but this can be met by an iterative design procedure. The advantage is that no artificial design requirements (for example, pole pinning) need to be introduced, and that the remaining degrees of freedom can be utilized to improve insensitivity to model errors. Also, no full state vector estimation may be necessary and methods exist to derive only those elementary estimates necessary to perform the partial assignment, yielding low-complexity dynamic output feedback controllers.

In the following, an initial controller in the form of an output feedback control law is designed by robust eigenstructure assignment using the techniques and tools given in [54].

Given a state-space system $\mathbf{P}$ as in (5.15) and (5.16) (subscript i omitted for brevity), q triplets $(\lambda_i, \boldsymbol{v}_i, \boldsymbol{w}_i)$ (eigenvalue, input, and output directions, respectively) are assigned in closed loop (with $q \leq p$ where p is the number of measurements). Let $\mathbf{X} = \mathbf{CV} + \mathbf{DW}$, $\mathbf{V} = [\boldsymbol{v}_1, \ldots, \boldsymbol{v}_q]$, and $\mathbf{W} = [\boldsymbol{w}_1, \ldots, \boldsymbol{w}_q]$ hold. The output feedback gain to assign the given eigenstructure is

$$\mathbf{K} = \mathbf{W}\mathbf{X}^{\dagger} \tag{6.1}$$

where the pseudo-inverse $(\cdot)^{\dagger}$ of $\mathbf{X}$ yields the norm-minimal feedback gain for $q < p$. If $q = p$ and $\mathbf{X}$ is non-singular, the inverse of $\mathbf{X}$ can be used instead.

6.2.2 Control Goals

The specific control goals for this lateral inner-loop control design are a subset of the goals in Table 5.4:

1. stabilize the aircraft,
2. obtain high damping $\zeta \geq 0.7$ of the Dutch Roll mode (DR mode) while keeping the mode's undamped eigenfrequency unchanged,
3. obtain sufficiently fast real/aperiodic remaining system dynamics to fulfill rise-time requirements on roll/side-slip responses in 7 and 5 s, respectively, and
4. improve damping of the first flexible mode.

Note that in the present setting, goal 1 also includes a significant shift of the spiral mode's pole to the left which otherwise is realized by an outer (auto-)pilot control loop.

These requirements all have to be fulfilled robustly for all 30 considered parameter cases in the viewed parameter space. They will all be addressed, as far as possible, by the control law which is designed through robust/insensitive eigenstructure assignment.

6.2.3 Feedback Control Design

To fulfill the listed control goals, an initial controller is designed by robust partial eigenstructure assignment (utilizing the MATLAB® Robust Modal Control Toolbox supplied with the book [54]). This is done in two steps:

1. Assign low-frequency (rigid-body) dynamics using low-pass output feedback,
2. Increase the damping of high-frequency flexible modes via a bandpass-filtered output feedback through eigenvector projection.

For step 1, an input/output (I/O)- and state-reduced RB model was extracted from the design ROMs at a chosen parameter case:

- Input reduction to 1 combined rudder command and 1 combined anti-symmetric command on flaps 3 and 4 ("inner" and "middle" ailerons). This was chosen because flaps 3, 4 do not reverse their effect on the aircraft over the envelope and they are fast enough for RB control.

- Output reduction to measurements of β (side-slip angle), φ (roll angle), p (roll rate), and r (yaw rate).
- State reduction by truncation of all flexible modes and lag states, leaving only states β (side-slip angle), p (roll rate), r (yaw rate), φ (roll angle), and the rudder- and flap 3, 4 second-order dynamics. The actuator dynamics of flaps 3 and 4 were modeled by a single filter because they behave sufficiently similarly.
- Augmentation of each of the 4 measurements by a fourth-order dynamics (second-order Padé approximation of 160 ms delay and a second-order low-pass filter).

The relevant plant open-loop poles lie close to the respective poles of the full-order model. The RB poles can be identified as a low-damped (in some parameter cases unstable) DR mode (frequency between 0.7 and 1 rad/s), a marginally stable or unstable real spiral mode and a stable real pole at around -2. The desired DR pole location is obtained by increasing its damping ζ to $\sqrt{2}/2$ with constant frequency.

The DR mode damping requirement and the decoupling specifications (and partially the performance specifications) are cast into eigenstructure constraints, see [54]:

$$p_{\text{rig,des},1} = -0.6 \qquad v_1 = [0, *, 0, *, \ldots]^{\mathrm{T}} \tag{6.2}$$

$$p_{\text{rig,des},2,3} = p_{\text{DR,des},1,2} \qquad v_{2,3} = [*, 0, *, 0, \ldots]^{\mathrm{T}} \tag{6.3}$$

$$p_{\text{rig,des},4} = -1.3 \qquad v_4 = [0, *, 0, *, \ldots]^{\mathrm{T}}, \tag{6.4}$$

where the remaining eigenvector elements (marked by $*$ in (6.2)–(6.4)) are unconstrained. The computed feedback gain robustly assigns a high DR mode damping. The loop is closed with the resulting static output feedback law, and this shaped plant comprises the design plant for step 2.

Design step 2 aims to increase the damping of the first (low-damped) flexible mode at around 10 rad/s. The controller takes the modal measurement $Nz_{\text{lat.law}}$ and generates a combined flap 3, 4 and a separately actuated flap 5 control signal. In order to obtain enough degrees of freedom to shift the two flexible mode (complex-conjugated) poles, a first-order observer is necessary. The mentioned toolbox offers a robust observer design method for this task. The observation dynamics is chosen real and near the relevant modes' frequency at $p_{\text{obs}} = -10$. After such observer is synthesized, a static output feedback gain is computed to shift the flexible mode poles to the left. Hence, they are reassigned at the location

$$p_{\text{flex,desired},1,2} = p_{\text{flex,actual},1,2} - 0.5 \tag{6.5}$$

using a minimal-energy criterion, yielding a Bode magnitude peak reduction of about 6 dB in the closed-loop transfer path from lateral gust to $Nz_{\text{lat.law}}$.

The final partial eigenstructure assignment controller is combined into a single linear time-invariant (LTI) system of first order, 3 outputs (combined flap 3, 4; flap 5; rudder), and 5 inputs (measurements of side-slip angle, roll angle, roll rate, yaw rate, and $Nz_{\text{lat.law}}$) and is successfully validated on all fuel and center of gravity (CG)

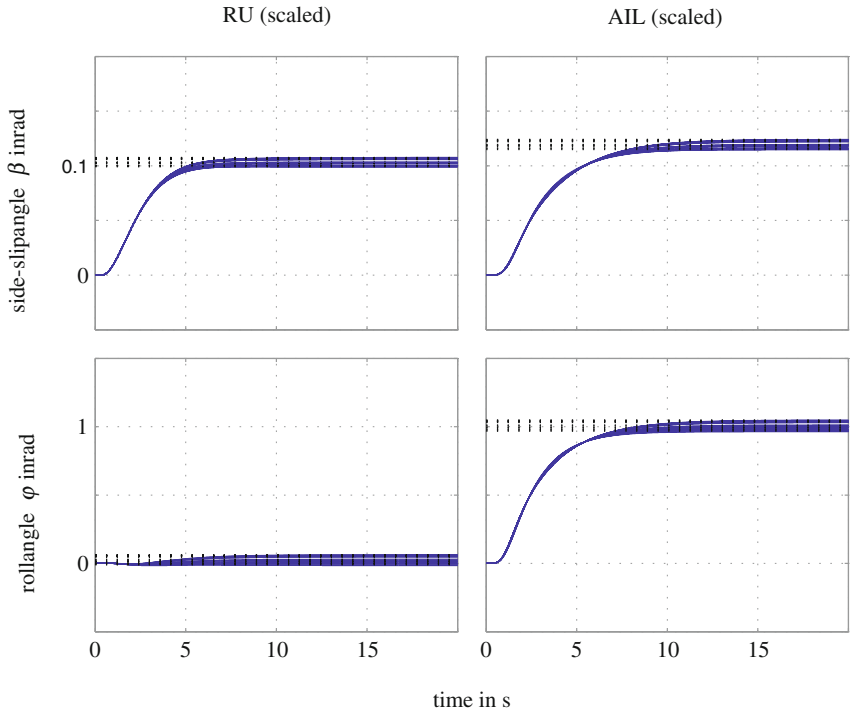

Fig. 6.1 Step responses of the pre-shaped plants from rudder and ailerons to side-slip and roll angles at random CG and fuel parameter values

parameter cases of the design flight condition (fixed Mach and dynamic pressure case).

6.2.4 Basic Feed-Forward Decoupling Design

For basic pilot input shaping, a simple feed-forward control law of PT1-structure is synthesized that

- maximizes decoupling of the two reference signals (roll reference φ_{ref} and side-slip reference β_{ref}) and
- ensures that rate limits on the control surface inputs are obeyed for the test maneuvers ($-30° \rightarrow +30°$ roll reference step, $0 \rightarrow 0.1$ rad side-slip reference step).

This is solved by a linear programing (LP) problem that directly shapes the feed-forward controller coefficients to optimize decoupling Decouplingover all fuel and CG cases and a suitable choice of the PT1 time constants.

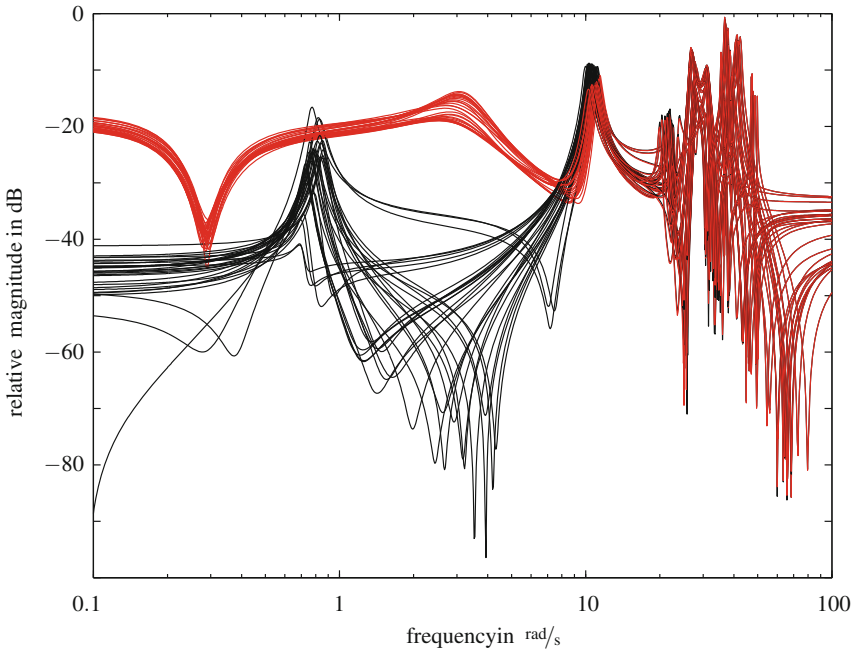

Fig. 6.2 Bode magnitude plot of gust-wing cut moment for all mass cases (*black* open loop; *red* closed loop with initial controller)

6.2.5 Initial Control Law Validation

Figures 6.1 and 6.2 validate the performance of the designed initial control law for all CG and fuel cases for the high-speed central flight case (cruise conditions). Figure 6.1 shows that the closed-loop validation step responses fulfill the required RB specifications robustly. Moreover, the aircraft is robustly stabilized, and the damping ratios of the DR mode and the first flexible (wing bending) modes are increased as shown in Fig. 6.2, but also an overall increase in the low-frequency magnitude of the disturbance-loads transfer becomes evident. The first flexible mode can be robustly attenuated by about 6 dB in all CG/fuel cases with this simple control law.

Further studies on the issue of the increased low-frequency disturbance-load magnitude shows that this effect mainly occurs at parameter configurations far from the design point. When solely assigning one aircraft mode to the desired location while keeping the others fixed at their open-loop locations, it is unveiled that shifting the roll mode and the flexible mode does not affect low-frequency loads; however, both DR mode shaping as well as shifting the spiral mode are responsible to a similar degree to the observed increase in loads. Further optimization of the low-frequency disturbance behavior of the aircraft is not studied in this work, but represents an interesting area for follow-up studies.

6.3 DK-Iteration Design

A. Schirrer and M. Kozek

6.3.1 Methodology

Based on the pre-shaped plant obtained by closing the loop with the initial controller from Sect. 6.2, a parameterized high-accuracy parameterized linear fractional representation (LFR) is built (see Sect. 4.2.3.3), which serves as basis for robust feedback control design by DGK-iteration [74]. Due to high-dimensional parameter dependency and loose bounds in current μ analysis tools, this synthesis task faces computational difficulties given today's workstation computing performance and numeric properties of the algorithms. Thus, ways to reduce design complexity and improve resulting robust control performance are tested and assessed in terms of performance, robustness, tractability, and problem size. A high-accuracy parametric LFR as well as various simplified LFR formulations are utilized in subsequent design attempts.

6.3.1.1 Initial Controller

The output feedback controller $\mathbf{K}_{\text{init}}$ of dynamic order 1 is obtained as shown in Sect. 6.2. The initial controller is interconnected to the aircraft system models, forming a set of pre-shaped plants (each of dynamic order 48). As described in Sect. 6.2.5, this initial controller achieves a robust reduction of the first anti-symmetric wing bending mode amplitude by about 6 dB. Note that it is not possible to directly and robustly increase flexible mode damping further with the eigenstructure assignment design methodology.

6.3.1.2 Linear Fractional Representation of the Parametrized, Pre-shaped Plants

By exploiting the structure of the parameter dependency of the plant, the damping of the first flexible modes is attempted to be further increased, without altering the other already satisfied control goals (RB response, stability). Therefore, an LFR description of this set of pre-shaped plants in the two parameters CG and fuel filling has been generated from the model grid (5.15) and (5.16) and validated by the authors' project partners analogous to the procedure in [43], see Sect. 4.2.3.3. The lag states were removed for the LFR generation. A first, high-accuracy LFR has been generated which has 41 states and a Δ block size of 40 $\times$ 40 (in which the two real-valued

parameters are 9 and 31 times repeated, respectively). Later, due to computational difficulties with this level of complexity, a simplified parameterization has been generated which leads to a reduced-accuracy LFR with 33 states and a 13×13 Δ block (8 and 5 times repeated, respectively).

Figure 6.1 shows scaled, typical step responses (as modeled by the high-accuracy LFR) for several randomly sampled parameter values. The RB response is considered satisfactorily shaped by the initial controller.

6.3.2 Control Goals

In addition to the initial control law designed in Sect. 5.4, a lateral inner-loop control design should be carried out to are:

1. retain the achieved goals from Table 5.4 (stabilization, RB control), and
2. maximize damping of the first two flexible modes.

Note that the initial control law already provides vibration damping functionality; however, further improvement of the vibration damping performance (goal 2) is possible only when exploiting knowledge on the parameter dependency. Thus, the μ synthesis method (via the D(G)K-iteration algorithm) is employed to address this goal.

6.3.3 Control Design

DGK-iteration is employed with the aim to generate a robust controller that fulfills the targeted control goals: to attenuate the first and second flexible modes, and thus reduce the gust-induced wing loads. For details on the involved robust control theory, fundamental definitions of linear fractional transforms/representation (LFTs/LFRs), the structured singular value (μ), robust stability (RS), robust performance (RP), or the DK- and DGK-iteration algorithms, the reader is referred to [5, 37, 76, 95].

The control design architecture for control design via DGK-iteration is outlined in Fig. 6.3 (left). The system LFR $\mathbf{G}_{\text{LFR}}$ is augmented by the design weights $\mathbf{W}_{\text{a}}$, $\mathbf{W}_{\boldsymbol{n}}$, $\mathbf{W}_{\boldsymbol{u}}$, and $\mathbf{W}_z$ to obtain the augmented plant $\mathbf{G}_{\text{aug}}$, and $\mathbf{K}$ is the robust feedback LTI controller to be designed. The modeled signals are disturbance input $d = v_{\text{lat}}$, feedback control commands $\boldsymbol{u} = [u_{\text{RU,FB}}, u_{\text{TE12,FB}}, u_{\text{TE3,FB}}]^{\text{T}}$, the performance outputs $\boldsymbol{z} = [My_{\text{wing}}, Nz_{\text{lat.law}}]^{\text{T}}$, the measured outputs $\boldsymbol{y} = [\beta, \phi, p, r, Nz_{\text{lat.law}}]^{\text{T}}$ with measurement noise $\boldsymbol{n}$, as well as the weighted output signals $\boldsymbol{z_u}$ and $\boldsymbol{z_p}$. The measurement noise weighted $\mathbf{W}_n$ and the additive uncertainty weight $\mathbf{W}_{\text{a}}$ serve as problem regularization terms and are chosen small and constant. The remaining weights are chosen with the aim to

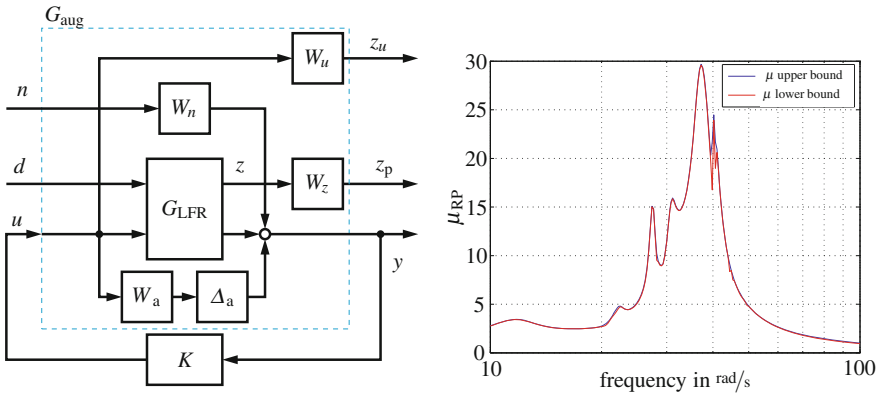

Fig. 6.3 Design architecture for DGK-iteration (*left*), robust performance (RP) μ analysis results (*right*)

- ensure well-scaled I/O magnitudes (via scaling inside $\mathbf{G}_{\text{LFR}}$),
- emphasize the first and second wing bending modes in the performance path (via $\mathbf{W}_z$), and to
- limit the control input magnitudes to the admissible input range (via $\mathbf{W}_u$).

6.3.3.1 DGK-Design Attempt with High-Accuracy LFR

The results of a DGK-iteration run based on the high-accuracy LFR are shown in Fig. 6.3 (right). The RP μ value is much larger than 1 at all considered frequencies—it is clearly evident that the closed loop fails to achieve satisfactory control performance. In further studies, it becomes evident that the bounds of the open-loop robust stability (RS) μ value are very loose. This problem of convergence and the resulting conservativeness in the **D**- and **G**-scalings yield unsatisfactory results of the design. Note that only static scalings could be utilized in DGK-iteration design due to the problem size: The $\boldsymbol{\Delta}$-block contains $40 \times 40 = 1{,}600$ entries. Fitting these with dynamic **G**- and **D**-scalings inflates the controller order quickly well above 1,000 which is numerically and computationally infeasible.

One common heuristics to improve mixed-μ convergence is to add small, complex uncertainties to the existing real uncertainties. This was attempted first, however no improvement in μ bound convergence could be observed.

To overcome the encountered computational difficulties, two simplification approaches will be taken and compared in the following.

6.3.3.2 DGK-Design Attempt with AdHoc Uncertainty Model

Based on the observation that the perturbations of the flexible mode parameters are the main source of uncertainty, an adhoc uncertainty parameterization is attempted

(see [8, 90, 95] for similar attempts). The aircraft models are close to a modal form [36] in which a low-damped flexible mode is represented by a 2×2 submatrix of the system matrix $\boldsymbol{A}$:

$$\boldsymbol{A}_{\mathrm{m}i} = \begin{bmatrix} 0 & 1 \\ -\omega_i^2 & -2\zeta_i\omega_i \end{bmatrix}. \tag{6.6}$$

By replacing the (2, 1) and (2, 2) matrix elements with real-valued uncertain parameters which are confined to the intervals occurring across the model set, an efficient uncertainty representation with a small uncertainty matrix $\boldsymbol{\Delta}$ of size 2×2 per mode is obtained. Note that no other variations in the plant are considered, hence the uncertainty model is rather crude. The architecture shown in Fig. 6.3 is reused, but the plant LFR is replaced by its simplified version (with a $\boldsymbol{\Delta}$-block of 4×4). The achieved RP μ value is 2.7.

The obtained controller is of dynamic order 117 (due to dynamic D- and G-scalings) after few minutes of computation time on a standard office PC. This controller complexity is in general too high for implementation, so controller order reduction is needed subsequently.

Figure 6.4 shows the performance singular values of the open- and closed-loop systems with the validation plants. An input turbulence model according to a 1D von-Kármán vertical turbulence model has been utilized to include information on the expected low-pass characteristics of turbulence excitation, assuming that a similar turbulence characteristics can be observed in a lateral direction. It is evident that for most models the obtained controller performs well and achieves strong attenuation (about -7 dB) of the first and second flexible modes. However, in two (extremal) parameter cases, the second flexible mode of the respective validation plant is destabilized. No simple means are available to ensure stability with these plants except for enlarging the uncertainty ranges, which quickly destroys the obtained nominal performance.

6.3.3.3 DGK-Design with Reduced-Accuracy LFR

In order to obtain a computationally manageable problem size, but still to obtain a robustly stabilizing and performing control law, a reduced-accuracy parameterized LFR has been generated. The weight shapes are chosen as depicted in Fig. 6.5 to emphasize the control effect on the first flexible mode. After several design iterations, it became clear that the large variation of the second flexible mode is a limiting factor in the design—therefore, the weightings are adapted to avoid control action at the second flexible mode's frequency range.

Figure 6.6 shows the unweighted and the weighted performance singular values of the unweighted (scaled) LFR and of the weighted design plant, randomly sampled in the uncertain set. The effect of the chosen weightings is clearly visible—the strongly

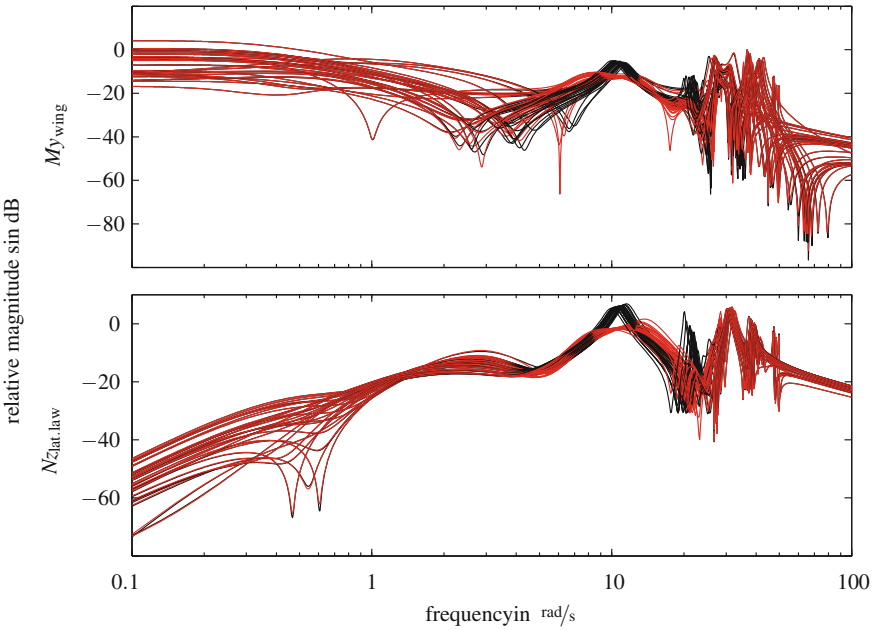

Fig. 6.4 Bode magnitude plots of von-Kármán low-pass filtered lateral wind v_{lat} to wing cut moment My_{wing} and anti-symmetric wingtip acceleration signal $Nz_{\text{lat.law}}$ for all mass cases. *Black* Pre-shaped design plant; *red* closed loop with robust controller, obtained by DGK-iteration on a simplified design LFR

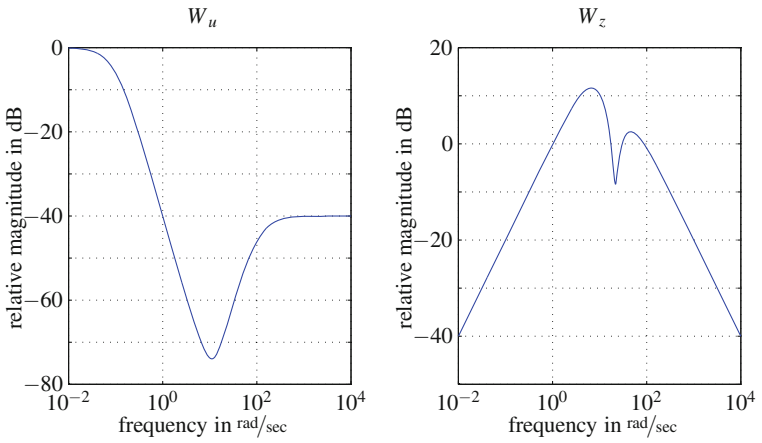

Fig. 6.5 Weight shapes of $\mathbf{W}_u$ (*left*) and $\mathbf{W}_z$ (*right*) the control action is focused on the first wing bending mode (notch in $\mathbf{W}_u$, peak in $\mathbf{W}_z$). Additionally, the 2nd flexible mode must be attenuated in the performance path to obtain RP

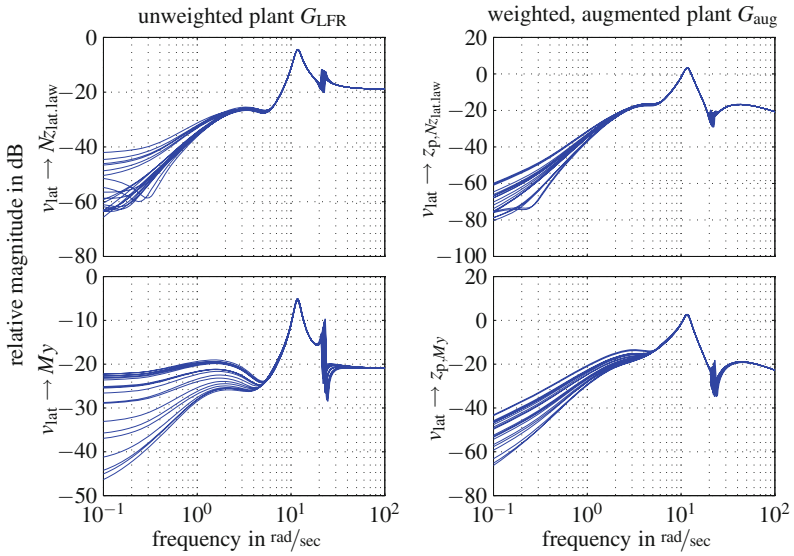

Fig. 6.6 Scaled, unweighted (*left*), and weighted (*right*) magnitude plot of lateral gust—performance outputs as modeled by the reduced-complexity LFR, sampled at 20 random parameter points

varying second mode is decreased in importance; the control design task focuses on the first flexible mode.

After the DGK-iteration run (20 iterations, **D**- and **G**-scalings up to order 4, grid of 284 frequencies, augmented design plant $\mathbf{P}_{\mathrm{aug}}$ of order 59, 135 min computation time), an RP μ of 1.44 is obtained (as compared to an open-loop RP μ of 2.0), which is still larger than 1, but, as shown in Fig. 6.7, the RS μ value is less than 1. The figure shows also the nominal performance singular values (single weighted load performance outputs and all outputs combined) of the nominal closed loop **M** and thus shows the closed-loop system variation bounds as gap between the nominal singular values and the RP μ bound. The controller dynamic order is very high with 253 states. For implementation, (robust) controller order reduction must be performed, see [21] for a μ-based approach. The high-order control law can be reduced by the `reduce` command of MATLAB® [5] with the option `'ErrorType','mult'` to order 30 virtually without performance loss. The underlying algorithm is a balanced stochastic model truncation (BST) via Schur's method [67].

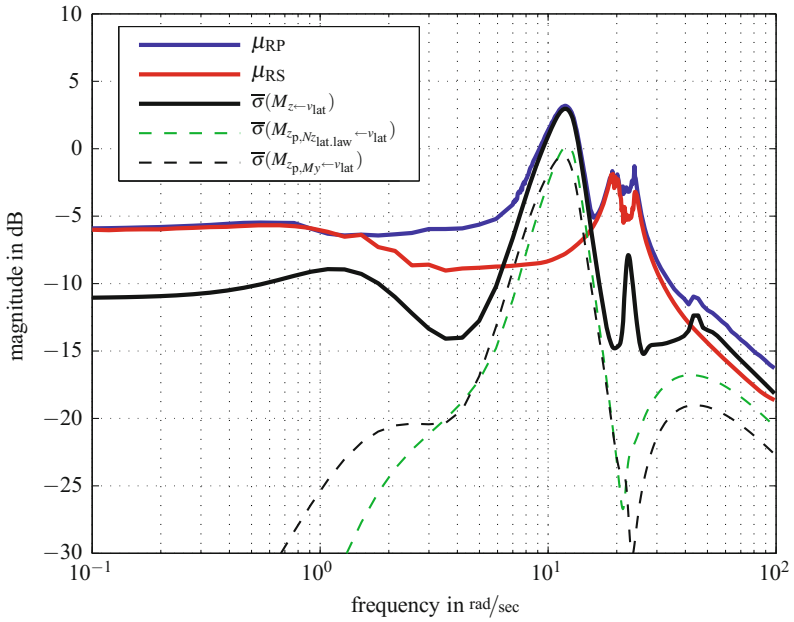

Fig. 6.7 Nominal performance singular values and μ upper bounds for RP and RS

6.3.4 Validation and Discussion

6.3.4.1 Validation of Control Performance and Robustness

The control law obtained in Sect. 6.3.3.3 is validated with all grid models (5.15) and (5.16). All closed-loop systems are stable. While the μ analysis results in Fig. 6.7 proves RS for the utilized LFR formulation of the problem (up to LFR approximation errors), this enumeration of the set of all closed-loop systems proves RS in terms of the provided model set.

Figure 6.8 shows the magnitude plots of the disturbance—performance paths: the first flexible mode can robustly be reduced to 2–3 dB below the level provided by the initial control law. Note that this does not contradict the evident lack of RP in the LFR sense (which is based on the performance formulation according to Fig. 6.3).

The controller obtained by DGK-iteration does not interfere with low-frequency roll and side-slip behavior of the BWB aircraft, so the final closed-loop responses are virtually unchanged compared to Fig. 6.1 and control goals 2 and 3 in Sect. 6.2 remain fulfilled.

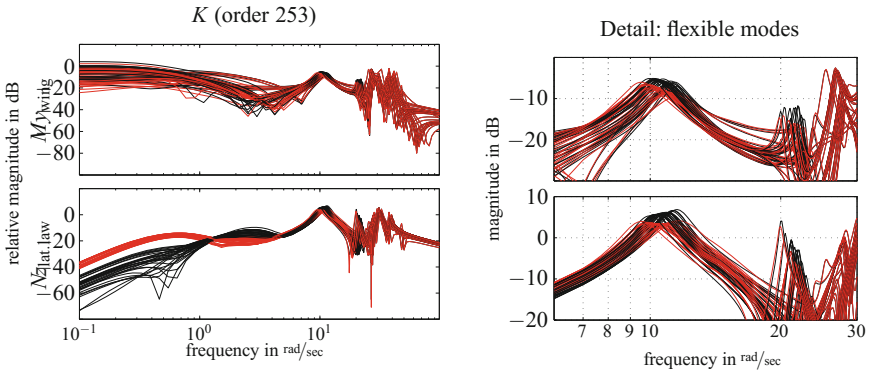

Fig. 6.8 Bode magnitude plots of von-Kármán low-pass filtered lateral wind v_{lat} to the wing cut moment My_{wing} and to the anti-symmetric wingtip acceleration signal $Nz_{\text{lat.law}}$ for all mass cases. *Black* Aircraft model with initial control law only; *Red* closed loop with initial controller and robust controller, obtained by DGK-iteration with the reduced-accuracy design LFR

6.3.4.2 Discussion

A highly detailed modeling process yields accurate system models for a parameter grid of relevant system parameters. For high parameterization accuracy, the obtained parameterized linear fractional representation turns out to be prohibitively complex for current μ analysis and synthesis algorithms. Several ways to solve the design task have been attempted, including well-known problem regularization techniques ("complexification" of the uncertainty description) and simplification of the linear fractional representation.

Adhoc uncertainty modeling yields simple LFRs and high control performance for the design plant, but it destabilizes some parameter-extremal validation plant cases in closed loop. No straightforward remedy is found without compromising control performance significantly.

Subsequently, a reduced-accuracy parameterized LFR is generated which leads to a successful, albeit computationally demanding design. The obtained control law can be reduced to order 30 without performance degradation and yields stable closed loops with all validation cases. Its performance is significantly lower than the nominal performance achieved through the adhoc approach, but in turn it provides an actually robust solution. Considering that significant damping is already introduced by the initial control law it is plausible that further improvement comes at high cost—both in terms of design complexity and numeric complexity of the control law.

As an outlook to possible future research, several other approaches could be attempted in such high-complexity designs. To meet the numeric challenges associated with μ bounds calculation, especially in the present case where a low number of parameters is repeated often, it seems reasonable to attempt numeric search methods to empirically find improved μ bounds. Also, μ computation algorithms without the need of fine frequency gridding could alleviate the encountered difficulties [34].

This study considers only the lateral motion of the BWB aircraft which is decoupled from the longitudinal motion as long as the deviation of the flight mechanic variables remain sufficiently close to trimmed level flight conditions and the linearized system models remain valid. However, even without longitudinal/lateral coupling in the underlying system models, it is important to simulate both dynamics simultaneously in order to verify that control surface deflection/rate limitations are obeyed also in combined maneuvers (such as in coordinated turns).

In conclusion, the findings of this work underline the importance of efficient LFR modeling for DK-/DGK-iteration-based control design. The encountered challenges demonstrate the need for algorithms which allow to generate efficient LFRs whose parameterization accuracy is optimized for the envisaged control task, for example through frequency-weighted error minimization.

6.3.4.3 Conclusions

This section presents results for an incremental robust feedback control design of a lateral inner-loop control law for the 450-passenger ACFA BWB aircraft predesign model. Starting with an initial control law that already provides basic response shaping and flexible mode damping, the main design goal of this work is to further increase the damping of the flexible modes robustly despite the presence of strong parameter-dependent plant variation. The DGK-iteration synthesis procedure is utilized and several LFR formulations of the aircraft model parameter dependency are tested. The highest-complexity attempt involving a high-accuracy parametric LFR cannot be handled computationally. A simple, manual adhoc uncertainty formulation leads to quick results with high nominal performance but fails to provide robustness in validation. Finally, a reduced-accuracy parametric LFR is utilized which leads to a computationally demanding design, but yields a control law that robustly stabilizes and attenuates the flexible dynamics above the level provided by the initial control law. High-fidelity validation studies of these control laws via simulations are necessary at a later stage of control design in order to quantify the effects of model uncertainties and errors as well as longitudinal and lateral coupling.

6.4 Convex Synthesis Design

F. Demourant, G. Ferreres and A. Schirrer

6.4.1 Introduction

Numerous requirements are to be fulfilled to control a flexible aircraft. The corresponding specifications can be very different: handling qualities, load alleviation in the frequency- and/or time-domain representations, command effort including saturation and rate limiters, comfort and robustness [23, 33, 84]. To meet these

different kinds of specifications the Youla parameter design, namely the convex synthesis [12] is involved. This approach is very interesting for several reasons. All stabilizing controllers can be parametrized thanks to the Youla parameter and the closed-loop transfer functions are affine with respect to the Youla parameter. Then all specifications that correspond to constraints on closed-loop transfer functions can be rewritten as convex optimization problem. Finally, the problem solved is convex which guarantees the globality of the optimum found and good tractability of the optimization algorithm. This last point is all the more important in that a specific property of a flexible aircraft is the high dynamic order of the models. In brief, the convex synthesis is clearly a multiobjective/multicriterion control law design approach.

The second important point is to ensure achieving the required performance level for the full flight domain and different mass/fuel cases. This point leads to schedule a control law with measurable parameters which impact the behavior of the aircraft. An useful representation to make the Youla parameter appear naturally is the estimated state feedback structure. By this representation, a natural LPV controller is obtained since a parametrized model is embedded in the observer. A typical parametrization is an LFR of the model to control, whereby the Δ block contains scheduling parameters. Let us point out two important points. Firstly, it is not necessary to schedule the observer and state gains and/or the Youla parameter if the closed-loop behavior is satisfactory. Secondly, the LFR, which can be difficult to determine with high-order models and/or numerous scheduling/robustness parameters [83], is one possible representation, but other parametrizations such as a polynomial parametrization, can be used for the observer.

The studied control design task for the flexible ACFA BWB aircraft is aimed at 3 sets of specifications. The first set of specifications concerns the handling qualities, that is, the behavior of the aircraft with pilot and flight control law. Thereby, it is important to note that it is not expected that all handling qualities specifications are satisfied by the feedback. If the feedback design is considered satisfactory, it is possible and necessary to use a feed-forward control law to shape time-domain responses in order to fully meet handling qualities specifications. The second set of specifications concerns the load alleviation in critical load outputs. Typically, the main objective is to decrease the load level for the wing root bending moment (WRMX) under the constraint to satisfy actuators saturations and rate limiters and not to increase the wing root vertical force (WRFz). The last specification set concerns the improvement of passenger comfort. Here, this specification is formulated as reduction of the $\mathscr{H}_2$ norm of cabin accelerations.

For the rigid part, an LQG methodology is involved. This methodology is very interesting in our context because it makes the structure of the estimated state feedback appear naturally. Of course, from theoretical point of view, any dynamic feedback output can be put under an estimated state-feedback form [1]. However, this additional step is not straightforward to carry out and can lead, in the context of an LPV control law, to controllers which are not interpolable with a suitable behavior. Results obtained in terms of closed-loop pole placement and time-domain simulations are satisfactory without scheduling observer and state gains. Still, this controller is an LPV controller due to the fact that the observer is parametrized. This controller

represents the initial stabilizing LPV controller. Now the Youla parameter is designed to meet specification on the flexible part. Finally, the load alleviation, which is the main objective, is obtained while satisfying constraints on WRFz and actuators together with a comfort improvement. Finally, after the feedback has been synthesized, a feed-forward is designed to satisfy handling qualities specifications completely.

The results of this control design strategy are taken from [24].

6.4.2 Methodology

A convex representation of the feedback control design problem is obtained via the Youla parameterization [94]. This allows one to express closed-loop transfer functions affinely in basis functions of the Youla parameter and thus allows direct convex optimization of closed-loop time- or frequency-domain responses. This so-called convex synthesis [12, 20], as a Youla-parameter-based technique, is similar to the $\mathscr{H}_\infty$ synthesis in the sense that it allows to weigh closed-loop transfer matrices. Additionally, mixed frequency- and time-domain constraints or objectives ($\mathscr{H}_\infty$, $\mathscr{L}_\infty$, $\mathscr{H}_2$, etc.) can be considered simultaneously. However, closed-loop plant poles become immobile under this parametrization, so an initial stabilizing controller is required which already has to produce a well-placed closed-loop plant pole structure.

6.4.2.1 Affinity of Closed-Loop Transfer Functions

Let us consider the classical standard form where $\mathbf{y}(t)$ and $\boldsymbol{u}(t)$ are the inputs/outputs of the control law and $\boldsymbol{w}(t)$ and $\boldsymbol{z}(t)$ are the closed-loop inputs/outputs to control. Typically, $\boldsymbol{w}(t)$ are reference inputs, measure noise and non-measured perturbations. Outputs $\boldsymbol{z}(t)$ represent any closed-loop weighted signals which must be controlled by the control law. $\mathbf{P}(s)$ represents the synthesis model with weighting functions and $\mathbf{K}_0$ represents an available control law. Two hypothesizes are necessary to use of convex synthesis methodology:

- the transfer matrix $\mathbf{P}(s)$ should be proper;
- the initial controller $\mathbf{K}_0$ should ensure closed-loop stability.

Let us split transfer matrix $\mathbf{P}$ in the following way:

$$\mathbf{P} = \begin{bmatrix} \mathbf{P}_{11} & \mathbf{P}_{12} \\ \mathbf{P}_{21} & \mathbf{P}_{22} \end{bmatrix} \tag{6.7}$$

It is possible to write the transfer matrix between $\boldsymbol{w}$ and $\boldsymbol{z}$ as a function of $\mathbf{P}$ and any controller $\mathbf{K}$ by the lower linear fractional transformation $\mathscr{F}_l(\mathbf{P}, \mathbf{K})$:

$$\mathbf{T}_{w\to z} = \mathscr{F}_l(\mathbf{P}, \mathbf{K}) = \mathbf{P}_{11} + \mathbf{P}_{12}\mathbf{K}(\mathrm{I} - \mathbf{P}_{22}\mathbf{K})^{-1}\mathbf{P}_{21} \tag{6.8}$$

In our synthesis problem, it is necessary to write the set of time- and frequency-domain specifications under mathematical criteria. For instance, frequency-domain specifications can be written as the minimization of $\gamma_{i,j}$ under the frequency-domain constraint:

$$\| \mathbf{T}_{w_i \to z_j}(j\omega) \|_\infty \leq \gamma_{i,j} \Leftrightarrow \| \mathscr{F}_1(\mathbf{P}, \mathbf{K})_{i,j} \|_\infty \leq \gamma_{i,j} \tag{6.9}$$

The problem is to determine the control law $\mathbf{K}$ which satisfies specifications (6.9), which is deeply nonlinear in $\mathbf{K}$. We will now show that the Q-parameterization allows to express the closed-loop constraints as a linear expression in $\mathbf{Q}$:

$$\mathscr{F}_1(\mathbf{P}, \mathbf{K}) = \mathbf{T}_1 - \mathbf{T}_2 \mathbf{Q} \mathbf{T}_3 \tag{6.10}$$

where $\mathbf{Q}$ becomes the synthesis parameter and $\mathbf{T}_1$, $\mathbf{T}_2$ and $\mathbf{T}_3$ contain the poles of the initial closed-loop system. In fact, the Q-parameterization allows to substitute $\mathbf{Q}$ to $\mathbf{K}$ to make the optimization problem convex. The Q-parameterization allows to describe all the $\mathbf{K}(s)$ which stabilize the closed loop: if a control law satisfying the specifications exists then it is possible to find it by optimizing the $\mathbf{Q}$ parameter.

We have shown that the closed-loop transfer matrix is affine in $\mathbf{Q}$ for an (LFT). $\mathbf{Q}$ can be parameterized as follows:

$$\mathbf{Q} = \sum_{i=1}^{n} \theta_i \mathbf{Q}_i \tag{6.11}$$

$\mathbf{Q}_i$ are filters whose poles are determined a priori and θ_i are optimization parameters. The set of these filters is a base which is used to build $\mathbf{Q}$. Then the (LFT) can be written in the following way:

$$\mathscr{F}_1(\mathbf{P}, \mathbf{K}) = \mathbf{T}_1 - \sum_{i=1}^{n} \theta_i \mathbf{T}_2 \mathbf{Q}_i \mathbf{T}_3 \tag{6.12}$$

Let us assume $\mathbf{F}_{l_0} = \mathbf{T}_1$ and $\mathbf{F}_{l_i} = -\mathbf{T}_2 \mathbf{Q}_i \mathbf{T}_3$, we obtain:

$$\mathscr{F}_1(\mathbf{P}, \mathbf{K}) = \mathbf{F}_{l_0} + \sum_{i=1}^{n} \mathbf{F}_{l_i} \theta_i = \mathbf{F}_{l_0} + \mathbf{F}^t \Theta \tag{6.13}$$

where the closed-loop transfer matrix is affine in Θ, vector of the decomposition of $\mathbf{Q}$ over the base. We can show that frequency- and time-domain responses are also affine in Θ. The problem can then be efficiently solved with the cutting-planes method.

6.4.2.2 Choice of a Base

To choose a base for Q comes down to determine poles. Is important to note that poles of filters are poles of the final closed loop by property of Q-parameterization. In the field of system identification, numerous studies exist about the generation of these bases. Theoretically, an infinite number of base elements is needed, but as the control law order depends on the base order, a base which order is compatible with specifications is chosen. An orthonormal base is used, called Takenaka and Malmquist base, which combines properties of Laguerre and Kautz base. The decomposition of $Q_i(s)$ is given by (6.14).

$$Q_i(s) = \frac{\sqrt{2\,\mathrm{Re}(a_i)}}{s + a_i} \prod_{k=1}^{i-1} \frac{s - \overline{a_k}}{s + a_k}, \quad Q_0(s) = 1, \quad a_k \in \mathbb{C}^+ \tag{6.14}$$

where a_k are the filters poles and are determined a priori to cover the frequency domain of the bandwidth, and $Q = \sum_{i=1}^{N} \theta_i Q_i$.

6.4.2.3 A Structure for the Youla Parameter

One method to obtain a Youla parametrization is to design an initial stabilizing observer-based state feedback which is a posteriori augmented with the inputs $\boldsymbol{e}$ and outputs $\boldsymbol{v}$ of $\mathbf{Q}(s)$:

$$\begin{aligned} \dot{\hat{\mathbf{x}}} &= \mathbf{A}\hat{\mathbf{x}} + \mathbf{B}\boldsymbol{u} + \mathbf{L}(\mathbf{y} - \mathbf{C}\hat{\mathbf{x}} - \mathbf{D}\boldsymbol{u}) \\ \boldsymbol{u} &= -\mathbf{K}\hat{\mathbf{x}} + \boldsymbol{v} \\ \boldsymbol{e} &= \mathbf{y} - \mathbf{C}\hat{\mathbf{x}} - \mathbf{D}\boldsymbol{u} \end{aligned} \tag{6.15}$$

where $\mathbf{K}$ and $\mathbf{L}$ respectively represent the state feedback and the observer gain. Finally, the control law order $\mathbf{K}(\mathbf{Q})$ is the sum of the order of the initial control law $\mathbf{K}_0$ and the order of $\mathbf{Q}$.

6.4.3 Control Design

The utilized longitudinal model of the ACFA 2020 BWB aircraft (a variant of the reduced-order model (ROM) as generated in Sect. 4.1) is of order 23. This model includes 4 rigid states (pitch oscillation and phugoid modes), 6 flexible modes, hence 12 flexible states and 7 lag states. This model is composed of 2 parts: A rigid part which corresponds to the handling qualities model and a flexible part which corresponds to the aeroelastic model.

The structure of the closed loop for the longitudinal control of a civil aircraft is the following one. The measurement signals used by the controller are $Nz_{\text{long.law}}$, q, and Nz_{CG}. The signals q and Nz_{CG}, respectively, represent the pitch rate and the vertical acceleration on the center of gravity. These two outputs are used to obtain satisfactory results for the handling qualities. $Nz_{\text{long.law}} = (Nz_{\text{l.wingtip}} + Nz_{\text{r.wingtip}})/2 - Nz_{\text{CG}}$ where $Nz_{\text{l.wingtip}}$ and $Nz_{\text{r.wingtip}}$ represent respectively the vertical acceleration on the left and right wing allows to catch the symmetric flexible modes of the wing in order to control them and then to decrease the load level and to improve the comfort for passengers. The outputs used by the controller correspond to the elevators (inner and outer) and the outer ailerons. The elevators allow to obtain good handling qualities and the ailerons allow to control the symmetric flexible modes. As just the longitudinal dynamics is investigated ailerons and elevators are deflected in a symmetric way. The last input, Nz_{com}, corresponds to the reference input.

A second-order actuator is used for each input. Besides, a second-order Padé model of a 160 ms delay with an additional low-pass second-order filter is added on q and Nz_{CG}. A second-order Padé model of a 60 ms delay is added on $Nz_{\text{long.law}}$. These actuators have specific characteristics since the dynamics of these actuators are very slow as indicated by Table 6.1. This kind of dynamics leads to a high amplitude of controller output signals. Besides, as rate limiters and saturations are situated before actuators on the controller outputs, rate limiters represent strong constraints for the command effort. Data about saturations and rate limiters are given in Table 6.1.

Globally the system to control is of order 37 (aircraft 23 + actuators 4 + sensors 10). Of course, it is necessary to add other inputs and outputs which are not used by the controller but essential to satisfy specifications such as the wind and derivative wind inputs, WRMX and WRFz outputs, and cabin accelerations to improve comfort.

The considered flight domain is defined by 3 Mach numbers and 3 dynamic pressures. Tables 6.2 and 6.3 provide the different flight cases in altitudes and true air speed. Eight fuel cases have been considered from the case 20 % to the case full fuel tank by step of 10 %. Finally, 9 flight cases and 9 fuel/mass cases are obtained which correspond to 81 models.

To evaluate the load level, two kinds of signal for perturbations can be considered. The first one is the turbulence which is usually represented by a linearized von-Kármán filter. In our application, this perturbation does not represent the critical perturbation in the sense that it does not lead to a high load level. The second one is the discrete gust which is modeled by the following relation:

Table 6.1 Actuators characteristics

	Damping	Frequency (rad/s)	Position limits (°)	Velocity limits (°/s)
Elevators	0.707	2.71	[−30, +15]	[−30, +30]
Outer ailerons	0.707	7.77	[−25, +25]	[−40, +40]

Table 6.2 True air speed V_{TAS} in m/s

	Mach case 1	Mach case 2	Mach case 3
V1	243.6	251.6	259.8
V2	248.6	256.1	263.7
V3	252.9	260.3	267.7

Table 6.3 Altitude in m

	Mach case 1	Mach case 2	Mach case 3
H1	10,871	11,335	11,777
H2	9,031	9,513	9,973
H3	7,793	8,287	8,761

$$U = \frac{U_{ds}}{2} \times \left[1 - \cos\left(\frac{\pi\, V_{\mathrm{TAS}}}{H} t\right)\right] \tag{6.16}$$

where V_{TAS} is the true airspeed of the aircraft, U_{ds} the amplitude which varies from 11.9 to 19 m/s and H the scale which lies between 9 and 152.4 m. This kind of perturbation leads to sizing load levels.

6.4.3.1 The Initial Stabilizing Controller

The initial stabilizing controller has been designed by a classical LQG approach. Let us remind that this approach is based on the minimization of the following criterion:

$$\int_{-\infty}^{+\infty} \left(\mathbf{x}^{\mathrm{T}}\mathbf{Q}\mathbf{x} + \boldsymbol{u}^{\mathrm{T}}\mathbf{R}\boldsymbol{u}\right) \mathrm{d}t \tag{6.17}$$

where $\mathbf{x}$ is the state vector and $\boldsymbol{u}$ is the input signal of the system to control such as:

$$\begin{aligned} \dot{\mathbf{x}} &= \mathbf{A}\mathbf{x} + \mathbf{B}\boldsymbol{u} \\ \mathbf{y} &= \mathbf{C}\mathbf{x} + \mathbf{D}\boldsymbol{u} \end{aligned} \tag{6.18}$$

Matrices $\mathbf{Q}$ and $\mathbf{R}$ are design parameters and are chosen to satisfy specifications. Finally, a state feedback $\mathbf{K}$ such as $\boldsymbol{u} = -\mathbf{K}\mathbf{x}$ is obtained. A similar formulation exists to synthesize the observer gain $\mathbf{L}$.

6.4.4 Validation and Discussion

As indicated previously, convex synthesis is done in two steps. The first one is to obtain an initial stabilizing LPV controller. From methodological point of view, this

initial controller is designed to satisfy specifications on the rigid part. The rigid part is a fourth-order model with two dynamics: the pitch oscillation and the phugoid modes.

6.4.4.1 Handling Qualities

Specifications concern the pitch oscillation since the phugoid is treated thanks to an auto-throttle which is not the objective here. But a hard constraint must be respected since the pitch oscillation control do not make the phugoid too unstable, that is, the phugoid must remain real and the possible instability inferior to +0.1 rad/s. In other words, the phugoid can be unstable but real and very slow to be controllable by the pilot. Specifications are the following ones:

- A static error null between the Nz command Nz_{com} and Nz_{CG} for a step input;
- Perturbation rejection must be ensured;
- A correct closed-loop pole placement, that is, the control law is able to reject a non-measured perturbation in 5 or 6 s;
- A first-order behavior for Nz_{CG} with a step reference input on Nz_{com}. A rising time of 3–6 s is expected with a very limited overshoot on Nz and an overshoot maximum of 30 % on q.

The first three specifications can be and must be satisfied only by the feedback. In fact, it is necessary to have an integrator in the controller to ensure the perturbation rejection and the null static error. Besides, the closed-loop pole placement cannot be modified by a feed-forward, hence it is necessary to satisfy with the feedback the specification concerning the perturbation rejection in 5 or 6 s. The last specification is treated thanks to a feed-forward. However, to make easier the design of the feed-forward, it is interesting to have, with only the feedback, time-domain response as closed as possible to this specification.

The structure of the 2DOF controller is given by Fig. 6.9. Let us notice the integrator pole in the controller to ensure a perturbation rejection, the feed-forward which acts on only the elevators to satisfy handling qualities specifications and the Youla parameter which uses the estimation error.

Design of the State-Feedback Controller

The design model corresponds to the most unstable model with pitch oscillation and phugoid modes. The phugoid mode is unstable (-0.133 and $+0.206$), while the damping ratio of the short-period mode, namely 0.527, is close to the minimum value over the operating range.

The design model for the state-feedback controller is the 21 state integral model (with a second-order rigid part only corresponding to the pitch oscillation) + actuator and sensor models + an integrator on the Nz_{CG} output. Only the elevators are used.

An LQ method is used as written previously to design the initial stabilizing controller. $R = 1$ for the weighting matrix on u_1 and the weighting matrix Q for the

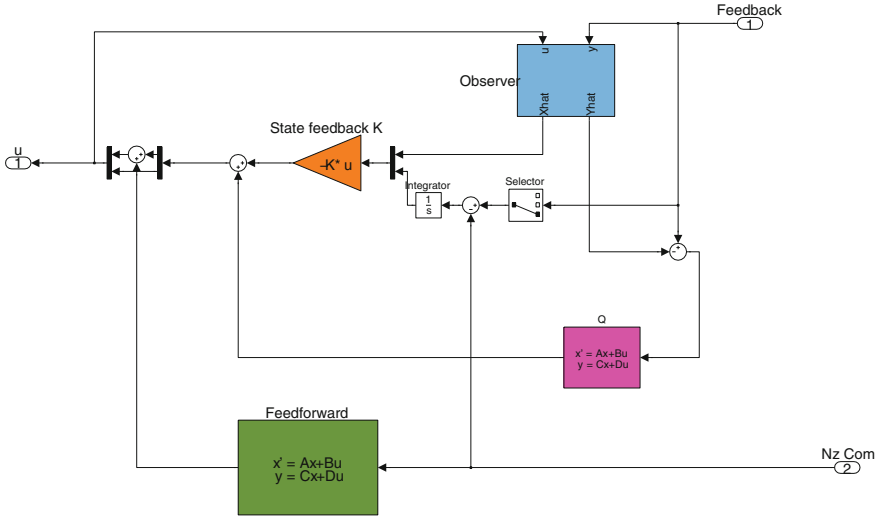

Fig. 6.9 Structure of the 2DOF controller

states corresponds to $Q = \mu_1 c_1 c_1^{\mathrm{T}} + \mu_2 c_2 c_2^{\mathrm{T}}$. The output $y_1 = c_1^{\mathrm{T}} x$ corresponds to the integrator on the Nz_{CG} output, while $y_2 = c_2^{\mathrm{T}} x$ corresponds to the Nz_{CG} output itself. For the application, $\mu_1 = \mu_2 = 0.01$.

Finally, the results in terms of closed-loop pole placement are the following ones for all models over the operating range with only the pitch oscillation:

- The integrator pole remains real in closed loop;
- The open-loop real lag pole remains real in closed loop;
- The pitch oscillation mode, with a damping ratio of about 0.5 in open loop, is accelerated and a bit more damped.

The previous results are not modified by the phugoid, that is, with a 23rd-order model. Besides for all models over the operating range, the worst-case stability degree for the phugoid is $+0.007$, which is very satisfactory since widely inferior to 0.1 rad/s which is the limit imposed by specifications.

To illustrate these results, time-domain responses of the closed loop between Nz_{com} and Nz_{CG} are given by Fig. 6.10a, b. Let us notice that results without phugoid are rather close to the final specifications expected with a feed-forward. Then it is reasonable to assume that it will be possible to satisfy specifications on all models with a simple multi-model feed-forward. The state-feedback controller is globally (very) satisfactory.

Design of the Observer Gain

The model embedded inside the observed state-feedback controller is chosen to be the integral 21 state model (with only a second-order rigid part corresponding to the pitch

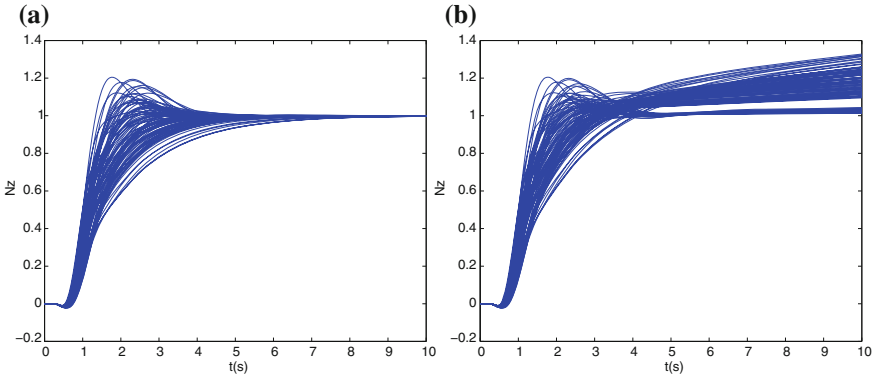

Fig. 6.10 Time-domain response of Nz_{CG} for a step input on Nz_{com}. **a** Time-domain response without phugoid. **b** Time-domain response with phugoid

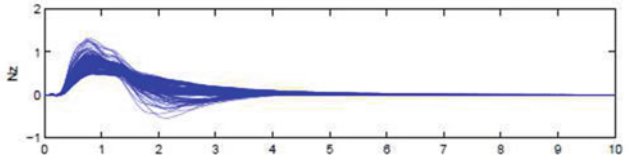

Fig. 6.11 Step response to the filtered wind input on all models without phugoid

oscillation mode) as well as actuator and sensor models. There is no integrator on the Nz_{CG} output since this state is directly available for the state-feedback controller. Remember that the pitch oscillation mode is correctly damped, so that the observer gain is simply chosen as zero. The resulting observed state-feedback controller is first tested on all models without phugoid mode, for the step response to a filtered wind input. More precisely, a filter $1/(1+0.05\text{s})$ is applied to the wind input w and a filter $s/(1+0.05\text{s})$ is applied to $\mathrm{d}w/\mathrm{d}t$. The result seems satisfactory (see Figs. 6.11 and 6.12). The step response to a reference acceleration input is the same as the one obtained with the state-feedback controller, and the closed-loop poles correspond to those obtained with the state feedback and observer gains, so that they need not be checked. Then the estimated state-feedback controller is applied to all models with phugoid mode:

- As for the closed-loop poles, the worst-case stability degree is $+1.951\text{e}{-}02$, which means that the phugoid mode has been essentially stabilized (remember its worst-case open loop value is $+0.206$).
- The step responses to a reference acceleration input are displayed in Fig. 6.13.

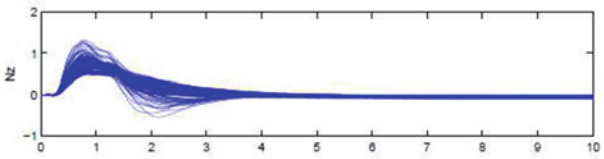

Fig. 6.12 Step response to the filtered wind input on all models with phugoid

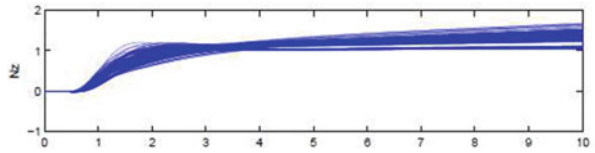

Fig. 6.13 Time-domain response of Nz_{CG} for a step input on Nz_{com} with phugoid mode for all models

6.4.4.2 Control of the Flexible Part

Specifications on the flexible part are treated thanks the Youla parameter design. Let us remind that the closed-loop transfer functions are parametrized with respect to the Youla parameter of the following way:

$$\mathbf{T}_{w\to z} = \mathbf{T}_1 + \mathbf{T}_2\mathbf{Q}\mathbf{T}_3 \tag{6.19}$$

where $\mathbf{T}_{w\to z}$ represents the closed-loop transfer function to minimize or to constrain, $\mathbf{T}_1$ the initial closed-loop transfer function, $\mathbf{T}_2$ and $\mathbf{T}_3$ closed-loop transfer functions which depend on the initial stabilizing controller. Specifications on the flexible model are the following ones:

- To minimize the WRMX load level for sizing cases with critical perturbations;
- A command effort to minimize the WRMX compatible with saturations and rate limiters;
- A WRFz preserved with minimization of the WRMX load level;
- Improvement of the passengers comfort.

Load Level Alleviation

The first specification is the main specification and the most difficult one. Typically, the perturbation is either a turbulence or a discrete gust. However, generally speaking, the discrete gust is the perturbation which leads to the maximum load level for the WRMX. For discrete gusts, the load level is evaluated as an $\mathscr{L}_\infty$ norm on the output WRMX for a specific discrete gust. For each flight and mass case, 10 different discrete gusts, which correspond to 10 different amplitudes U_{ds} and scales H, are applied. Besides when the WRMX load level is decreased for one discrete gust, one mass and one flight case, the load level must represent the maximum load level for all

other discrete gusts and flight/fuel cases. In other words, it is difficult to guarantee a maximum load level for all cases. Of course, as indicated previously, it must be done while satisfying saturations and rate limiters with a limited WRFz load level.

Another and last point is to take into account the 1 g load. This static load is specific to the longitudinal dynamic and perfectly natural since it corresponds to the compensation of the weight of the aircraft. In brief, the total load level is the result of a static part and a dynamic part. But if the dynamic load is obtained by the linear time-domain simulations, it is not the case of the 1 g load. For all that it is the total load which must be minimized and if the same constraint is imposed for all dynamic load it is not relevant because the total load can be very different due to the 1 g load. A solution is to impose a constraint different for each dynamic load in order to have the same constraint for the total load level.

To decrease the WRMX load level sizing fuel and flight cases have been determined. Besides discrete gusts which lead to the highest WRMX load level are determined too. These discrete gusts are called critical discrete gusts. In brief, just sizing flight and fuel cases with critical discrete gusts are used in the optimization problem. But the analysis a posteriori is done with all fuel and flight cases and all discrete gusts.

For all figures, constraints are represented by red lines, static load levels by green lines and dynamic or total load levels by blue lines. For a upward discrete gust , the bending moment is negative, so the sizing value is represented by the negative part. A constraint on the dynamic load is evaluated for each fuel and flight sizing case (Fig. 6.14a). The Youla parameter is designed and finally the result on the dynamic load level is given by Fig. 6.14b. Results on total load level are given by Fig. 6.15b where we notice that the constraint is the same for all cases (Fig. 6.15a, b) since the constraint on the dynamic part has been evaluated for this. Finally, a load alleviation of 17 % is obtained on the total load level (Fig. 6.15b). An important point is to check that WRMX load level for all flight and mass cases and all discrete gusts satisfy constraints, which represent 81 models $\times$ 10 discrete gusts totalling 810 time-domain simulations for each figure. These responses are presented in Fig. 6.16a, b. Thanks to these figures we notice that the constraints are satisfied for all cases.

Command Effort

Let us remind that in the nonlinear scheme, saturations and rate limiters are situated before the actuators and consequently on the controller outputs. Then the signals which are considered for the synthesis and the analysis are controller outputs. Critical constraints are imposed by rate limiters since the deflection velocity before actuator is very high due to limited actuators bandwidth.

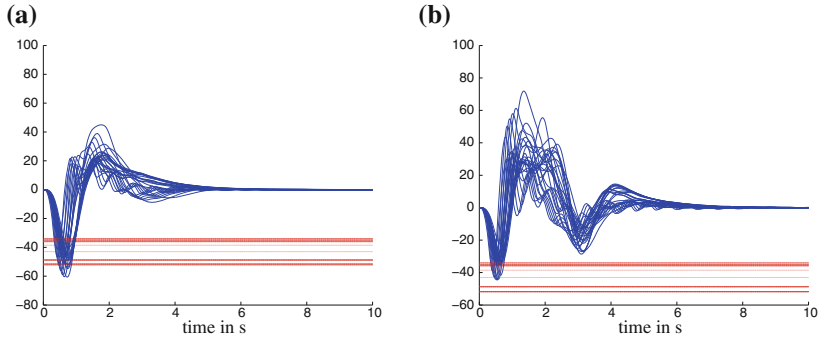

Fig. 6.14 Time-domain response of the WRMX *dynamic* load level with discrete gust. **a** WRMX time-domain response without Youla parameter. **b** WRMX time-domain response with Youla parameter

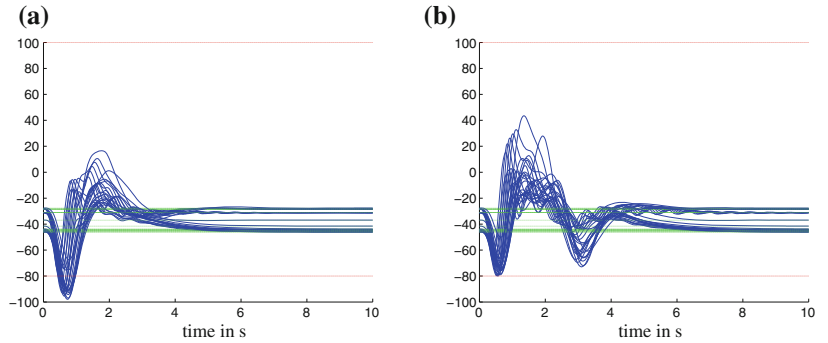

Fig. 6.15 Time-domain response of the WRMX *total* load level with discrete gust. **a** WRMX time-domain response without Youla parameter. **b** WRMX time-domain response with Youla parameter

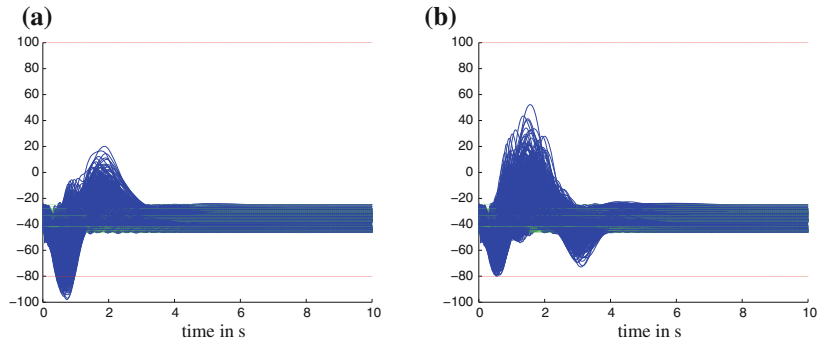

Fig. 6.16 Time-domain response of the WRMX *total* load level with all discrete gusts and all fuel and mass cases. **a** WRMX time-domain response without Youla parameter. **b** WRMX time-domain response with Youla parameter

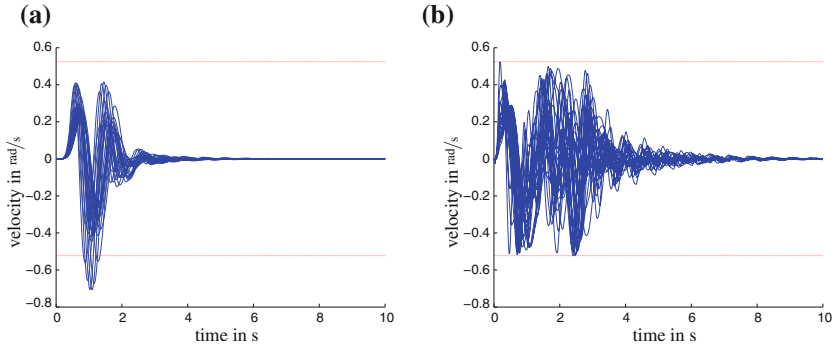

Fig. 6.17 Deflection velocity of elevators for sizing mass and flight cases and critical discrete gusts. **a** Deflection velocity of elevators without Youla parameter. **b** Deflection velocity of elevators with Youla parameter

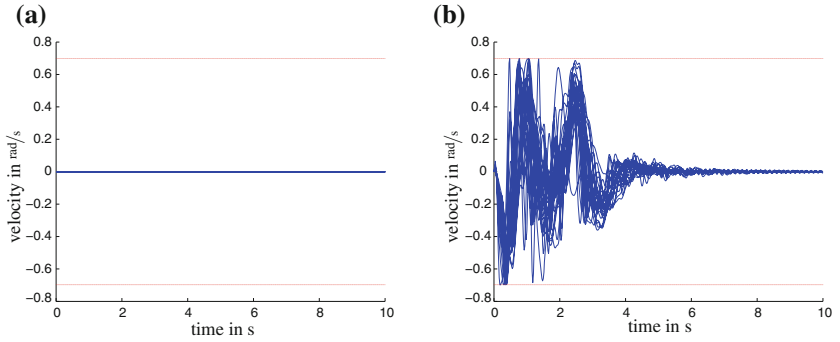

Fig. 6.18 Deflection velocity of outer ailerons for sizing mass and flight cases and critical discrete gusts. **a** Deflection velocity of outer ailerons without Youla parameter. **b** Deflection velocity of outer ailerons with Youla parameter

Figures 6.17, 6.18, 6.19 and 6.20 represent deflections (in rad) and deflection velocity (in rad/s) of outer ailerons and elevators for sizing flight and mass cases and critical gusts with respect to time in seconds. We notice that the constraints represented by red lines are satisfied. These constraints are given by Table 6.1. Let us notice that the initial stabilizing controllers whose the objective is to satisfy handling qualities does not use ailerons, so the result without Youla parameter is 0.

Wing Root Vertical Force Load Level

A specification concerns the WRFz which must be preserved with minimization of the WRMX load level.

In Fig. 6.21, the WRFz load level has been represented for all discrete gusts, mass and flight cases. The red lines on these figures represent the maximal positive and

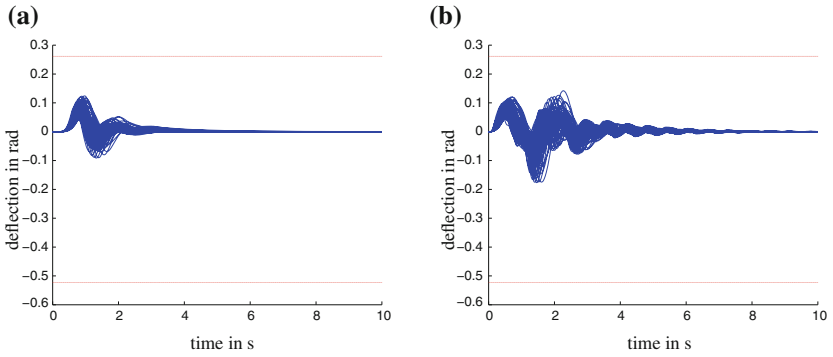

Fig. 6.19 Deflection of elevators for sizing mass and flight cases and critical discrete gusts. **a** Deflection of elevators without Youla parameter. **b** Deflection of elevators with Youla parameter

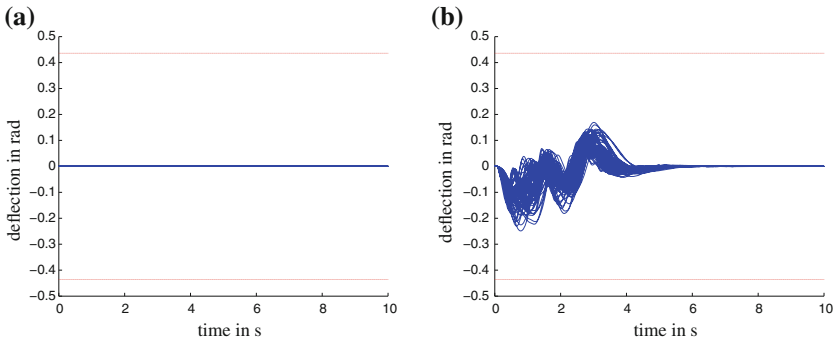

Fig. 6.20 Deflection of outer ailerons for sizing mass and flight cases and critical discrete gusts. **a** Deflection of outer ailerons without Youla parameter. **b** Deflection of outer ailerons with Youla parameter

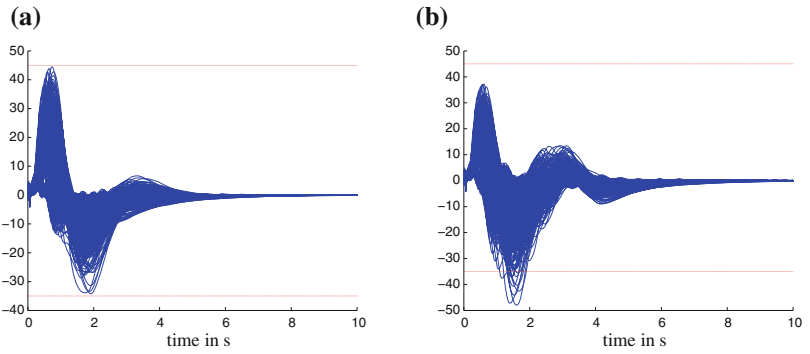

Fig. 6.21 Time-domain response of the WRFz load level with all discrete gusts and all fuel and mass cases. **a** WRFz load level without Youla parameter. **b** WRFz load level with Youla parameter

negative value without Youla parameter. We notice that results with Youla parameter are satisfactory because not only the WRFz is preserved, but also it is decreased for the positive value. The absolute value of the negative part increases but it is not a problem since the 1 g force is positive.

Passenger Comfort

Figures 6.22 and 6.23 represent comfort cabin with two kinds of filters: seasickness and vibration filters. The comfort criterion is based on the $\mathscr{H}_2$ norm of the transfer function. Only result with one comfort cabin output has been represented but 5 comfort cabin outputs have been used in the design scheme. On each figure, the 81 fuel and flight cases have been represented. The input signal is a white noise filtered by a linearized von-Kármán filter. Globally, since 5 comfort cabin outputs are used, the $\mathscr{H}_2$ norm of $5 * 81 = 405$ transfer functions are considered. Of course, it is not possible to represent all these transfer functions but the global reduction of the $\mathscr{H}_2$

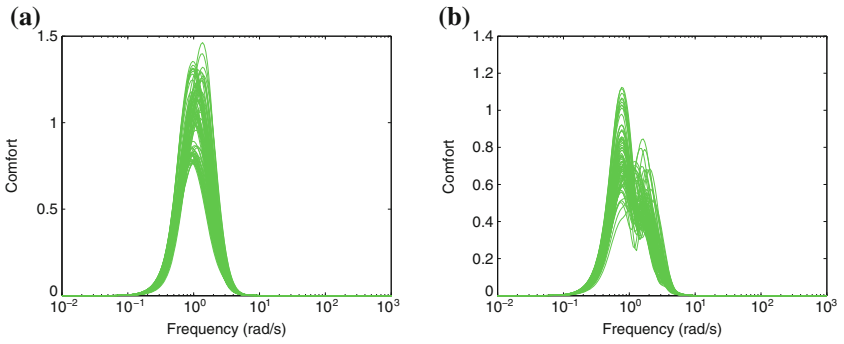

Fig. 6.22 Comfort cabin with seasickness filters. **a** Transfer functions of comfort cabin without Youla parameter. **b** Transfer functions of comfort cabin with Youla parameter

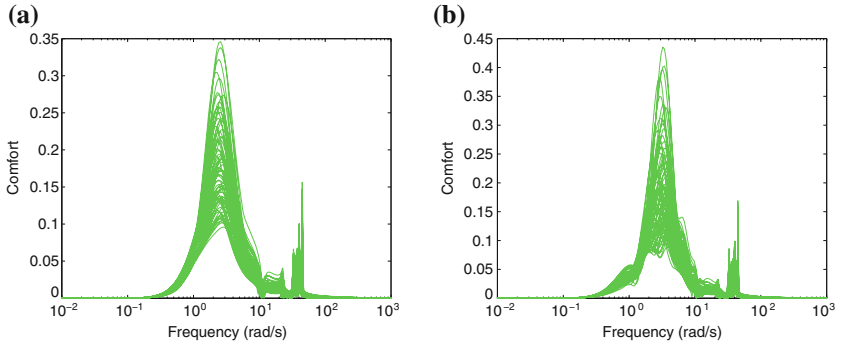

Fig. 6.23 Comfort cabin with vibration filters. **a** Transfer functions of comfort cabin without Youla parameter. **b** Transfer functions of comfort cabin with Youla parameter

norm is 20 %, that is, the comfort has been improved by 20 %. This global reduction can lead to a rise in some transfer functions as it is possible to see in Fig. 6.23b.

6.4.4.3 Feed-Forward

Let us remind handling qualities specifications that we have to satisfy with the feed-forward:

- A rise time of 3–6 s is expected with a very limited overshoot on Nz;
- A maximum overshoot of 30 % on q.

Figure 6.24 represents handling qualities when the feed-forward law is designed and implemented. We can notice that specifications are fully satisfied now since:

- The overshoot on Nz_{CG} is limited to 1 % for the worst case with a mean of 0.45 %;
- The rising time on Nz_{CG} is 5.95 s at 95 % of the wanted value or 4.95 s at 90 % of the wanted value for the worst case. Mean values are respectively of 4.0 and 3.4 s.
- The overshoot on q is limited to 21.5 % for the worst case with a mean value of 5.7 %.

Besides, this feed-forward law is multi-model, that is, a simple transfer function of order 4 allows to satisfy specifications for all fuel and flight cases. Of course, all these results on Nz_{CG} and q are obtained with a limited command effort since we can see in Fig. 6.25 that firstly, only elevators are used by the feed-forward law as shown by Fig. 6.9 and secondly that deflection and deflection velocity are widely inferior to constraints represented by saturations and rate limiters.

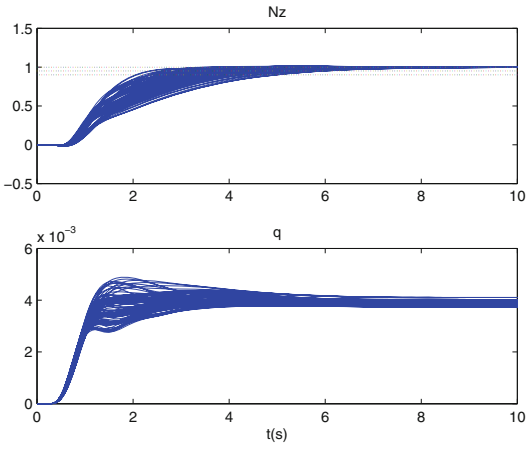

Fig. 6.24 Step response for Nz and q

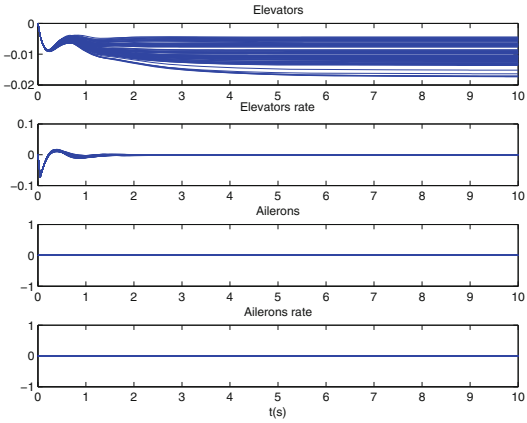

Fig. 6.25 Elevator and aileron responses to step

6.5 LPV Feedback Design

C. Westermayer, A. Schirrer and M. Kozek

The LPV feedback control design presented in this section has been developed in [88] for the longitudinal dynamics of the ACFA 2020 BWB aircraft. Over the design steps, including preliminary and optimized $\mathscr{H}_\infty$ LTI designs, as well as the overall LPV design, both, a linearization family of the ROMs (Sect. 4.1) and a parametrized model in an LFR obtained in Sect. 4.2 has been utilized for analysis, design, and validation tasks.

6.5.1 Methodology—LPV Design Using Parameter-Dependent Lyapunov Functions

In this section, the theoretical background for controller design using parameter-dependent Lyapunov functions is outlined. It follows the derivations in [93], where the information given by upper bounds on parameter variation rates are utilized for controller design of parameter-varying systems in order to obtain less conservative results. An outline of this methodology can also be found in [66], where also the connection to other scheduling approaches is provided. The methodology was already successfully applied to some practical applications [4, 61, 85, 89], which was decisive to use it also for the given problem formulation. More specifically, an LPV design toolbox developed by and kindly provided by Prof. Gary Balas [4], which is based on the methodology of parameter-dependent Lyapunov functions, is utilized for feedback control design of the aeroelastic BWB aircraft.

6.5.1.1 Stability and Performance Analysis of Parameter-Dependent Systems

Starting point for the following considerations is the description of the nonlinear plant

$$\begin{aligned} \dot{\boldsymbol{x}}(t) &= \boldsymbol{f}\left(\boldsymbol{x}(t), \boldsymbol{u}(t), \boldsymbol{d}(t), \boldsymbol{\rho}(t)\right) \\ \boldsymbol{y}(t) &= \boldsymbol{g}\left(\boldsymbol{x}(t), \boldsymbol{d}(t), \boldsymbol{\rho}(t)\right) \\ \boldsymbol{z}(t) &= \boldsymbol{h}\left(\boldsymbol{x}(t), \boldsymbol{u}(t), \boldsymbol{d}(t), \boldsymbol{\rho}(t)\right) \end{aligned} \tag{6.20}$$

where $\boldsymbol{x}(t)$ denotes the state vector, $\boldsymbol{u}$ is the control input, $\boldsymbol{d}$ is the disturbance input, $\boldsymbol{y}$ is the measurement output, $\boldsymbol{z}$ is the error output. Additionally, $\boldsymbol{\rho}(t)$ is the exogenous variable, or also denoted as the parameter vector. This vector is assumed piecewise continuously differentiable and is defined over the compact set $\mathscr{P} \subset \mathbb{R}^s$:

$$\boldsymbol{\rho}(t) = [\rho_1(t)\ \rho_2(t)\ \cdots\ \rho_s(t)]^{\mathrm{T}} \qquad \boldsymbol{\rho} \in \mathscr{P} \subset \mathbb{R}^s. \tag{6.21}$$

Moreover, the parameter vector rate of variation is bounded such that

$$|\dot{\rho}_i(t)| \leq \nu_i, \quad i = 1, \ldots, s. \tag{6.22}$$

holds. Linearization of (6.20) for a set of fixed parameters in an equilibrium point with respect to $\boldsymbol{x}$, $\boldsymbol{u}$ and $\boldsymbol{d}$ leads to a linear parameter-dependent description for the nonlinear plant

$$\begin{bmatrix} \dot{\boldsymbol{x}} \\ \boldsymbol{z} \\ \boldsymbol{y} \end{bmatrix} = \begin{bmatrix} \boldsymbol{A}(\boldsymbol{\rho}) & \boldsymbol{B}_1(\boldsymbol{\rho}) & \boldsymbol{B}_2(\boldsymbol{\rho}) \\ \boldsymbol{C}_1(\boldsymbol{\rho}) & \boldsymbol{D}_{11}(\boldsymbol{\rho}) & \boldsymbol{D}_{12}(\boldsymbol{\rho}) \\ \boldsymbol{C}_2(\boldsymbol{\rho}) & \boldsymbol{D}_{21}(\boldsymbol{\rho}) & \boldsymbol{D}_{22}(\boldsymbol{\rho}) \end{bmatrix} \begin{bmatrix} \boldsymbol{x} \\ \boldsymbol{d} \\ \boldsymbol{u} \end{bmatrix} \tag{6.23}$$

Utilizing the assumptions that $\boldsymbol{D}_{22}(\boldsymbol{\rho}) = \boldsymbol{0}$, $\boldsymbol{D}_{12}(\boldsymbol{\rho})$ has full column rank and $\boldsymbol{D}_{21}(\boldsymbol{\rho})$ full row rank for all $\boldsymbol{\rho} \in \mathscr{P}$, the open-loop system representation (6.23) can without loss of generality be transformed in a simplified form for synthesis:

$$\begin{bmatrix} \dot{\boldsymbol{x}} \\ \boldsymbol{z}_1 \\ \boldsymbol{z}_2 \\ \boldsymbol{y} \end{bmatrix} = \begin{bmatrix} \boldsymbol{A}(\boldsymbol{\rho}) & \boldsymbol{B}_{11}(\boldsymbol{\rho}) & \boldsymbol{B}_{12}(\boldsymbol{\rho}) & \boldsymbol{B}_2(\boldsymbol{\rho}) \\ \boldsymbol{C}_{11}(\boldsymbol{\rho}) & \boldsymbol{D}_{1111}(\boldsymbol{\rho}) & \boldsymbol{D}_{1112}(\boldsymbol{\rho}) & \boldsymbol{0} \\ \boldsymbol{C}_{12}(\boldsymbol{\rho}) & \boldsymbol{D}_{1121}(\boldsymbol{\rho}) & \boldsymbol{D}_{1122}(\boldsymbol{\rho}) & \mathrm{I}_{n_{z2}} \\ \boldsymbol{C}_2(\boldsymbol{\rho}) & \boldsymbol{0} & \mathrm{I}_{n_{d2}} & \boldsymbol{0} \end{bmatrix} \begin{bmatrix} \boldsymbol{x} \\ \boldsymbol{d}_1 \\ \boldsymbol{d}_2 \\ \boldsymbol{u} \end{bmatrix}. \tag{6.24}$$

The parameter vector $\boldsymbol{\rho}$ and its derivative $\dot{\boldsymbol{\rho}}$ are assumed to be measurable in real time and therefore can be used as an additional information for the controller. This leads to the system representation of the controller

$$\begin{bmatrix} \dot{\boldsymbol{x}}_{\mathrm{K}} \\ \boldsymbol{u} \end{bmatrix} = \begin{bmatrix} \boldsymbol{A}_{\mathrm{K}}(\boldsymbol{\rho}, \dot{\boldsymbol{\rho}}) & \boldsymbol{B}_{\mathrm{K}}(\boldsymbol{\rho}, \dot{\boldsymbol{\rho}}) \\ \boldsymbol{C}_{\mathrm{K}}(\boldsymbol{\rho}, \dot{\boldsymbol{\rho}}) & \boldsymbol{D}_{\mathrm{K}}(\boldsymbol{\rho}, \dot{\boldsymbol{\rho}}) \end{bmatrix} \begin{bmatrix} \boldsymbol{x}_{\mathrm{K}} \\ \boldsymbol{y} \end{bmatrix}, \tag{6.25}$$

which is also parameter-dependent. Using a lower (LFT), the closed loop can be built

$$\begin{bmatrix} \dot{\boldsymbol{x}}_{\mathrm{cl}} \\ \boldsymbol{z} \end{bmatrix} = \begin{bmatrix} \boldsymbol{A}_{\mathrm{cl}}(\boldsymbol{\rho}, \dot{\boldsymbol{\rho}}) & \boldsymbol{B}_{\mathrm{cl}}(\boldsymbol{\rho}, \dot{\boldsymbol{\rho}}) \\ \boldsymbol{C}_{\mathrm{cl}}(\boldsymbol{\rho}, \dot{\boldsymbol{\rho}}) & \boldsymbol{D}_{\mathrm{cl}}(\boldsymbol{\rho}, \dot{\boldsymbol{\rho}}) \end{bmatrix} \begin{bmatrix} \boldsymbol{x}_{\mathrm{cl}} \\ \boldsymbol{d} \end{bmatrix}, \tag{6.26}$$

with

$$\boldsymbol{A}_{\mathrm{cl}} = \begin{bmatrix} \boldsymbol{A}(\boldsymbol{\rho}) + \boldsymbol{B}_2(\boldsymbol{\rho})\boldsymbol{D}_{\mathrm{K}}(\boldsymbol{\rho}, \dot{\boldsymbol{\rho}})\boldsymbol{C}_2(\boldsymbol{\rho}) & \boldsymbol{B}_2(\boldsymbol{\rho})\boldsymbol{C}_{\mathrm{K}}(\boldsymbol{\rho}, \dot{\boldsymbol{\rho}}) \\ \boldsymbol{B}_{\mathrm{K}}(\boldsymbol{\rho}, \dot{\boldsymbol{\rho}})\boldsymbol{C}_2(\boldsymbol{\rho}) & \boldsymbol{A}_{\mathrm{K}}(\boldsymbol{\rho}, \dot{\boldsymbol{\rho}}) \end{bmatrix}, \tag{6.27}$$

$$\boldsymbol{B}_{\mathrm{cl}} = \begin{bmatrix} \boldsymbol{B}_{11}(\boldsymbol{\rho}) & \boldsymbol{B}_{12}(\boldsymbol{\rho}) + \boldsymbol{B}_2(\boldsymbol{\rho})\boldsymbol{D}_{\mathrm{K}}(\boldsymbol{\rho}, \dot{\boldsymbol{\rho}}) \\ \boldsymbol{0} & \boldsymbol{B}_{\mathrm{K}}(\boldsymbol{\rho}, \dot{\boldsymbol{\rho}}) \end{bmatrix}, \tag{6.28}$$

$$\boldsymbol{C}_{\mathrm{cl}} = \begin{bmatrix} \boldsymbol{C}_{11}(\boldsymbol{\rho}) & \boldsymbol{0} \\ \boldsymbol{C}_{12}(\boldsymbol{\rho}) + \boldsymbol{D}_{\mathrm{K}}(\boldsymbol{\rho}, \dot{\boldsymbol{\rho}})\boldsymbol{C}_2(\boldsymbol{\rho}) & \boldsymbol{C}_{\mathrm{K}}(\boldsymbol{\rho}, \dot{\boldsymbol{\rho}}) \end{bmatrix}, \tag{6.29}$$

$$\boldsymbol{D}_{\mathrm{cl}} = \begin{bmatrix} \boldsymbol{D}_{1111}(\boldsymbol{\rho}) & \boldsymbol{D}_{1112}(\boldsymbol{\rho}) \\ \boldsymbol{D}_{1121} & \boldsymbol{D}_{1122}(\boldsymbol{\rho})\boldsymbol{D}_{\mathrm{K}}(\boldsymbol{\rho}, \dot{\boldsymbol{\rho}}) \end{bmatrix}. \tag{6.30}$$

In order to test stability of the parameter-dependent systems such as (6.24) or (6.26), the Lyapunov stability test [40] can be used. However, this test is based on a quadratic, parameter-independent Lyapunov function

$$\mathbf{V}(\boldsymbol{x}) = \boldsymbol{x}^{\mathrm{T}}\mathbf{X}\boldsymbol{x}, \quad \mathbf{X} = \mathbf{X}^{\mathrm{T}} \tag{6.31}$$

and proves stability for arbitrarily fast changing parameters. Therefore, utilizing this analysis test as a basis for controller synthesis of parameter-varying systems leads to either conservative results or in terms of an LMI optimization even to infeasibility although a feasible result could exist. Instead of the quadratic Lyapunov function, a parameter-dependent Lyapunov function of the form

$$\mathbf{V}(\boldsymbol{x}, \boldsymbol{\rho}) = \boldsymbol{x}^{\mathrm{T}}\mathbf{X}(\boldsymbol{\rho})\boldsymbol{x}, \quad \mathbf{X}(\boldsymbol{\rho}) = \mathbf{X}^{\mathrm{T}}(\boldsymbol{\rho}) \tag{6.32}$$

can be introduced. Its time derivative is given by

$$\begin{aligned} \frac{\mathrm{d}}{\mathrm{d}t}\mathbf{V}(\boldsymbol{x}, \boldsymbol{\rho}) &= \dot{\boldsymbol{x}}^{\mathrm{T}}\mathbf{X}(\boldsymbol{\rho})\boldsymbol{x} + \boldsymbol{x}^{\mathrm{T}}\mathbf{X}(\boldsymbol{\rho})\dot{\boldsymbol{x}} + \frac{\mathrm{d}}{\mathrm{d}t}\mathbf{X}(\boldsymbol{\rho}) \\ &= \dot{\boldsymbol{x}}^{\mathrm{T}}\mathbf{X}(\boldsymbol{\rho})\boldsymbol{x} + \boldsymbol{x}^{\mathrm{T}}\mathbf{X}(\boldsymbol{\rho})\dot{\boldsymbol{x}} + \sum_{i=1}^{s}\left(\dot{\rho}_i \frac{\partial \mathbf{X}(\boldsymbol{\rho})}{\partial \rho_i}\right). \end{aligned} \tag{6.33}$$

Using this Lyapunov function, the stability test for parameter-dependent systems can be defined as follows.

Definition 6.1 (*Parameter-dependent stability* [93]) For a given compact parameter set $\boldsymbol{\rho} \in \mathscr{P} \subset \mathbb{R}^s$ and non-negative upper bounds of parameter variation rates $\{\nu_i\}_{i=1}^s$, consider a linear parameter-varying system

$$\dot{\boldsymbol{x}} = \boldsymbol{A}(\boldsymbol{\rho}, \dot{\boldsymbol{\rho}})\boldsymbol{x}, \quad \boldsymbol{x}(t_0) = \boldsymbol{x}_0, \tag{6.34}$$

which is called parametrically dependent stable if $\lim_{t\to\infty} \boldsymbol{x}(t) = 0$ for all $\boldsymbol{x}_0$. Using the parameter-dependent Lyapunov function (6.32), then $\boldsymbol{A}(\boldsymbol{\rho}, \dot{\boldsymbol{\rho}})$ is parametrically dependent stable over $\mathscr{P}$ if there exists a continuously differentiable function $\mathbf{X}(\boldsymbol{\rho})$: $\mathbb{R}^s \to \mathbb{S}^{n\times n}$, such that $\mathbf{X}(\boldsymbol{\rho}) = \mathbf{X}^{\mathrm{T}}(\boldsymbol{\rho}) > 0$ and

$$\boldsymbol{A}^{\mathrm{T}}(\boldsymbol{\rho}, \dot{\boldsymbol{\rho}})\mathbf{X}(\boldsymbol{\rho}) + \mathbf{X}(\boldsymbol{\rho})\boldsymbol{A}(\boldsymbol{\rho}, \dot{\boldsymbol{\rho}}) + \sum_{i=1}^{s} \left(\dot{\rho}_i \frac{\partial \mathbf{X}}{\partial \rho_i} \right) < 0 \tag{6.35}$$

for all $\boldsymbol{\rho} \in \mathscr{P}$ and $|\dot{\rho}_i| \leq \nu_i$ holds.

The proof is given in [93]. This parameter-dependent stability criterion incorporates bounds on the maximum parameter rates of variation and therefore is less conservative than the quadratic stability criterion. In order to obtain a similar stability and performance test as given by the classical Bounded Real Lemma [68] for LTI systems, this lemma has to be generalized for parameter-varying systems using the parameter-dependent Lyapunov function (6.32). An appropriate corresponding performance measure for LPV systems is given by the induced $\mathscr{L}_2$-norm which is defined for the performance transfer path as

$$||T_{zd}||_{i,2} = \sup_{\substack{\rho\in\mathscr{P} \\ |\dot{\rho}|\leq \boldsymbol{\nu}}} \sup_{\|\boldsymbol{d}\|_2 \neq 0} \frac{||\boldsymbol{z}||_2}{||\boldsymbol{d}||_2}. \tag{6.36}$$

This norm is equivalent to the largest amplification of the disturbance norm $||\boldsymbol{d}||_2$ to the error norm $||\boldsymbol{z}||_2$ for all parameter trajectories that satisfy $\boldsymbol{\rho} \in \mathscr{P}$ and hence represents a generalization of the $\mathscr{H}_\infty$-norm for LTI systems to LPV systems [93]. Consequently, the following theorem is derived which provides a sufficient condition for parameter-dependent stability and a prescribed bound for the induced $\mathscr{L}_2$-norm of a linear parameter-dependent system.

Theorem 6.1 [93] *For a given compact parameter set $\boldsymbol{\rho} \in \mathscr{P} \subset \mathbb{R}^s$ and non-negative upper magnitude bounds of parameter variation rates $\{\nu_i\}_{i=1}^s$, consider the linear parameter-varying system (6.26). If there exists a continuously differentiable matrix function $\mathbf{X}(\boldsymbol{\rho}) = \mathbf{X}^{\mathrm{T}}(\boldsymbol{\rho})$ such that*

$$\begin{aligned} &\mathbf{X}(\boldsymbol{\rho}) > 0, \\ &\begin{bmatrix} \boldsymbol{A}_{\mathrm{cl}}^{\mathrm{T}}(\boldsymbol{\rho}, \dot{\boldsymbol{\rho}})\mathbf{X}(\boldsymbol{\rho}) + \mathbf{X}(\boldsymbol{\rho})\boldsymbol{A}_{\mathrm{cl}}(\boldsymbol{\rho}, \dot{\boldsymbol{\rho}}) + \sum_{i=1}^{s} \left(\dot{\rho}_i \frac{\partial \mathbf{X}}{\partial \beta_i} \right) \mathbf{X}(\boldsymbol{\rho})\boldsymbol{B}_{\mathrm{cl}}(\boldsymbol{\rho}, \dot{\boldsymbol{\rho}}) \\ \boldsymbol{B}_{\mathrm{cl}}^{\mathrm{T}}(\boldsymbol{\rho}, \dot{\boldsymbol{\rho}})\mathbf{X}(\boldsymbol{\rho}) \qquad\qquad\qquad\qquad \mathbf{0} \end{bmatrix} \\ &\quad + \begin{bmatrix} \mathbf{0} & \mathbf{I} \\ \boldsymbol{C}_{\mathrm{cl}}(\boldsymbol{\rho}, \dot{\boldsymbol{\rho}}) & \boldsymbol{D}_{\mathrm{cl}}(\boldsymbol{\rho}, \dot{\boldsymbol{\rho}}) \end{bmatrix}^{\mathrm{T}} \begin{bmatrix} -\gamma^2\mathbf{I} & \mathbf{0} \\ \mathbf{0} & \mathbf{I} \end{bmatrix} \begin{bmatrix} \mathbf{0} & \mathbf{I} \\ \boldsymbol{C}_{\mathrm{cl}}(\boldsymbol{\rho}, \dot{\boldsymbol{\rho}}) & \boldsymbol{D}_{\mathrm{cl}}(\boldsymbol{\rho}, \dot{\boldsymbol{\rho}}) \end{bmatrix} < 0 \end{aligned} \tag{6.37}$$

holds for all $\boldsymbol{\rho} \in \mathscr{P}$ and $|\beta_i| \leq \nu_i$, then

1. *the function $\boldsymbol{A}_{cl}(\boldsymbol{\rho}, \dot{\boldsymbol{\rho}})$ is parametrically dependent stable over $\mathscr{P}$ and*
2. *the closed-loop performance transfer fulfills $||T_{zd}||_{i,2} < \gamma$.*

In Theorem 6.1 purposely the closed-loop system as given by (6.26) was considered, indicating that this theorem serves as a basis for controller design. Using the Schur complement, the LMI (6.37) can be also written in compact form as

$$\begin{bmatrix} \boldsymbol{A}_{\mathrm{cl}}^{\mathrm{T}}(\boldsymbol{\rho},\dot{\boldsymbol{\rho}})\mathbf{X}(\boldsymbol{\rho}) + \mathbf{X}(\boldsymbol{\rho})\boldsymbol{A}_{\mathrm{cl}}(\boldsymbol{\rho},\dot{\boldsymbol{\rho}}) + \sum_{i=1}^{s}\left(\beta_i \frac{\partial \mathbf{X}}{\partial \rho_i}\right) & \mathbf{X}(\rho)\boldsymbol{B}_{\mathrm{cl}}(\boldsymbol{\rho},\dot{\boldsymbol{\rho}}) & \gamma^{-1}\boldsymbol{C}_{\mathrm{cl}}{}^{\mathrm{T}}(\boldsymbol{\rho},\dot{\boldsymbol{\rho}}) \\ \boldsymbol{B}_{\mathrm{cl}}{}^{\mathrm{T}}(\boldsymbol{\rho},\dot{\boldsymbol{\rho}})\mathbf{X}(\rho) & -\mathrm{I} & \gamma^{-1}\boldsymbol{D}_{\mathrm{cl}}{}^{\mathrm{T}}(\boldsymbol{\rho},\dot{\boldsymbol{\rho}}) \\ \gamma^{-1}\boldsymbol{C}_{\mathrm{cl}}(\boldsymbol{\rho},\dot{\boldsymbol{\rho}}) & \gamma^{-1}\boldsymbol{D}_{\mathrm{cl}}(\boldsymbol{\rho},\dot{\boldsymbol{\rho}}) & -\mathrm{I} \end{bmatrix} < 0. \tag{6.38}$$

This LMI (6.38) can be used as starting point for the derivation of an adequate controller synthesis formulation. For the sake of brevity, the solvability condition for the parameter-dependent γ-performance problem is not presented here and the reader is kindly referred to [93].

The matrix functions $\mathbf{X}(\boldsymbol{\rho})$ represent an infinite-dimensional function space which has to be approximated by a finite-dimensional subspace using a set of continuously differentiable basis functions f_i:

$$\mathbf{X}(\boldsymbol{\rho}) := \sum_{i=1}^{N} f_i(\boldsymbol{\rho})\mathbf{X}_i. \tag{6.39}$$

A guideline for the selection of the basis functions is to choose functions that reflect the parameter dependency of the open-loop plant as close as possible [4, 61, 85]. Moreover, the synthesis LMIs have to be satisfied for all $\boldsymbol{\rho} \in \mathscr{P}$ which would require to solve an infinite number of LMIs. Hence, for computational tractability, the entire parameter space has to be approximated by a representative finite set of grid point models. It is important to keep in mind that both, the selection of basis functions and the gridding density strongly affects computational complexity, since the number of decision variables increases with a higher number of basis functions and grid point models.

6.5.1.2 Design Process

Based on the theoretical aspects outlined above and the information that needs to be gathered from nominal $\mathscr{H}_\infty$ grid point design as will be shown in Sect. 6.5.3, the LPV design process can be described by the following steps:

1. Derive the linearized models from the nonlinear system parameterized by the scheduling variables $\boldsymbol{\rho}$ (see Sect. 4.2). Thereby, attention should be paid on the model order to simplify the subsequent LMI optimization process.
2. Analyze the open-loop model with special emphasis on the effect of varying parameters on the system properties (see Sect. 5.1).

3. Select an appropriate $\mathscr{H}_\infty$ controller design architecture which addresses the required design specifications and define appropriate weighting functions (see Sect. 6.5.3.1).
4. Optimize LTI $\mathscr{H}_\infty$ controllers over the entire parameter space by adjusting the performance weighting functions (see Sect. 6.5.3.2). Preferably, this is done in an automatic way by defining a cost function based on relevant design specifications which have to be optimized (see Sect. 6.5.3.3).
5. Validate the LTI controllers on a representative validation model. If specifications are not satisfied, go back to step 3 and try a different design architecture or different frequency weighting functions.
6. Scale the determined performance weighting functions for each parameter grid point by corresponding obtained γ_{LTI} values in order to avoid over-emphasizing of some grid points in the LPV optimization. At the same time, the finally obtained γ_{LPV} value provides information about the performance degradation in comparison to the LTI design.
7. Select suitable basis functions according to the plant dynamics dependency on scheduling parameters [93], and determine a grid of fixed parameter settings representing the parameter space (see Sect. 6.5.4.1).
8. Define lower and upper bounds for the parameter variation rates representative for the considered application (see Sect. 6.5.4.2).
9. Run of LMI optimization using the linearized models, the design architecture, and the scaled performance weighting functions determined in the previous steps.
10. Split the entire parameter space into smaller subspaces, if the entire parameter space is too large for controller optimization in one step or strong discontinuities in a certain parameter region are present.

If more than one scheduling parameter has to be considered at once, it is to recommend that a priori designs for a single parameter are carried out to develop an understanding about the necessary density of the parameter grid and the effect of various basis functions. With the information gathered, a stepwise enlargement of the parameter space is preferable.

If the LMI optimization leads to a feasible solution, the following steps are necessary to obtain the final LPV control law:

1. Preparation of a fine gridding of linearized models such that several grid points in between the design grid points are available.
2. Linear interpolation of the performance weightings and the γ_{LTI} values between the design grid points.
3. Interconnection of the finely gridded linearized models with the corresponding interpolated and scaled performance weightings.
4. The LPV controller matrices for the fine gridding are obtained as presented in [93], where the system matrix $\mathbf{A}_{\mathrm{LTI}}$ depends on the parameter rate.
5. Optional removal of parameter rate dependency according to [66].

In order to obtain a control law representation which continuously depends on the parameter vector, the finely gridded controller matrices can be linearly interpolated element-wise as in [4].

6.5.2 Design Goals

In this feedback design, the feedback control goals as a subset of the goals listed in Sect. 5.2 are addressed. Especially, robust stabilization, pole placement, and rejection of turbulence or gust disturbances are focused on. Partially, the maneuverability is addressed to improve maneuver performance with the final feed-forward command shaping.

6.5.3 Preceding $\mathscr{H}_\infty$ Design Optimization

6.5.3.1 Design Model and Closed-Loop Interconnection Architecture

As described in Sect. 6.5.1.2, the overall complexity of the feedback control process demands a stepwise design procedure starting with nominal $\mathscr{H}_\infty$ designs. Using the results gathered during the open-loop analysis as presented in Sect. 5.1, an adequate control design architecture needs to be defined.

Initial preliminary designs have revealed that the architecture as proposed in Fig. 6.26 is suitable to successfully address the design goals as formulated in

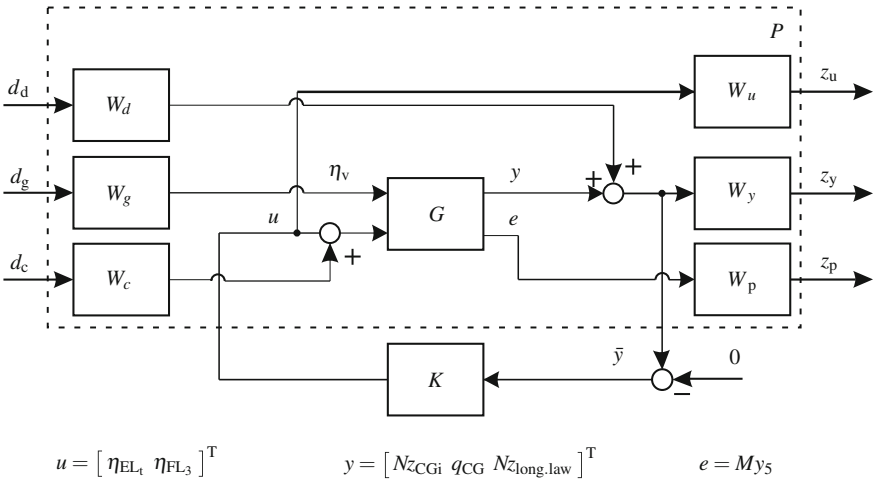

Fig. 6.26 Extended closed-loop interconnection structure

Sect. 6.5.2 in an highly efficient manner. In this architecture, $\mathbf{G}$ is the state-space model of the aircraft

$$\begin{bmatrix} \dot{\boldsymbol{x}}(t) \\ \boldsymbol{e}(t) \\ \boldsymbol{y}(t) \end{bmatrix} = \underbrace{\begin{bmatrix} \boldsymbol{A} & \boldsymbol{B}_1 & \boldsymbol{B}_2 \\ \boldsymbol{C}_1 & \boldsymbol{D}_{11} & \boldsymbol{D}_{12} \\ \boldsymbol{C}_2 & \boldsymbol{D}_{21} & \boldsymbol{D}_{22} \end{bmatrix}}_{\mathbf{G}} \begin{bmatrix} \boldsymbol{x}(t) \\ \boldsymbol{d}(t) \\ \boldsymbol{u}(t) \end{bmatrix}, \tag{6.40}$$

and $\mathbf{K}$ is the feedback controller to be designed. The corresponding state vector $\boldsymbol{x}$ of $\mathbf{G}$ is given by

$$\boldsymbol{x} = \left[u \; w \; \Theta \; q \; \xi_1 \; \dot{\xi}_1 \; \ldots \; \xi_s \; \dot{\xi}_s \; x_{l_1} \; \ldots \; x_{l_t} \right]^{\mathrm{T}}, \tag{6.41}$$

where the first four states represent the RB states body forward velocity u, body downward velocity w, pitch angle Θ and pitch rate q. Neglecting the states u and Θ in (6.41) results in the short-period mode approximation of the aircraft. Using this approximation prevents the $\mathscr{H}_\infty$ optimization algorithm from directly stabilizing the phugoid mode in favor of overall improved closed-loop performance. The states ξ_j and $\dot{\xi}_j$ $(j = 1, \ldots, s)$ are the modal deflections and modal deflection rates of aeroelastic modes, respectively, and x_{l_k} $(k = 1, \ldots, t)$ are the lag states. The number of flexible modes and lag states are different for validation and design models:

- Validation model $\mathbf{G}_{\mathrm{val}}$: $s = 19, \quad t = 14$
- Design model $\mathbf{G}_{\mathrm{des}}$: $s = 2, \quad t = 4$

The number of flexible modes in the design model is set to a comparatively low number due to the limited bandwidth of about 20 rad/s of the investigated control surfaces. However, within this range, the first two symmetrical flexible modes are located which are important in terms of structural loads and vibrations. Moreover, keeping only four lag states for the design turned out to have only marginal effect on the considered system dynamics.

The utilized control inputs $\boldsymbol{u}$ of $\mathbf{G}$ are the combined elevator $\eta_{\mathrm{EL_t}}$ and the fast actuating outer flap $\eta_{\mathrm{FL_3}}$. The first is the control surface most efficient for pitch motion control, while the latter is mainly used for aeroelastics control. In terms of aeroelastics control, the exogenous input η_{v} is a further important input to the system, representing the global vertical gust velocity input positioned at the CG.

The measurement signals available to the controller to fulfill control goals that are mainly related to the RB dynamics of the aircraft, are the vertical acceleration at CG, Nz_{CG}, and the pitch rate q_{CG}. Zero tracking error on Nz_{CG} is guaranteed by an approach as presented in [50], where the open loop is directly augmented by an integrator as indicated by the index i in Fig. 6.26. The q_{CG} output turned out to be an effective lever for tuning of the short-period mode damping. Initial designs also revealed that Nz_{CG} and q_{CG} feedback signals are able to significantly shift the unstable phugoid mode. For that reason, an additional V_{TAS} measurement signal was not directly included in the $\mathscr{H}_\infty$ design, but instead a static V_{TAS} outer feedback loop was added to further improve the phugoid mode. For aeroelastic control, the modal

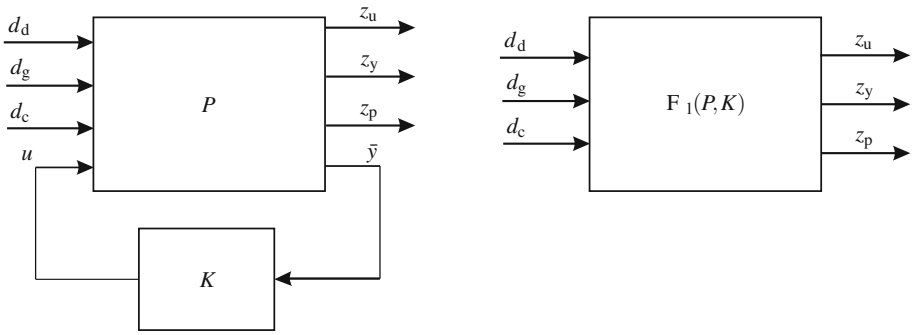

Fig. 6.27 Generalized closed-loop and lower LFT

wing bending signal $Nz_{\text{long.law}}$ is used to separate the vertical wing bending from the RB motion:

$$Nz_{\text{long.law}} = \left(\frac{\left(Nz_{\text{lw,k}} + Nz_{\text{rw,k}}\right)}{2} - Nz_{\text{CG}} \right), \tag{6.42}$$

The cut moment output My_5 serves as the only performance output during design and is selected to formulate performance specifications concerning load minimization in turbulence gust and maneuvers.

The design architecture in Fig. 6.26 represents a standard $\mathscr{H}_\infty$ mixed-sensitivity problem [76], with the corresponding generalized closed-loop representation as shown in Fig. 6.27. The main goal of the optimization is to minimize the cost function

$$\left\| \mathscr{F}_l(\mathbf{P}, \mathbf{K}) \right\|_\infty < \gamma, \tag{6.43}$$

where the transfer paths from the exogenous inputs $\boldsymbol{d}$ to the exogenous outputs $\boldsymbol{z}$ correspond to the single elements of the cost function matrix (6.43) and represent important performance paths of the closed loop. These are additionally weighted by suitable weighting functions $\mathbf{W}_i$ as indicated in Fig. 6.26 and represent the tuning knobs of the $\mathscr{H}_\infty$ mixed-sensitivity design. Therefore, a good understanding of the weighting functions and the actual closed-loop behavior is a prerequisite for a successful LPV design over a large parameter space. However, the choice of weighting function definition and the tuning process itself is extensive. Here, exemplarily the optimization with respect to limited control energy and the tuning of aeroelastic control is presented only.

6.5.3.2 Performance Weighting Function Definition

When trying to improve disturbance attenuation or tracking performance, it is of utmost importance to incorporate constraints concerning available control energy in a similar degree. In terms of a mixed-sensitivity problem, this can easily be ensured by including the control input $\boldsymbol{u}$ in the performance output vector [76]. Thereby, the function $\mathbf{KS}_\mathrm{o}$ appears in the cost function (6.43), where $\mathbf{S}_\mathrm{o} = (\mathbf{I} + \mathbf{GK})^{-1}$ is the output sensitivity function. In the low-frequency region, the singular value of $\mathbf{KS}_\mathrm{o}$ must be limited in order to avoid large control signals beyond saturation limits demanded by the controller $\mathbf{K}$. On the other hand, the bandwidth of control inputs must be constrained to avoid exceeding the corresponding rate limits. Since the output sensitivity function $\mathbf{S}_\mathrm{o}$ typically shows proportional behavior in the high-frequency region, the controller roll-off itself determines the roll-off of the closed-loop transfer function $\mathbf{KS}_\mathrm{o}$. Appropriate controller roll-off is obtained using a high-pass filter as performance weighting

$$\mathbf{W}_u = \begin{bmatrix} t_{u1}\frac{s+t_{u2}\cdot 1}{s+t_{u2}\cdot 100}, & 0 \\ 0 & t_{u3}\frac{s+t_{u4}\cdot 1}{s+t_{u4}\cdot 100}, \end{bmatrix}, \tag{6.44}$$

where t_{u1}, t_{u3} and t_{u2}, t_{u4} as the corresponding tuning factors to define the static gain (DC gain) and the corner frequency. For the control input $\eta_{\mathrm{EL_t}}$, the singular value plot of $\mathbf{KS}_\mathrm{o}$ for a nominal plant as well as exemplarily the inverse of the corresponding weighting function $\mathbf{W}_u^{-1}$ is shown in Fig. 6.28 (left).

As evident from that figure, the low-pass behavior of $\mathbf{W}_u^{-1}$ ensures the desired roll-off behavior of the closed loop. Increasing t_{u1} leads to both reduced bandwidth and reduced maximum control signals.

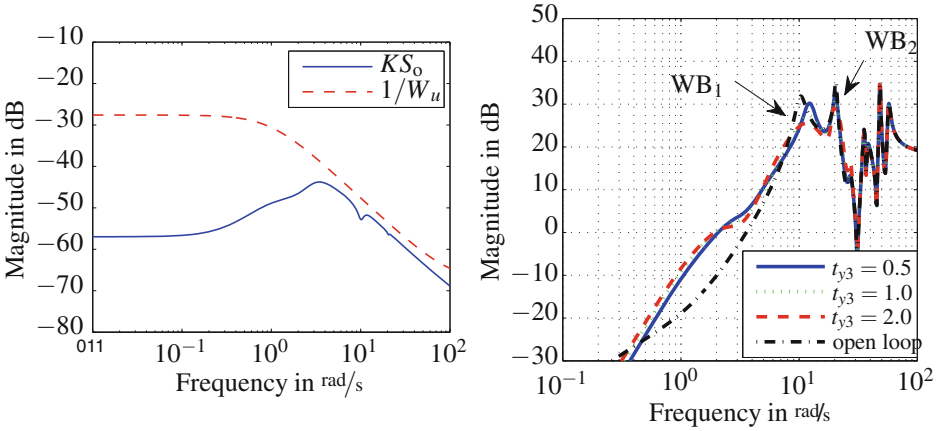

Fig. 6.28 $\mathbf{KS}_\mathrm{o}$ and $1/\mathbf{W}_u$ (*left*); effect on the singular value plot from η_v to $Nz_{\mathrm{long.law}}$ given by varying weighting factors t_{y3} (*right*)

The design requirements regarding reduction of structural loads and maximum vertical accelerations due to vertical gusts has proven to be difficult to achieve by frequency domain weighting without deterioration of the remaining specifications. Therefore, instead of minimization, an increase of these quantities is tried to be avoided by an appropriate selection of tuning weights. The damping of structural vibrations, on the contrary, is effectively addressed by shaping the output sensitivity function $\mathbf{S}_\mathrm{o}$ from the disturbance input at the output d_d to the measurement $Nz_{\mathrm{long.law}}$ and the disturbance transfer path from the vertical gust input η_v to $Nz_{\mathrm{long.law}}$. Therefore, the output disturbance weighting function matrix $\mathbf{W}_d$ and the output weighting function matrix $\mathbf{W}_y$,

$$\mathbf{W}_d = \begin{bmatrix} t_{d1} & 0 & 0 \\ 0 & t_{d2} & 0 \\ 0 & 0 & t_{d3} \end{bmatrix}, \quad \mathbf{W}_y = \begin{bmatrix} t_{y1} & 0 & 0 \\ 0 & t_{y2} & 0 \\ 0 & 0 & t_{y3} \end{bmatrix}, \tag{6.45}$$

at the corresponding position are both defined as a constant weight t_{d3} and t_{y3}. Constant weights have proven to be sufficient, due to the localized high gains of the flexible modes in the corresponding transfer functions. For controller tuning, the factors t_{d3} and t_{y3} are both increased until a slight shift of WB_1 respectively WB_2 is visible. Subsequently, t_{d3} is kept constant and t_{y3} is used for tuning of the structural damping of these two modes. This is presented in the singular value plot from η_v to $Nz_{\mathrm{long.law}}$ in Fig. 6.28 (right), where the results for a varying tuning factor t_{y3} are shown and $t_{y3} = 1$ represents a nominal setting. As can be seen, the damping is extremely sensitive on variations of t_{y3}. Considering WB_1, variations of the nominal setting $t_{y3} = 1$ by a factor of 2 respectively 0.5 leads to changes of the relative damping of around $\pm 50\,\%$. However, as expected not only modifications in the modes' damping ratios but also in their frequencies are apparent.

6.5.3.3 Robustness Against Fuel Uncertainty and Automated Tuning

In the previous section, aspects of nominal design were considered mainly. A subsequent step is to investigate the design optimization with respect to the robustness requirement for fuel-mass uncertainty. Basically, two different approaches were considered. First, a μ-synthesis design was investigated using an (LFT) model with a structured uncertainty block of order three. The high-accuracy and simultaneously low-order (LFT) model was provided by the project partner DLR (see Sect. 4.2). The obtained RP of the closed loop was compared to a second approach, a multi-model $\mathscr{H}_\infty$ approach. Despite the slightly deteriorated performance of the latter, the multi-model approach is chosen due to the reduced optimization complexity. Moreover, the closed-loop robustness against frequency and damping parameter uncertainty of the first two flexible modes was analyzed. Thereby, it turned out that the sensitivity to frequency uncertainty is higher than for damping parameter variations. However, basically a good robustness against these two uncertain parameters was revealed.

The manual tuning process is a time-consuming task for the large operating range to be considered. Therefore, an automatic tuning approach based on quality functions appropriate for performance specifications related to command response shaping and pole placement were defined. The resulting optimization function was minimized using the genetic algorithm of the optimization toolbox in MATLAB®. Using the automatic tuning approach, the weighting functions over the entire considered parameter space required for the subsequent LPV optimization were effectively determined, see [88].

6.5.4 Preliminary LPV Feedback Design

With the information gathered from the nominal $\mathscr{H}_\infty$ designs as described in the previous Sect. 6.5.3, the LPV controller optimization can be started. The LPV design is again divided into several sub-steps in order to improve the overall design process. First, several preliminary designs with single scheduling parameters are necessary in order to determine appropriate basis functions and an adequate gridding density, both with respect to closed-loop performance and computational complexity. Furthermore, closed-loop performance is investigated with respect to changing upper bounds for parameter rates. Finally, the LPV design optimization over the entire parameter space is presented and key items are discussed.

6.5.4.1 Basis Functions Selection and Gridding Density

For a successful LPV control optimization over a large parameter space, the effect of gridding density and the selection of basis function are essential aspects of the design. It is advantageous to consider always only one scheduling parameter for the parameter range of interest at the beginning. Exemplarily, the θ_{Ma} parameter is investigated in the following.

The solution matrices $\mathbf{X}(\boldsymbol{\rho})$, $\mathbf{Y}(\boldsymbol{\rho})$ of the LPV synthesis problem as outlined in Sect. 6.5.1.1 are matrix functions depending on the parameter vector $\boldsymbol{\rho}$. This leads to an infinite-dimensional optimization problem, so these matrices have to be approximated by a finite set of basis functions. Though much importance is attached to the choice of basis functions, a clear analytical procedure is not available. A general rule is to select the basis functions according to the parameter dependency of the open-loop system to be considered [93]. In previous works [4, 61, 85], where the LPV design methodology is applied to industrial applications, the matrix functions were defined by constant, linear and quadratic basis functions as

$$\mathbf{X}(\boldsymbol{\rho}) = \mathbf{X}_1 + \rho\mathbf{X}_2 + \rho^2\mathbf{X}_3,\ \mathbf{Y}(\boldsymbol{\rho}) = \mathbf{Y}_1 + \rho\mathbf{Y}_2 + \rho^2\mathbf{Y}_3. \tag{6.46}$$

For a larger subproblem in [85], only a constant and a linear term are utilized.

According to the results obtained from the open-loop analysis in Sect. 5.1, the parameter dependency of the short-period mode (SPM) on the θ_{Ma} parameter for the given parameter range $0.82 \leq \theta_{\mathrm{Ma}} \leq 0.88$ is nearly linear. Therefore, in a first step, constant and linear basis functions, $\mathbf{X}(\theta_{\mathrm{Ma}}) = \mathbf{X}_1 + \theta_{\mathrm{Ma}}\mathbf{X}_2$ and $\mathbf{Y}(\theta_{\mathrm{Ma}}) = \mathbf{Y}_1 + \theta_{\mathrm{Ma}}\mathbf{Y}_2$, were tested. Moreover, the parameter range was approximated by two finite parameter vectors $\mathbf{P}_{\theta_{\mathrm{Ma}},i}$ of different grid density:

$$\begin{aligned} \mathbf{P}_{\theta_{\mathrm{Ma}},1} &= [0.820, 0.832, 0.844, 0.856, 0.868, 0.880] \\ \mathbf{P}_{\theta_{\mathrm{Ma}},2} &= [0.820, 0.850, 0.880] \end{aligned} \tag{6.47}$$

The effect of the different gridding density on the controller is shown in Fig. 6.29, where a frequency magnitude response plot of the controller from Nz_{CG} to η_{EL_t} and the corresponding pole/zero map on a fine parameter validation grid $\mathbf{P}_{\theta_{\mathrm{Ma}},\mathrm{val}} = [0.820, 0.826, \ldots, 0.880]$ is presented. In the low-frequency region up until 5 rad/s, the magnitude curves lie denser for the finer gridding indicating the advantage given by the additional information of intermediate grid points. In the higher frequency region, on the contrary, the magnitude curves are similar, which can be explained by the restricted control authority of the elevator in this region. The pole/zero map shows a smooth characteristics for poles and zeros along the parameter variation for the fine gridding. For the rough gridding, however, sometimes poles and zeros form a cluster. The obtained γ values are $\gamma_{\mathrm{LPV,fine}} = 1.15$ and $\gamma_{\mathrm{LPV,rough}} = 1.25$ for

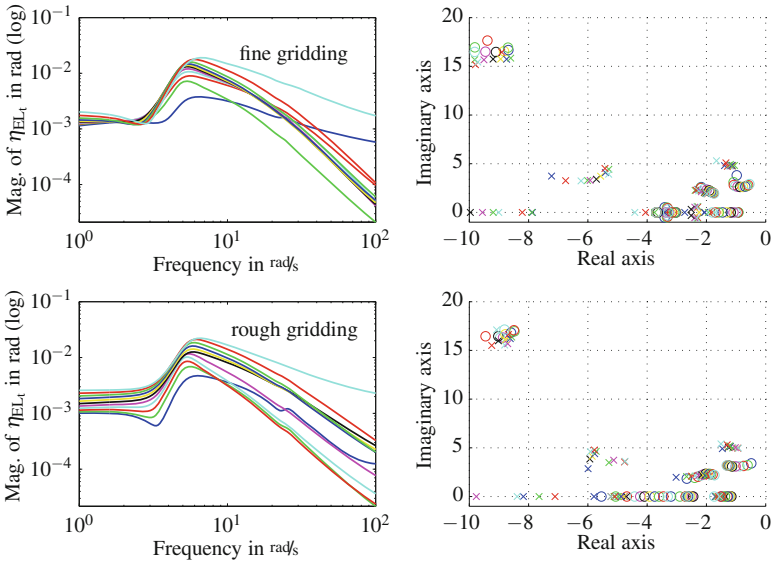

Fig. 6.29 Evaluation of LPV control law (depends on θ_{Ma} parameter only) dependency on different gridding density: frequency magnitude response plot from Nz_{CG} to η_{EL_t} (*left*) and corresponding pole zero map (*right*)

the fine and rough gridding, respectively, which emphasizes the advantage given by denser gridding.

A similar investigation was conducted with the matrix functions extended by the quadratic basis function terms $\theta_{\mathrm{Ma}}^2\mathbf{X}_3$ and $\theta_{\mathrm{Ma}}^2\mathbf{Y}_3$. Thereby, it turned out that the design is much more sensible to gridding density as in the linear case. Using a gridding according to $\mathbf{P}_{\theta_{\mathrm{Ma}},2}$ did not lead to useful results for intermediate points even though the design γ value $\gamma_{\mathrm{LPV,rough}} = 1.08$ was significantly lower than for the linear case. With $\mathbf{P}_{\theta_{\mathrm{Ma}},1}$, better results could be achieved, however, at few intermediate points the obtained control law was still defective. The same analysis was carried out for the θ_q parameter which lead to similar results.

6.5.4.2 Parameter Rate Setting

Additionally, the effect of the parameter rate setting on the optimization result was tested. Therefore, starting from a nominal setting of $|\dot{\theta}_{\mathrm{Ma}}| = 0.02\,1/\mathrm{s}$ and $|\dot{\theta}_{\mathrm{q}}| = 80\,\mathrm{Pa/s}$ was stepwise increased respectively decreased. Increasing the rate values leads to more conservative results indicated by an increased γ_{LPV} value and deteriorated overall performance. However, the basic characteristics of the control law and the resulting closed-loop behavior did not change.

6.5.5 Final LPV Design

With the information gathered from preliminary LPV designs, the parameter space was enlarged step-by-step. The $\mathscr{H}_\infty$ multi-model approach as shown in Sect. 6.5.3.3 has shown good RP results for an uncertain fuel-mass parameter and fixed θ_{Ma} and θ_q parameters. However, for varying θ_{Ma} and θ_q parameters, achieving robustness for the entire fuel-mass range turned out to be hard. Therefore, the fuel-mass parameter is included as additional parameter in the LPV design process, which is possible according to the design specifications, leading to a three-dimensional parameter space for the LMI optimization.

The associated high complexity of the optimization problem leads to either long computation times or to infeasibility of the problem. Therefore, the entire parameter space is split up into several subspaces. The rate of parameter variation is comparatively higher for θ_{Ma} and θ_q in comparison with θ_{fuel}, which makes robustness guarantees for those two parameters important. Moreover, the control law must provide sufficient robustness against fuel-mass uncertainty. Therefore, the fuel-mass parameter range was divided into three subspaces, where each subspace of θ_{fuel} is described by two grid points:

$$\mathbf{P}_{\theta_{\mathrm{fuel}},1} = [38, 63] \quad \mathbf{P}_{\theta_{\mathrm{fuel}},2} = [63, 91] \quad \mathbf{P}_{\theta_{\mathrm{fuel}},3} = [96, 100] \tag{6.48}$$

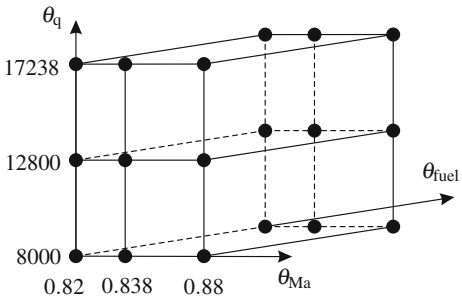

Fig. 6.30 Gridding of the parameter spaces used for design

Those fuel parameter regions which are not included in the optimization have to be robustly covered by the designed control laws $\mathbf{K}_{\theta_{\text{fuel}},i}(\theta_{\text{Ma}}, \theta_q, \theta_{\text{fuel}})$, $i = 1, 2, 3$. Especially in the low-fuel-mass region $\theta_{\text{fuel}} \leq 50\,\%$, it has been shown that $\mathbf{K}_{\theta_{\text{fuel}},1}$ fulfills the RP requirements to full extent. A continuously scheduled control law even for the fuel-mass parameter would have to be blended. However, blending of the control laws was not carried out in this work.

The parameter ranges of θ_{Ma} and θ_q parameter are described by three grid points, where the grid point vectors $\mathbf{P}_i$ are defined as

$$\mathbf{P}_{\theta_{\text{Ma}}} = [0.820, 0.838, 0.880] \quad \mathbf{P}_{\theta_q} = [8{,}000, 12{,}800, 17{,}238] \tag{6.49}$$

Therefore, each subspace is described through 18 grid point models as can be also seen in Fig. 6.30. The matrix functions $\mathbf{X}(\theta_{\text{Ma}}, \theta_q, \theta_{\text{fuel}})$, $\mathbf{Y}(\theta_{\text{Ma}}, \theta_q, \theta_{\text{fuel}})$ are approximated by constant and linear basis functions in θ_{Ma}, θ_q and θ_{fuel} according to:

$$\begin{aligned} \mathbf{X}(\theta_{\text{Ma}}, \theta_q, \theta_{\text{fuel}}) &= \mathbf{X}_1 + \theta_{\text{Ma}}\mathbf{X}_2 + \theta_q\mathbf{X}_3 + \theta_{\text{fuel}}\mathbf{X}_4 \\ \mathbf{Y}(\theta_{\text{Ma}}, \theta_q, \theta_{\text{fuel}}) &= \mathbf{Y}_1 + \theta_{\text{Ma}}\mathbf{Y}_2 + \theta_q\mathbf{Y}_3 + \theta_{\text{fuel}}\mathbf{Y}_4 \end{aligned} \tag{6.50}$$

The parameter rate of variation was set to $|\dot{\theta}_{\text{Ma}}| = 0.005\,1/\text{s}$, $|\dot{\theta}_{\text{q}}| = 240\,\text{Pa/s}$, and $|\dot{\theta}_{\text{fuel}}| = 0.1\,\%/\text{s}$. For the middle subspace represented by $\mathbf{K}_{\theta_{\text{fuel}2}}$, it has been shown that a reduction of the maximum rate for $\dot{\theta}_{\text{Ma}}$ and $\dot{\theta}_{\text{q}}$ to a quarter of the given value is necessary. Basically, this subspace has shown to be the computationally most demanding which could be relaxed through a further splitting.

With this optimization setup, one optimization run on an Intel® Core™ i7 PC takes between 6 and 17 h when using the LMI solver `mincx` from the Robust Control Toolbox of MATLAB® [5].

The obtained γ values are $\gamma_{\text{LPV},\theta_{\text{fuel}1}} = 6.9$, $\gamma_{\text{LPV},\theta_{\text{fuel}2}} = 4.9$ and $\gamma_{\text{LPV},\theta_{\text{fuel}3}} = 2.4$. Basically, an increase of the γ values in comparison with the LTI values is to be expected due to the given rate bounds and the approximation of the function space by the basis functions. However, these comparatively high values can be traced back to chosen high-gain performance weights at distinct parameter regions in order to enforce the desired performance specifications. Since the closed-loop validation

results are satisfactory as will be shown in Sect. 6.5.6, no further attempts were taken to reduce the obtained $\gamma_{\mathrm{LPV},\theta_{\mathrm{fuel}\,i}}$ values.

6.5.6 Validation of LPV Feedback Design

Basically, the validation models feature the following characteristics:

- The linear aircraft model comprises 19 aeroelastic modes and 14 lag states.
- The actuator dynamics is given by a θ_q-dependent nonlinear model.
- Control inputs are limited by nonlinear saturation and rate limits.
- Second-order Padé approximations for sensor delays.
- Second-order Butterworth filters for control measurement signals.

6.5.6.1 Closed-Loop Poles

One of the key performance requirements is the stabilization of the partly unstable SPM. Moreover, the open-loop poles must be shifted by the feedback law such that they provide satisfactory absolute and relative stability in the closed loop, except for the phugoid mode (PM), where an unstable real pole with a maximum real part of $\max(\mathrm{Re}(\lambda_{\mathrm{PM}})) < 0.1$ is still acceptable.

6.5.6.2 Command Response Behavior

For evaluation of the pitch response to a reference step command, essential flight mechanic data as well as the corresponding demanded control signals are presented in this section for the system response to a $r = 1.5\,\mathrm{g}$ reference command, where $g = 9.81\,\mathrm{m/s^2}$ is the gravity constant. Such large reference step represents a required validation maneuver leading to operation off the linearization point used for design.

The final command response behavior is available only if the feedback loop is connected with the feed-forward controller $\mathbf{K}_{\mathrm{ff}}$ where the results will be presented in a later section. The following results show the attainable tracking performance given by $\mathbf{K}_{\mathrm{fb}}$ alone and highlight the requirements which are not fully satisfied and therefore have to be improved by $\mathbf{K}_{\mathrm{ff}}$.

First, the command response is presented in Fig. 6.31 where the validation model does not contain the phugoid mode. Besides the outputs Nz_{CG}, q_{CG}, and Nz_{f}, the so-called C^* quantity is provided. This is a weighted linear combination of the vertical acceleration at the pilot position Nz_{f} and pitch rate q_{CG} and can be defined according to [13]:

$$C^* = Nz_{\mathrm{f}} + \dot{q}_{\mathrm{CG}} \frac{x_{\mathrm{CG}}}{\mathrm{g}} + q_{\mathrm{CG}} \frac{V_{\mathrm{m}}}{\mathrm{g}}, \tag{6.51}$$

where $V_m = 122\,\mathrm{m/s}$ [80] is an average velocity and x_{CG} is the distance from the CG to the pilot position.

Considering Nz_{CG}, which is the quantity to be tracked, in the upper left plot, it turns out that differences in the rise time as well as the maximum overshoot appear for the various parameter cases. Mainly the high Mach cases tend to yield slower command response. As it can be seen, it takes up to $t = 8\,\mathrm{s}$ for some systems to reach the desired end value. However, a large part fulfills the requirement of a rise time between 3 and 5 s with little overshoot.

The spread of the time characteristics of the pitch rate q_{CG} is, on the contrary, comparatively small over the parameter cases. The rise time is shorter than for Nz_{CG} and the maximum overshoot of 50 % is higher than the given requirement of 30 %. Considering the vertical acceleration at the cockpit position Nz_f, only moderate differences to the Nz_{CG} output appear. Also the C^* response is dominated by the shape of the Nz_f response.

The control signals demanded by the controller corresponding to Fig. 6.31 are provided in Fig. 6.32.

Comparing the obtained results with the actual limits for deflection and deflection rates

$$-30^\circ \le \eta_{EL_t} \le 15^\circ \quad -25^\circ \le \eta_{FL_{12}} \le 25^\circ \quad -25^\circ \le \eta_{FL_3} \le 25^\circ \tag{6.52}$$

$$-30^\circ/\mathrm{s} \le \dot{\eta}_{EL_t} \le 30^\circ/\mathrm{s} \; -40^\circ/\mathrm{s} \le \dot{\eta}_{FL_{12}} \le 40^\circ/\mathrm{s} \; -40^\circ/\mathrm{s} \le \dot{\eta}_{FL_3} \le 40^\circ/\mathrm{s} \tag{6.53}$$

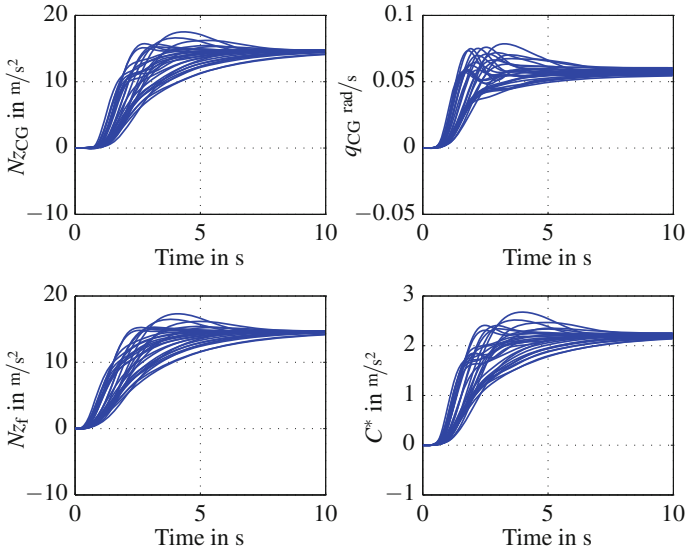

Fig. 6.31 Flight mechanic data time response to an $r = 1.5\,\mathrm{g}$ reference step command for representative validation models chosen from the parameter envelope

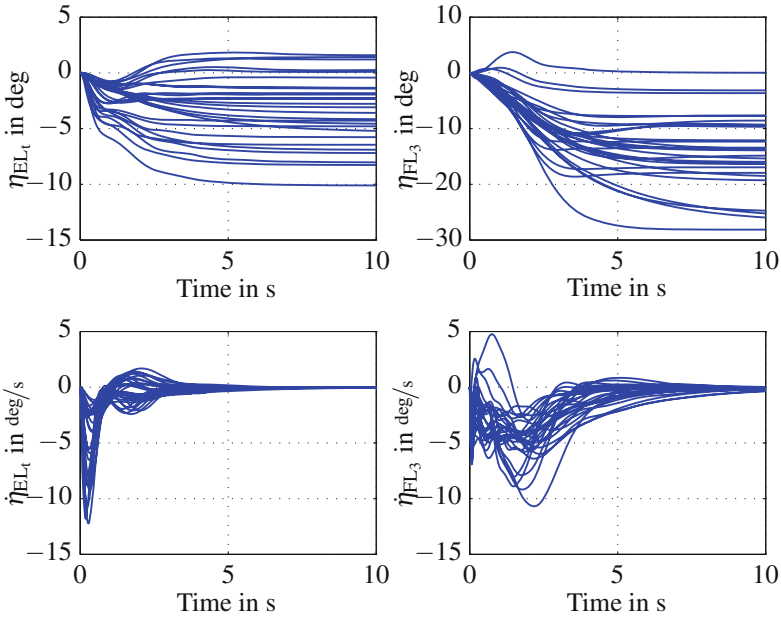

Fig. 6.32 Control input deflection and deflection rate time responses to an $r = 1.5$ g reference step command for representative validation models chosen from the parameter envelope

it turns out that the demanded values stay below the limits except for a few outliers. Especially the deflection rates are significantly lower for both actuators than the given limits, indicating that there is still enough potential left to make the pitch response faster. This was one of the main goals for feed-forward control law design, see Sect. 7.3.

6.5.7 Disturbance Response Behavior

In this section, the system disturbance response is validated using two representative $1 - \cos$ gusts input signals. In Fig. 6.33, the closed-loop and open-loop time responses for the longest considered gust length $L_{\text{gust}} = 152.4$ m are compared. This gust is the most important one in terms of maximum vertical accelerations and structural loads. The maximum acceleration respectively maximum load is given by their first peak in the time response. For a reduction of these peaks, it has been shown that feedback control requires high control effort in terms of maximum deflections and rates. Moreover, due to the corresponding necessary higher bandwidth, the robustness against high-frequency flexible modes deteriorates. Therefore, instead of minimizing of these maximum values, closed-loop acceleration and structural load levels equivalent to the open-loop level were aimed for.

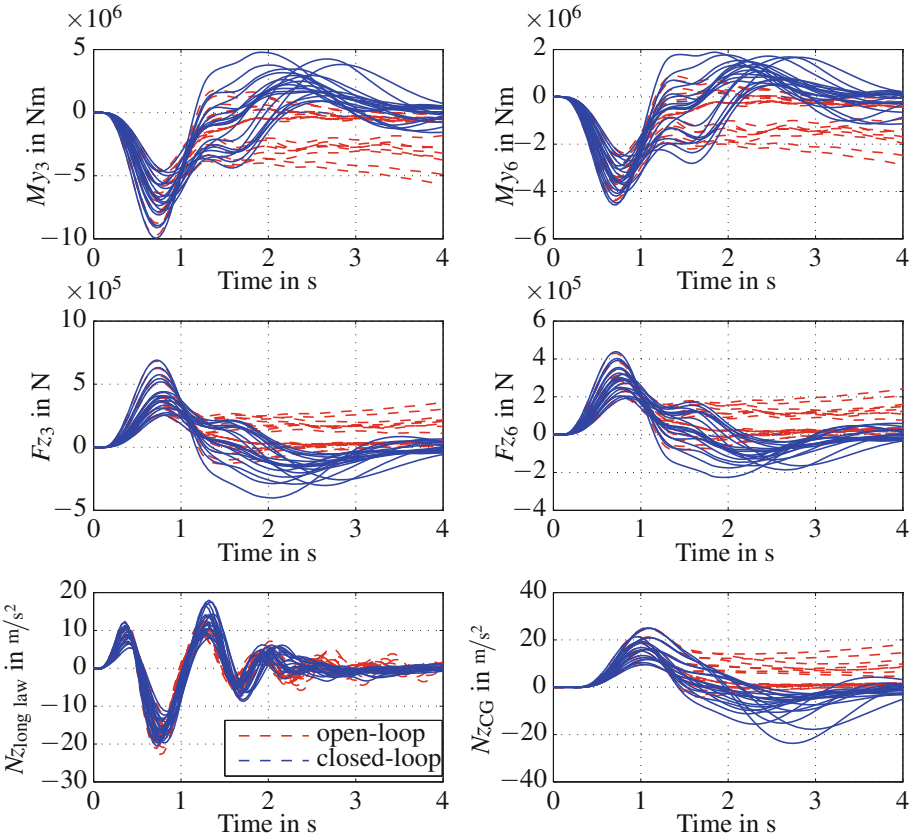

Fig. 6.33 Closed-loop and open-loop system time responses to gust number 10 for representative validation models chosen from the envelope

Considering the vertical acceleration Nz_{CG} response in the lower right plot of Fig. 6.33, it can be seen that the maximum closed-loop acceleration for various parameter cases is equivalent to those of the open-loop, represented by the dashed lines. For evaluation of structural loads, the load outputs My_3, My_6, Fz_3, and Fz_6 are exemplarily selected. Considering the responses it turns out that the design goal to avoid an increase of the load level is satisfied for both, the wing bending moment and the vertical force outputs.

The demanded control input time responses are provided in Fig. 6.34. During the design process, it has been shown that exceeding the rate limit of the elevator severely deteriorates the disturbance response and can even lead to instability. Therefore, special attention was paid to avoid too fast controller action of this control flap by appropriate frequency weighting. As can be seen in this figure, the maximum rate value for the elevator is $|\dot{\eta}_{EL_t}| = 28°/s$ and for the majority of cases $|\dot{\eta}_{EL_t}| < 20°/s$

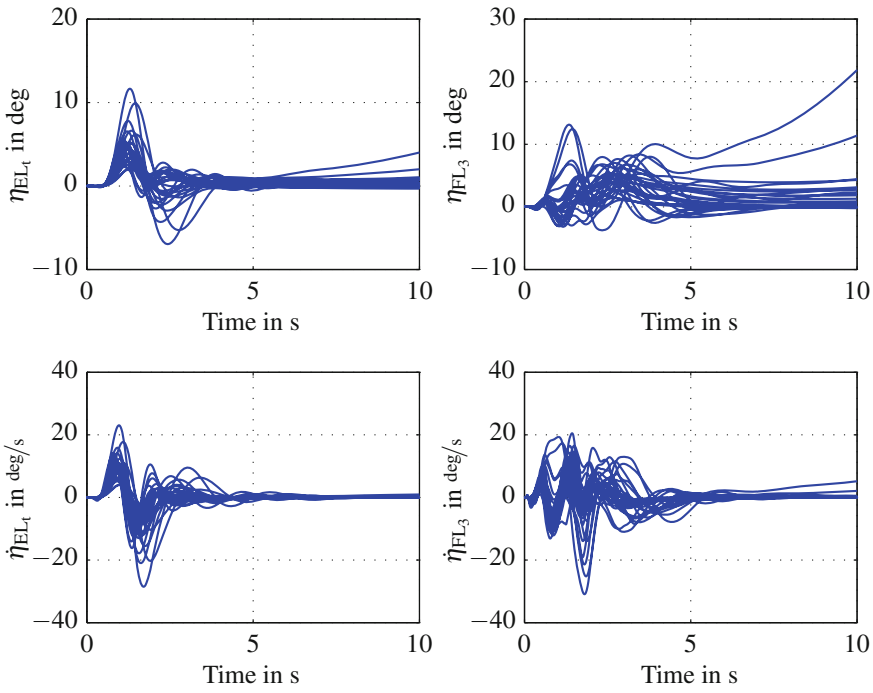

Fig. 6.34 Control input deflection and deflection rate time response to gust number 10 for representative validation models chosen from the envelope

holds, while $|\dot{\eta}_{FL_3}| < 29°/s$ holds. The maximum deflections $|\eta_{EL_t}| \leq 12°$, $|\eta_{FL_3}| \leq 13°$ also stay well within the limits.

Finally, the performance of aeroelastic damping is evaluated in the frequency domain. In Fig. 6.35, an open-loop/closed-loop comparison of the singular value plots is presented for several load outputs as well as Nz_{CG} and $Nz_{long.law}$ measurements. As can be seen from these plots, the damping of WB_1 is significantly increased and its magnitude significantly reduced for all considered outputs. The damping of WB_2, on the contrary, is hardly changed. No spillover effects arise for the modes not included in the design due to sufficient roll-off of the control law. There possibly exists some potential to further increase the control law bandwidth which can also have a positive effect on the damping performance for WB_2. This could be investigated in a subsequent design iteration step.

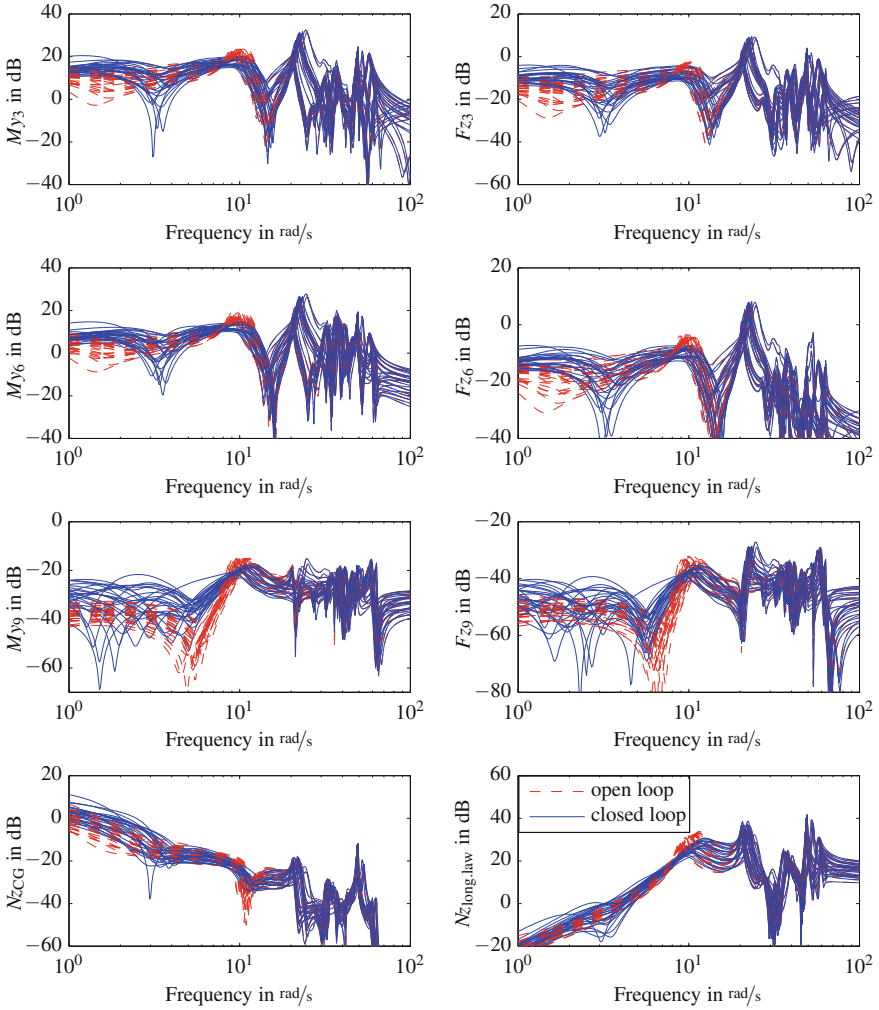

Fig. 6.35 Evaluation of aeroelastic control performance based on singular value analysis plots for several representative outputs

6.6 Low-Order Control Law Design

M. Hromčík and T. Haniš

6.6.1 Lateral $\mathscr{H}_\infty$-Optimal Control Law

Two different design approaches for design of lateral control augmentation system (CAS) for large BWB aircraft with flexible structure are elaborated and assessed in

this section. The most challenging design issues are related to coupling of rigid-body (RB) mechanics and flexible dynamics. First, a classical approach is employed giving rise to separate flight dynamics controller ($\mathscr{H}_2$-optimal, with sufficient roll-off at higher frequencies to avoid spillover) and an active damper for most prominent lateral flexible modes on top of that (mixed-sensitivity $\mathscr{H}_\infty$ design). This approach proves successful and has obvious advantages related to the design process complexity and to implementation/verification/testing. On the other hand, there is always a risk of potentially significant performance loss compared to a fully integrated design. For this reason, a fully integrated design is also presented in the form of a fixed-order multi-input multi-output (MIMO) $\mathscr{H}_\infty$-optimal flight control system (FCS) controller, obtained by means of direct non-convex non-smooth optimization using the dedicated software package HIFOO. Performance of both approaches is discussed. This design is carried out for the lateral motion of the NACRE BWB 750-passenger aircraft predesign model.

6.6.1.1 Introduction

Large lightweight aircraft structures and novel concepts, such as the BWB aircraft configurations, typically feature low-frequency structural vibrations modes, and their coupling with the flight mechanics modes may occur. Combined with significant dependency of the aircraft dynamics on flight parameters (Mach number / altitude / passengers / fuel volume and its distribution), severe flight control laws design challenges are to be expected.

Traditional methods for flight control design typically use nested single-input single-output (SISO) control loops and strongly structured control architectures [79]. These methods are based on detailed aircraft system analysis and exploit paths with weak coupling to obtain good results for conventional flight control design. However, multivariate methods, such as optimal control and particularly robust control design methods, are state-of-the-art for more complex flight control designs nowadays, especially useful for coupled and/or uncertain system dynamics. Two large groups of control design methodologies are optimal control design methods (for example, LQG control and the Kalman estimator [52]), as well as robust control design methods (see [76, 95] for fundamentals, or [7] for an aerospace-specific overview).

Two different approaches to lateral MIMO feedback CAS for NACRE BWB aircraft are presented in the following sections. They are namely a robust MIMO $\mathscr{H}_2/\mathscr{H}_\infty$ mixed-sensitivity controller and a low-order robust MIMO $\mathscr{H}_\infty$-optimal controller designed by direct fixed-order control design techniques. All controllers are designed to guarantee the desired closed-loop RB response (namely rise time and no-overshoot behavior to the reference change of the bank angle set point, attenuation of side-slip disturbance, and required damping ratio of the DR mode), and to dampen the first two anti-symmetric wing bending flexible modes. Performance and robustness of all controllers is demonstrated by means of MATLAB/Simulink® simulations, and their advantages and drawbacks are discussed.

6.6.1.2 BWB Aircraft Lateral Mathematical Model

The mathematical model of the BWB aircraft used for control law design consists of the flight mechanics model combined with the models of actuators and sensors. Actuator models are considered as second-order linear models augmented by saturations and rate limiters. Sensors are modeled as second-order Butterworth filters with time delays approximated by second-order Padé approximations. The mathematical model of the aircraft consists of the RB description (modeled as a 12th-order linear system separated into longitudinal and lateral dynamics), flexible modes (for design purposes just four modes are considered, depicted by an eighth-order linear model) and lag states. The overall model used for control law design is of order 52.

6.6.1.3 $\mathscr{H}_2/\mathscr{H}_\infty$ Mixed-Sensitivity Controller

A two-stage control law is devised—a separate CAS taking care of the flight dynamics (robust $\mathscr{H}_2$-optimal roll autopilot, with roll-off at higher frequencies), and an active damper for selected flexible modes ($\mathscr{H}_\infty$-optimal mixed-sensitivity controller tuned to first two anti-symmetric wing bending modes). Such an arrangement has obvious advantages—regarding tuning (both parts are designed/tuned independently), future flight testing (the active damper can be tested after the roll autopilot is implemented and approved, and it can be turned on/off at any time while keeping the aircraft well-controlled), safety (loss of the damper's functionality, for example, due to sensors failure, does not take the airplane out of control). The drawback is the potential reduction of performance compared to a fully integrated design where both flight dynamics and vibrational issues are handled by a single large MIMO controller.

Design Method

The lateral CAS (roll autopilot) is designed by $\mathscr{H}_2$ norm minimization of the generalized plant, encompassing the lateral RB dynamics itself (four states/outputs), two integrators (to ensure perfect steady-state tracking of a roll angle set point command and perfect steady-state attenuation of a side-slip disturbance), and two low-pass filters (for the required roll-off at higher frequencies—so that the flexible modes are left untouched and not excited by the controller). As all the RB states are measured, no observer needs to be implemented in fact and the resulting order of this CAS can be kept quite small (six states). Resulting controller features RS/RP for all considered mass cases (three passengers and five fuel cases).

On top of that, a robust MIMO controller is built by minimization of the $\mathscr{H}_\infty$ norm of the frequency-weighted mixed-sensitivity function. The wings' modal anti-symmetric sensor and anti-symmetric flaps make up the I/O groups. Loosely speaking, the closed-loop sensitivity function is kept small at selected frequency regions (in our case covering the wings' anti-symmetric modes) to assure for good performance (disturbance attenuation), while the complementary sensitivity function is kept small everywhere else (to ensure robustness—the design model becomes invalid outside the selected frequency region). A simple design model of eighth order was constructed

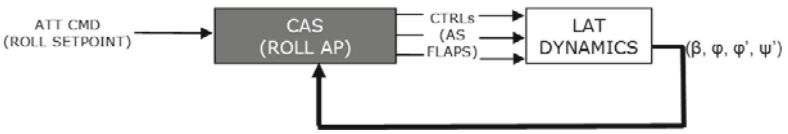

Fig. 6.36 Control augmentation system for $\mathscr{H}_2$ controller design. Anti-symmetrically operated wings ailerons are considered as control surfaces

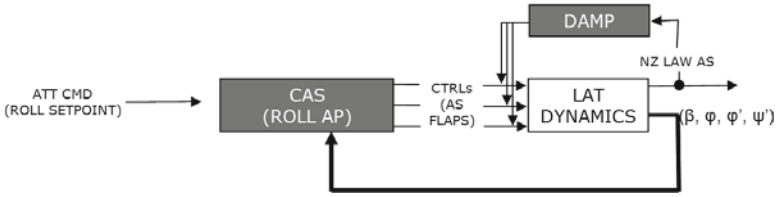

Fig. 6.37 Control augmentation system for $\mathscr{H}_2/\mathscr{H}_\infty$ controller design. Anti-symmetrically operated wings ailerons are considered as control surfaces

(modeling accurately the two modes and close region in the I/O channels). Two resonant weighting filters of second order are tuned to the frequencies and dampings of the anti-symmetric wing bending modes of a selected representative case for this purpose. The resulting $\mathscr{H}_\infty$ controller has 20 states.

The resulting damper (and also the overall CAS/damper combination) provides RS for all mass cases, significant improvement regarding damping of structural vibrations for most mass cases (more than 5 dB attenuation), and no effect on vibration damping for the remaining cases. These findings and the overall performance of the designed controller and its respective parts are visualized in Figs. 6.36 and 6.37.

$\mathscr{H}_2/\mathscr{H}_\infty$ Control Results

Brief assessment of the controller performance is given in the text above (regarding robustness and performance). A set of selected characteristics is now given to document these findings.

Note that very good performance is achieved for those cases that do not vary much in the frequency of the targeted modes (Fig. 6.38 left). However, even for the other cases (Fig. 6.38 right), some performance improvement is achieved, and RS is assured (Figs. 6.39, 6.40, and 6.41).

Required response to bank angle set point is achieved. Note marginal improvement of the response when the damping system is connected (though it was not intended to influence the flight dynamics in fact). As stated above, the flight dynamics part contains integrated yaw damper and side-slip compensator. Gain and phase margins for the complete designed controller have been evaluated. RS of the closed loop for all mass cases is achieved. For simultaneous, independent, worst-case variations in the individual channels the gain margin ranges from 1.9 to 3.7 dB, and the phase margin ranges from 12 to 23°, depending on the mass case.

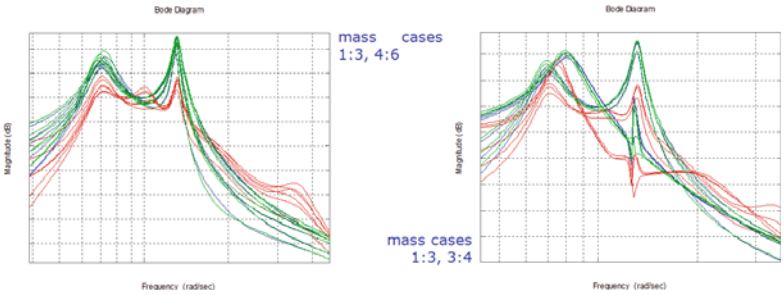

Fig. 6.38 Wing bending modes attenuation. Open loop (*green*), $\mathscr{H}_2$ control (*blue*), and $\mathscr{H}_2/\mathscr{H}_\infty$ control (*red*)

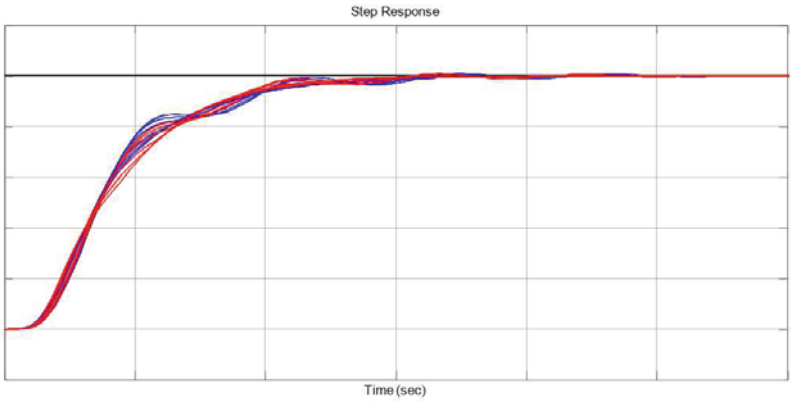

Fig. 6.39 Roll reference tracking. $\mathscr{H}_2$ control (*blue*) and $\mathscr{H}_2/\mathscr{H}_\infty$ control (*red*)

6.6.2 Non-convex Non-smooth Optimization

In recent years, great progress has been made in the challenging area of non-convex non-smooth optimization solvers. In contrast to more traditional setups, such problems are highly non-convex and no differentials or Jacobians can be used to navigate the search for even a local optimum. The solvers rely on a Broyden–Fletcher–Goldfarb–Shanno (BFGS) variable metric (quasi-Newton) method [16, 17, 51], or non-smooth modifications of Virginia Torczon's multidirectional search (MDS) [2, 81, 82].

Related numerical software has been soon delivered in the form of freeware and commercial package like Hybrid Algorithm for Non-Smooth Optimization (HANSO) based on the BFGS method.

As people from the systems and control community quickly realized, such algorithms and tools can be successfully applied to resolve some control design challenges that are otherwise almost untractable for real-life-size data. Didier Henrion and Mike Overton seem to get furthest, proposing a new methodology for direct design of

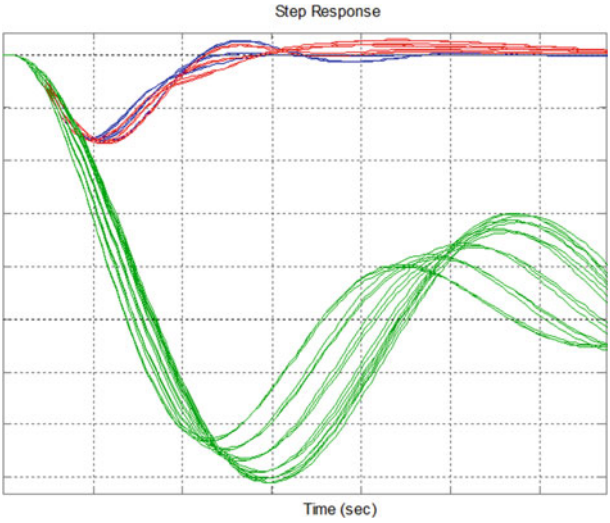

Fig. 6.40 Side-slip disturbance rejection. Open loop (*green*), $\mathscr{H}_2$ control (*blue*), and $\mathscr{H}_2/\mathscr{H}_\infty$ control (*red*)

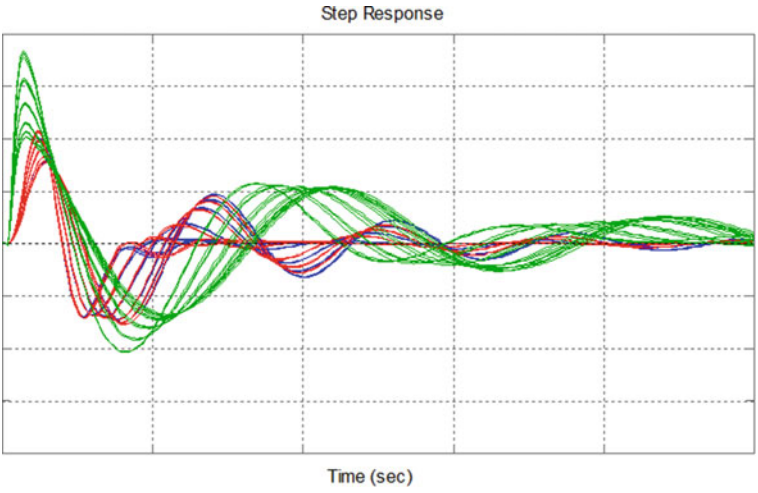

Fig. 6.41 Yaw rate damper. Open loop (*green*), $\mathscr{H}_2$ control (*blue*) and $\mathscr{H}_2/\mathscr{H}_\infty$ control (*red*)

low-order $\mathscr{H}_\infty$-optimal controllers in the 2000s [3, 15, 38, 39, 59], and delivering a related freeware package HIFOO.

The HIFOO package has already attracted attention of controls designers in the miscellaneous field [22, 25, 47, 63, 65, 87]. Regarding flight controls design, the first attempt was made in master thesis [59], where the applicability of the package

was approved by a means of a textbook example of a wing-leveler controller for an F-16 aircraft.

In this section, this approach and software will be employed to design, at one-shot, a robust, full-featured, $\mathscr{H}_\infty$-optimal longitudinal control law for a BWB highly flexible near-future airliner concept, following the recommended and industry-approved structure for this CAS. Performance of the result is assessed by means of high-fidelity simulations and classical, industry-standard robustness analysis results.

6.6.3 Direct Approach to Fixed-Order $\mathscr{H}_\infty$-Optimal Control Design

For reader's reference, the basic principles of the underlying algorithms used for direct $\mathscr{H}_\infty$ fixed-order control design are summarized in brief in this section, adopted from [38]. Interested readers are advised to consult the original paper for a more detailed and rigorous treatment.

The aim of the HIFOO algorithm is to deliver a stabilizing $\mathscr{H}_\infty$-optimal controller for given n LTI systems. The criterion for $\mathscr{H}_\infty$ optimization is expressed by the generalized plant setup. The algorithm has two phases. In each phase, the main workhorse is the BFGS optimization algorithm, which is surprisingly effective for non-convex, non-smooth optimization. The user can provide an initial guess for the desired controller; if this is not provided, HIFOO generates randomly generated initial controllers, and even when an initial guess is provided, HIFOO generates some additional randomly generated initial controllers in case they provide better results. The first phase is stabilization: BFGS is used to minimize the maximum of the spectral abscissa of the closed-loop plants. This process terminates as soon as a controller is found that stabilizes these plants, thus providing a starting point for which the objective function for the second phase is finite. The second phase is optimization: BFGS is used to look for a local minimizer of the controllers found in the first phase. The HIFOO control design method searches for locally optimal solutions of a non-smooth optimization problem that is built to incorporate minimization objectives and constraints for multiple plants. The optimization problem is introduced as a set of augmented plants, see Fig. 6.42, commonly used in robust control approaches. First, the controller order is fixed at the start, allowing for low-order controller design. Second, Lyapunov or lifting variables are introduced to deal with the conflicting specifications. The resulting optimization problem is formulated on the controller coefficients only, resulting in a typically small-dimensional non-smooth non-convex optimization problem that does not require the solution of large convex sub-problems, relieving the computational burden typical for Lyapunov LMI techniques. An algorithm that searches only for local minimization is used for the sake of computational time. While no theoretical guarantee can be given on the result's quality, in practice it often yields surprisingly efficient control laws.

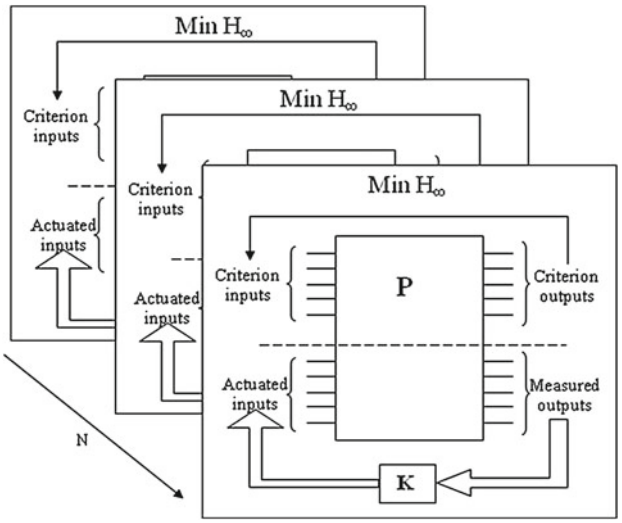

Fig. 6.42 $\mathscr{H}_\infty$ fixed-order optimization setup

6.6.3.1 Lateral Fixed-Order $\mathscr{H}_\infty$-Optimal MIMO Robust Controller

Similar as in the previous section, the two different control goals are targeted, but this time by one integrated controller. One job of the control law is to provide autopilot functionality. The autopilot consists of a stability augmentation system (SAS) (a DR mode damper) and a CAS (roll and side-slip angle reference tracking). Other roles of the control law are related to vibrations and loads attenuation.

The lateral integrated CAS was designed as a 2DoF architecture using the fixed-order optimization approach to keep control law order low. The resulting, extremely simple controller (in this case, just third-order control law was used) was calculated using the HIFOO toolbox. The overall lateral CAS consists of a RB autopilot (roll and side-slip tracker with DR mode damper) and an active feedback damper for structural modes. The lateral CAS setup can be seen from Fig. 6.43. Two reference signals are used as inputs into the feed-forward part of the controller (roll and side-slip setpoints). The side-slip reference signal is usually set to zero, and then the CAS provides coordinated turn functionality.

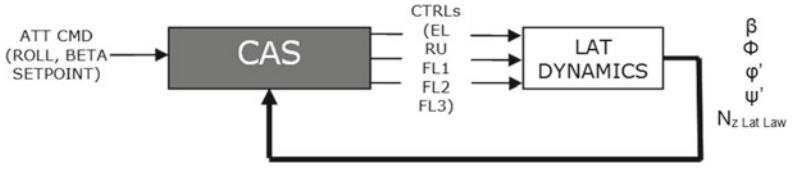

Fig. 6.43 Control augmentation system for HIFOO

The control surfaces used by the CAS are all ailerons (anti-symmetrically actuated FL1–FL3), rudders (RU) and elevators (symmetrically actuated EL). Measured signals are lateral RB variables at CG (side-slip angle, roll angle, roll rate and yaw rate), for structural modes control we have selected a lateral wing bending acceleration modal sensor in an anti-symmetrical setup. The resulting control law (autopilot and structural modes controller) provides RS as well as RP for all 18 cruise condition cases (six fuel and three passenger cases).

6.6.3.2 HIFOO Control Results

The achieved improvement of damping of the first and second wing bending modes can be seen from Fig. 6.44. Simultaneously, the DC gain is preserved for all cases. RP can be approved by the bank angle reference signal tracking response plotted in Fig. 6.45 (left). Responses for a sequence of two steps are shown and one can see sufficiently fast response with acceptably small overshoot.

Side-slip disturbance attenuation functionality is investigated in Fig. 6.46 (left). One can see complete vanishing of side wing influence in a few second and without inducing oscillation for major part of cases. DR mode damping is investigated in Fig. 6.46 (right).

Gain and phase margins for the complete designed controller have been evaluated. RS of the closed loop for all mass cases is achieved. For simultaneous, independent,

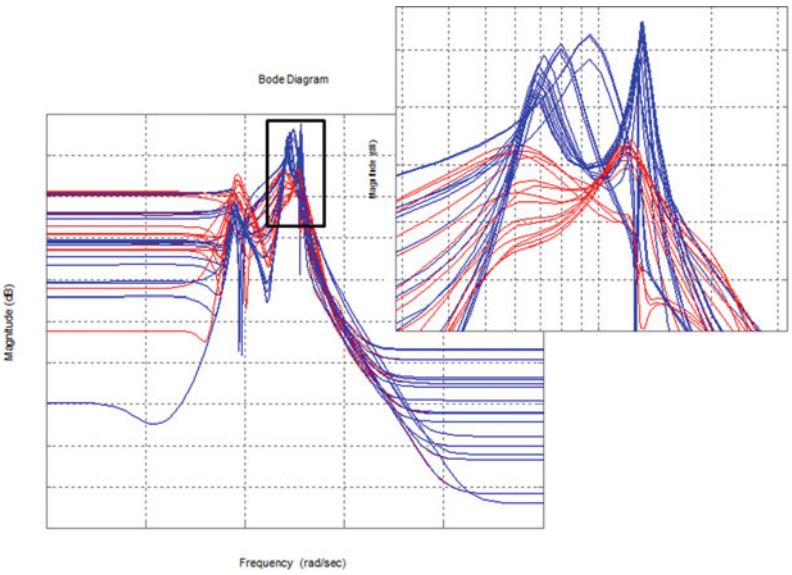

Fig. 6.44 Wing bending mode attenuation. Open loop (*blue*), closed loop (*red*)

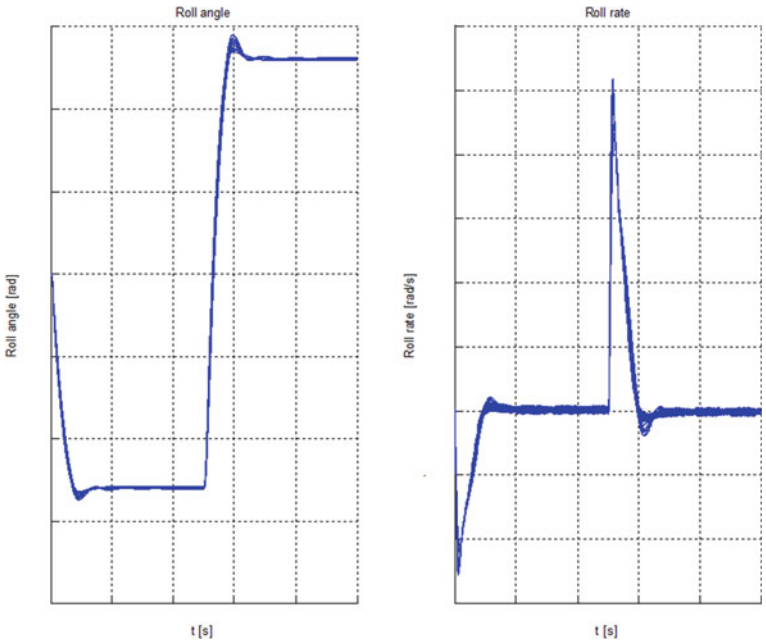

Fig. 6.45 Bank angle and roll rate reference signal tracking

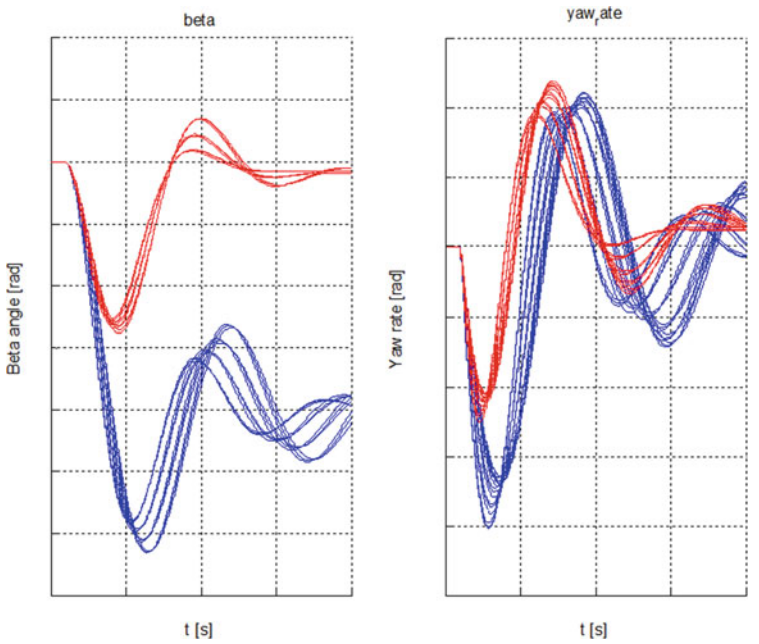

Fig. 6.46 Side-slip angle disturbance attenuation (*left*) and Yaw rate damping (*right*). Open loop (*blue*), closed loop (*red*)

worst-case variations in the individual channels the gain margin ranges from 0.8 to 2.6 dB, and the phase margin ranges from 5 to 16°, depending on the mass case.

6.6.4 Longitudinal $\mathscr{H}_\infty$-Optimal Control Law of Prescribed Structure

Advanced non-convex non-smooth optimization techniques for fixed-order $\mathscr{H}_\infty$ robust control are proposed in this part for design of FCSs with prescribed structure. Compared to classical techniques—tuning of and successive closures of particular SISO loops like dampers, attitude stabilizers, etc.—all loops are designed simultaneously by means of quite intuitive weighting-filters selection. In contrast to standard optimization techniques, such as $\mathscr{H}_2$ or $\mathscr{H}_\infty$ optimization, the resulting controller respects the prescribed structure in terms of engaged channels and orders (for example, P, PI, PID controllers). In addition, robustness with respect to multi-model uncertainty is also addressed which is of most importance for aerospace applications as well. Such a way, robust controllers for various Mach numbers, altitudes, or mass cases can be obtained directly, based only on particular mathematical models for respective combinations of the flight parameters.

6.6.4.1 Introduction

The flight dynamics, exhibiting many oscillatory or unstable modes for a typical aircraft, as well as the automatic or semi-automatic regimes of modern autopilots call for control synthesis methods that can effectively address these issues. Traditionally, classical tools for SISO loops tuning are used successively to deliver a complex FCS composed of a few smartly pre-selected channels, such as pitch, roll, or yaw dampers for suitable dynamics modifications (stability augmentation), subsequent attitude hold autopilots, automatic navigation loops, etc. Typically, a significant number of iterations and "backstepping" is required as the higher-level loops interact partially with the lower-level predesigned parts. Historically, frequency response methods were developed first in the 1930s and 1940s [11, 32, 56, 58, 60], and they remain arguably the most commonly used methods until today [14].

Since the 1960s, results of optimal control theory have been used extensively for aircraft control design as a powerful alternative to the classical approach. The methods are typically purely multi-input multi-output (MIMO) in nature, delivering all channels of the resulting controller in "one shot". The design procedure is controlled indirectly by means of selection of some weightings, being it constant matrices for LQ or LQG approach [53, 95], or LTI shaping filters for the $\mathscr{H}_2$ or $\mathscr{H}_\infty$-optimal control [7, 76, 95]. Nevertheless, the structure of the FCS is typically very hard or impossible to imprint, and the order (complexity) of the resulting controller can

become unacceptably large as well. In this regard, the classical methods still have quite a lot to offer.

Robustness of the flight controller is of utmost importance. The flight dynamics changes considerably as the aircraft properties vary over time (fuel amount, center of gravity position) and as the flight parameters change (altitude, airspeed, attitude angles). Classical and optimal controllers must fulfill the robustness requirements which is typically acknowledged by means of stability margins analysis (gain margin, phase margin [10, 18, 19, 53, 76, 95]) and extensive simulations for selected important points of the flight envelope. Nevertheless, neither of these methodologies supports incorporating the robustness requirements explicitly into the design procedure. In contrast, the robust control design approach, developed in the 1980s through the 2000s [26, 30, 31, 95] relies on the mathematical formulation of the uncertainty as one of the control design parameters. Most prominent methods are unstructured $\mathscr{H}_\infty$ optimization [7, 76, 95], structured $\mathscr{H}_\infty$ control (μ-synthesis, DK-iterations [6, 27–29, 95], robust loopshaping [55], and others). They all have been naturally accepted by the aerospace controls community, giving rise to significant implementations [9, 35, 44, 62].

One may ask if there is not a way to combine the benefits of the classical, optimal, and robust approaches—the convenient weighting-filters formulation of the optimal control synthesis, hierarchical and comprehensive structure of the classical controllers, and insensitivity to parameters uncertainties of the robust control designs. Indeed, some attempts have been made, based either on linear quadratic optimization (static output feedback design [77–79]), based on mixed-sensitivity $\mathscr{H}_\infty$ optimization with static output constraints [49, 75], or by designing a mixed $\mathscr{H}_2/\mathscr{H}_\infty$-optimal controller of fixed order based on a homotopy algorithm [91].

In this section, a completely different approach toward this goal is suggested, though. Thanks to the practical availability of computer-aided control systems design (CACSD) tools based on most recent non-convex non-smooth optimization techniques, direct synthesis methods can be employed to deliver a complex FCS that is structured (features pre-selected channels only), of fixed low order (consisting of, for example, P, PI, or lead-lag controllers), optimal in the $\mathscr{H}_\infty$ norm sense (for bandwidth setting, reference tracking, disturbance attenuation requirements), and robust with respect to a multi-model uncertainty (covering a selected number of airspeed, mass, altitude, or other cases).

The rest of this section is structured as follows. In Sect. 6.6.4.2, the method of formulating and solving a structured longitudinal CAS design process with HIFOO is shown. The main result of the paper is the case study presented in Sect. 6.6.4.3 (where advanced case study is presented). The procedure toward a structured, low complexity, and robust lateral FCS is elaborated in detail for a nonlinear model of a BWB-type aircraft, as a proof of practical usefulness of the proposed modern techniques for flight controls design purposes.

6.6.4.2 Longitudinal Structured Control Law with HIFOO

We propose a systematic methodology for a one-shot, robust, full-featured, $\mathscr{H}_\infty$-optimal longitudinal control design, for a multi-model case covering substantial points of the flight envelope. This methodology literally combines advantages from modern controller design techniques involving $\mathscr{H}_\infty$ or $\mathscr{H}_2$ optimization with a hierarchical approach for aircraft control system design. The HIFOO toolbox allows to preserve the property of physical meaning of each control system loop (which is one reasonable argument of aircraft control system engineers) and removes disadvantages of loop-by-loop tuning of control systems. On the other hand, the well-known robust control design approach based on the generalized plant setup and a corresponding criterion definition (for example, in the $\mathscr{H}_\infty$ sense) in the frequency domain can be followed also in the HIFOO formulation. Thereby, weighting filters like those used in [70, 71, 89, 90] can be included to produce MIMO controllers. Still, the HIFOO toolbox can be understood as an extension to the classical control design techniques. Due to the local optimization carried out by HIFOO, providing a suitable starting point in terms of an initial controller can significantly save computation time. Standard hierarchical approaches can then be used as a promising initial control law.

Algorithm:
Given:

- Set of systems for control design
- Structure of resulting control law
- Optimization criterion.

Output:

- Robust LTI control law with predefined structure.

- **Step 1:** Specify generalized plant set up (define measurable outputs/actuated inputs and criterion by performance inputs/outputs).
  - **Recommendations:** It is needed to select measurable outputs/actuated inputs in correspondence with structure to be designed.
- **Step 2:** Specify performance requirements by weighting filters.
  - **Recommendations:** Depends on the control problem. Typically, low-pass filters are used for reference signal tracking, and bandpass filters are used for vibration modes attenuation.
- **Step 3:** Specify the control law structure.
  - **Recommendations:** The structure needs to be defined by the controller's Rosenbrock matrix. There can be more than one representation, whereby a minimal realization should be aimed for.
- **Step 4:** Specify the starting control law if any is available, otherwise it will be generated randomly.

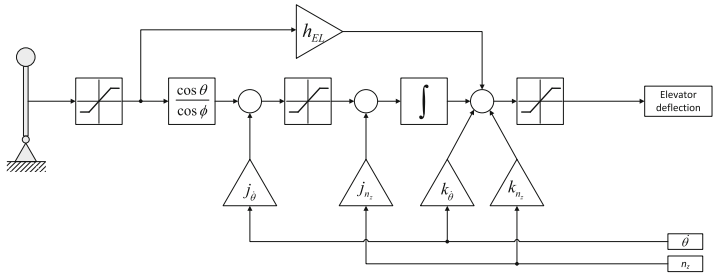

Fig. 6.47 Longitudinal control augmentation system (adopted from [13])

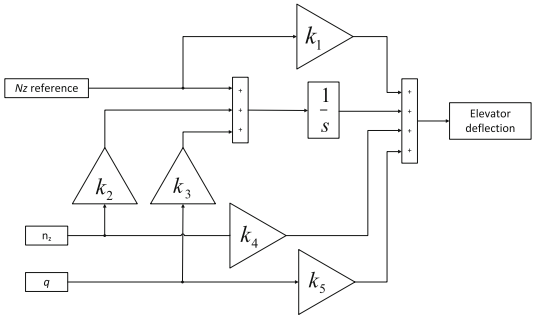

Fig. 6.48 Normal acceleration reference signal tracking control augmentation system with structure

  - **Recommendations:** The suitable choice of a starting point is critical to save optimization time. Control laws designed by classical approaches can be a suitable choice.

- **Step 5:** Solve the design problem using the HIFOO toolbox.
  - **Recommendations:** The involved optimization does not guarantee global optimality; therefore, it is usually required to run the optimization several times to reduce the risk of getting caught in mediocre local optima.

A longitudinal CAS of extremely low order (first-order control law) with imprinted structure was designed by the HIFOO toolbox. The structure of the control law is shown in Fig. 6.47, respectively Fig. 6.48 (with mapping of constants (6.54)).

$$\begin{aligned} k_1 &= h_\eta \\ k_2 &= j_{nz} \\ k_3 &= j_{\dot{\theta}} \\ k_4 &= k_{nz} \\ k_5 &= k_{\dot{\theta}} \end{aligned} \tag{6.54}$$

It is a common hierarchical control law used for an asymptotic tracking of the aircraft normal acceleration reference signal (see [13, 79]). The hierarchical control law design was usually done in an iterative manner, using background knowledge

of the physical meaning of the single loop to reach the required performance. The optimization technique is addressed now to design the overall control law in one shot. $\mathscr{H}_\infty$-performance criteria can be introduced to design robust control laws with predefined structure and order. The extremely low-order and structural complexity of the overall control law (with preserved robust behavior and control performance of full MIMO high-order control laws) is very important for final on-board implementation. It reduces necessary computational effort and therefore hardware demands for on-board equipment, which is closely connected with reliability and price of implementation. For other possibilities of high-order MIMO CAS designs, see [70, 71, 89, 90]. Control surfaces used by CAS are symmetrically actuated beaver tails (denoted as BT) and elevator (denoted as EL), in our case both flaps are collectively actuated as one. Measured signals are longitudinal RB variables at CG, namely normal acceleration (denoted as Nz_{CG}) and pitch rate (q). Highly valuable feature of $\mathscr{H}_\infty$ optimization is the possibility to introduce the concept of robustness. The HIFOO toolbox will be used, in this particular case, to cover multiple plants, each representing different fueling points in the flight envelope to end up with a longitudinal CAS robust with respect to fueling. The augmented plant used for control law design is shown in Fig. 6.49.

The signals in the augmented plant are divided into exogenous inputs and outputs (which represent control law performance by definition of the optimization criterion), as well as measured outputs and actuated inputs according to Fig. 6.42. The plant G represents aircraft longitudinal dynamics itself and weighting filters W represent the definition of performance criterion in the frequency domain. At this point, the structure of the controller can be introduced into HIFOO by prescribing zero entries in the controller's Rosenbrock matrix. Let the state-space representation of the controller be $K \cdot a$, $K \cdot b$, $K \cdot c$, and $K \cdot d$, then its Rosenbrock matrix is:

$$K = \begin{bmatrix} K \cdot a & K \cdot b \\ K \cdot c & K \cdot d \end{bmatrix}, \tag{6.55}$$

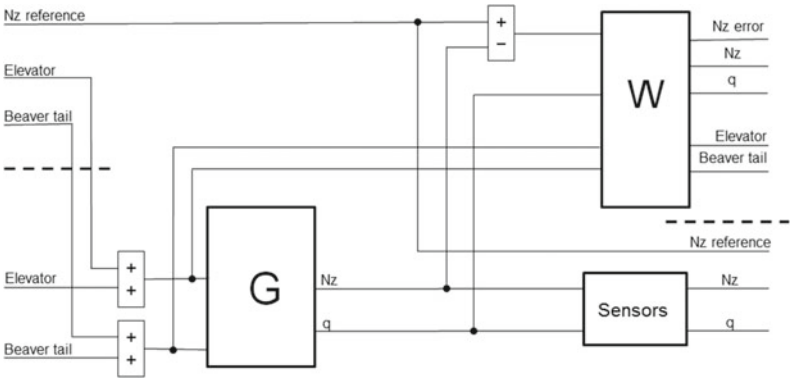

Fig. 6.49 Augmentation plant set up used for longitudinal control law design

with the augmented plant setup shown in Fig. 6.49 and the desired structure of the controller as shown in Figs. 6.47 and 6.48 the controller can be written in the form:

$$A_K = 0 \tag{6.56}$$

$$B_K = \begin{bmatrix} 1 & -k_2 & k_3 \end{bmatrix} \tag{6.57}$$

$$C_K = \begin{bmatrix} 1 \end{bmatrix} \tag{6.58}$$

$$D_K = \begin{bmatrix} k_1 & k_4 & k_5 \end{bmatrix}. \tag{6.59}$$

Consequently, the controller's Rosenbrock matrix is

$$K = \begin{bmatrix} 0 & 1 & -k_2 & k_3 \\ 1 & k_1 & k_4 & k_5 \end{bmatrix}. \tag{6.60}$$

The HIFOO toolbox is applied now to carry out the fixed-order optimization with a predefined structure of the controller. The final control law is an integrated first-order multi-input single-output (MISO) controller with predefined structure and can be used as an integrated longitudinal CAS. However, because of the structure it is possible to disassemble it into a hierarchical structure of SISO loops, which can be used one-by-one as a SAS itself (pitch rate damper and normal acceleration damper) as it is known from text books and longitudinal CAS, in this case a normal acceleration reference signal tracker.

6.6.4.3 BWB Case Study

Mathematical Model of Longitudinal Aircraft Dynamics

This longitudinal CAS control design is carried out for the ACFA 2020 BWB aircraft. A variant of the longitudinal ROMs obtained in Sect. 4.1 are utilized in the following. They contain both flight mechanics and aeroelastic effects as well as their coupling. A set of linearized state-space systems for various parameter values of fuel and payload mass (at fixed cruise altitude and airspeed) is available:

$$\begin{aligned} \dot{\mathbf{x}} &= \mathbf{A} \cdot \mathbf{x} + \mathbf{B} \cdot \boldsymbol{u} \\ \mathbf{y} &= \mathbf{C} \cdot \mathbf{x} + \mathbf{D} \cdot \boldsymbol{u}, \end{aligned} \tag{6.61}$$

where the state vector $\mathbf{x}$ is composed of the six flight mechanic states (x-position X, body forward speed u, altitude Z, body down speed w (it is proportional to angle of attack α), pitch angle θ and pitch rate q), 12 elastic states (six symmetrical structural

modes), as well as seven aerodynamic lag states. The states X (x-position) and Z (altitude) are neglected in this study. Utilized inputs u for control design are:

- Symmetric Extended Elevator deflection δ_{EEL} (in rad) and deflection rate $\dot{\delta}_{\mathrm{EEL}}$ (in rad/s).
- Symmetric Elevator deflection δ_{EL} (in rad) and deflection rate $\dot{\delta}_{\mathrm{EL}}$ (in rad/s).

The Extended Elevator and Elevator control surfaces are coupled and actuated simultaneously (will be notated as δ_{EL}) in case of longitudinal control law. The actuator dynamics are modeled via second-order low-pass filters.
Utilized outputs for control design are:

- Pitch rate q (in rad/s)
- Normal acceleration Nz_{CG} (in $\mathrm{m/s^2}$)

where in both sensor signals 160 ms time delay (due to signal processing latency, modeled via a second-order Padé approximation) and low-pass Butterworth filters of second order were considered.

Simulations

The resulting longitudinal control law performance is presented in this section. First are presented linear model simulation in MATLAB® and than nonlinear MATLAB/Simulink® model is involved to demonstrate longitudinal control law capabilities. Position of the closed-loop poles is constrained by required relative damping of 0.5 for all RB poles, the only exception is for the phugoid mode, which can have even one real unstable pole with time period less than 0.1. The closed-loop pole locations can be seen in Fig. 6.50.

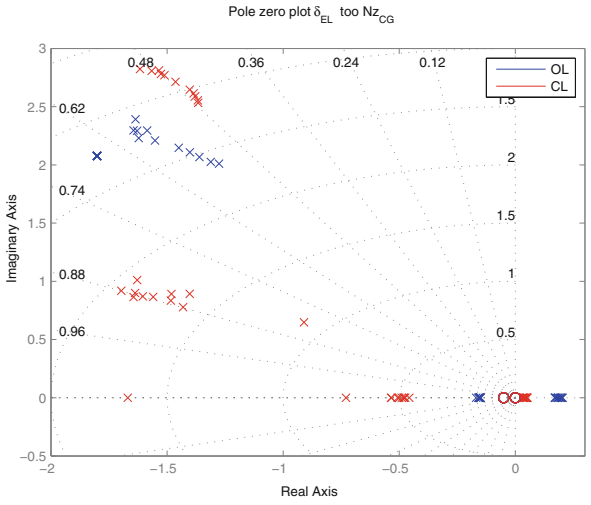

Fig. 6.50 Poles and zeros of Nz_{CG} reference signal to Nz_{CG} output signal channel (10 fueling cases are plotted)

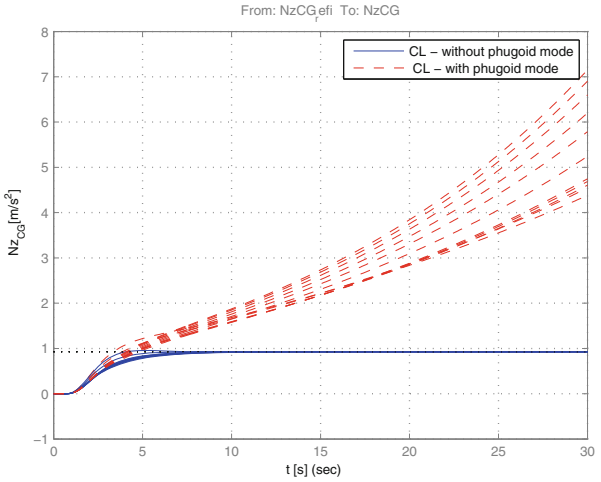

Fig. 6.51 Normal acceleration step response—linear simulation (10 fueling cases are plotted)

The aircraft normal acceleration step response can be seen in Fig. 6.51, where the design plant (without phugoid mode) response as well as the validation plant (with phugoid mode) responses are plotted for all fuel cases (which is one of the robust behavior requirements).

The robustness of control law with respect to unmodeled uncertainty is presented. The uncertainty is here illustrated by diamonds in a Nichols charts, as standard margins or robustness evaluation measures among aircraft controls designers for decades. Uncertainty in this case should be understood as a phase lag and gain variance insensitiveness. One Nichols chart is used for each opened loop (closed loop is disconnected at controller inputs or its output) of the multiple inputs and single-output control law to validate controller robustness. There are different robustness requirements for predefined frequency regions of control law, bounded by phugoid mode frequency (solid line diamond), short-period frequency (dot and dash line diamond) and the first wing bending mode frequency (doted line diamond). First, the robustness is investigated with respect to unmodeled uncertainty at system input, represented by diamonds in a Nichols chart of open-loop transfer function from system δ_{EL} input to controller δ_{EL} output, see Fig. 6.52 and its zoom in Fig. 6.53. One can see that all curves are outside of the prescribed diamonds which guarantees the required robustness.

Similarly, robustness with respect to output unmodeled uncertainty is investigated. The open-loop system has two inputs pitch rate q and normal acceleration Nz (controller inputs) and two measurements of the same notations (plant outputs). Nichols charts of open-loop transfer functions are plotted in Fig. 6.54, and its zoom for Nichols diamonds are plotted in Fig. 6.55.

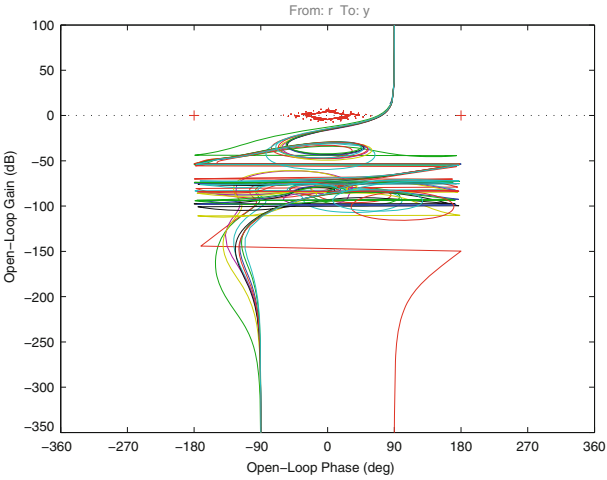

Fig. 6.52 Nichols charts of the closed loops (disconnected at actuators). Ten fueling cases are depicted

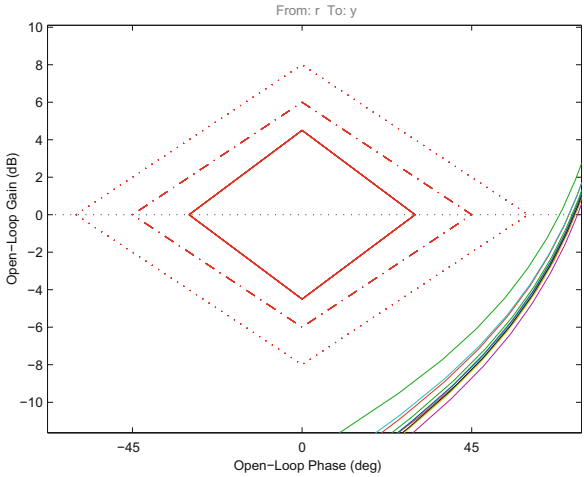

Fig. 6.53 Nichols charts of the closed loops (disconnected at actuators). Ten fueling cases are depicted. Zoomed in for Nichols *diamonds*

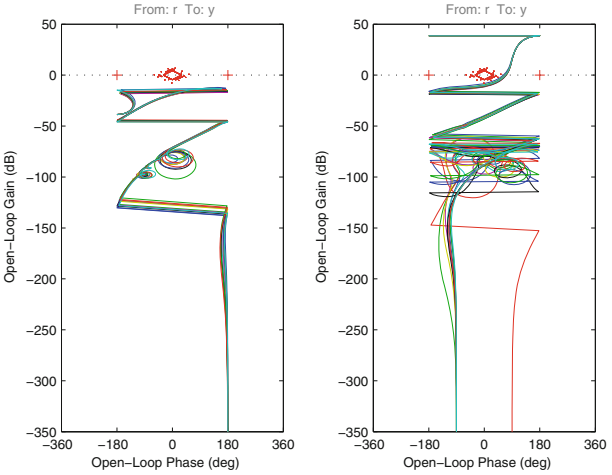

Fig. 6.54 Nichols charts of closed loop disconnected at sensors, pitch rate (*left*) and Nz_{CG} (*right*) (10 fueling cases are plotted)

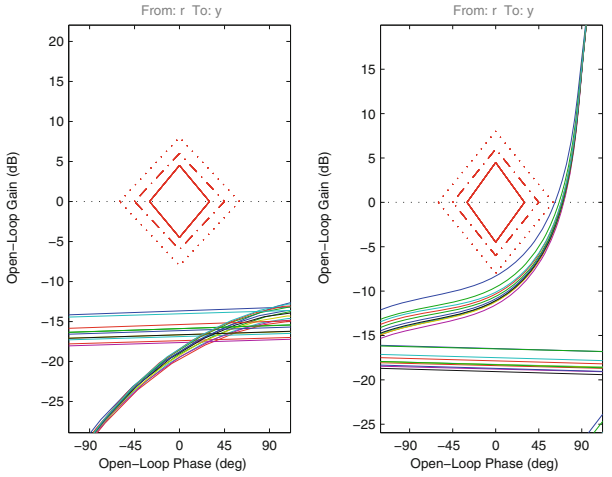

Fig. 6.55 Nichols charts of closed loop disconnected at sensors, pitch rate (*left*) and Nz_{CG} (*right*), zoomed for Nichols *diamonds* (10 fueling cases are plotted)

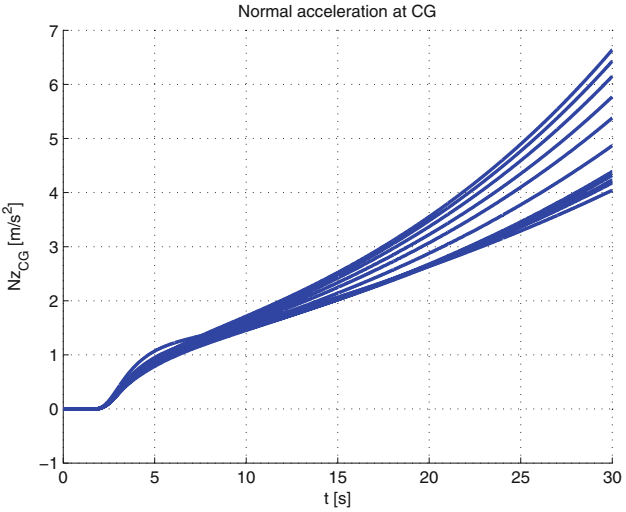

Fig. 6.56 Normal acceleration step response (10 fueling cases are plotted)

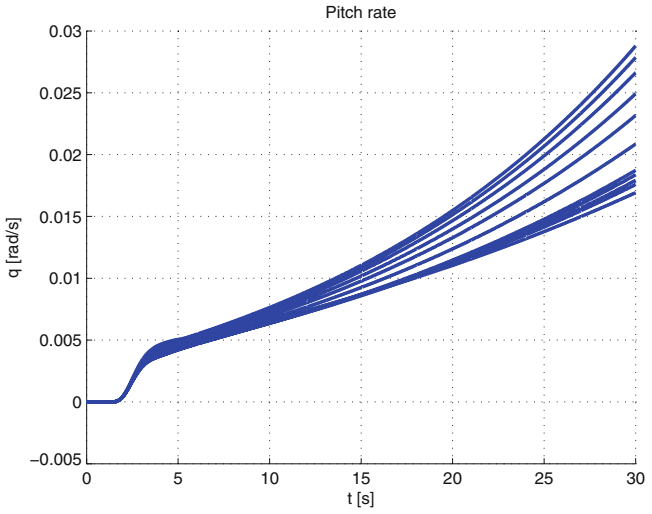

Fig. 6.57 Pitch rate response to step in normal acceleration reference signal (10 fueling cases are plotted)

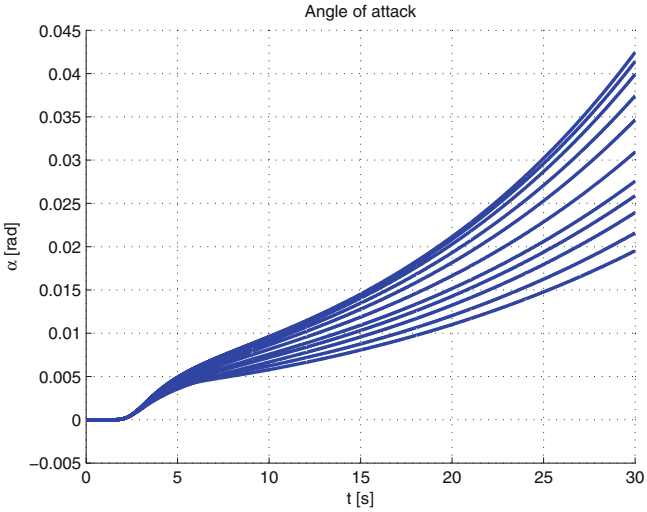

Fig. 6.58 Angle of attack response to step change in normal acceleration reference signal (10 fueling cases are plotted)

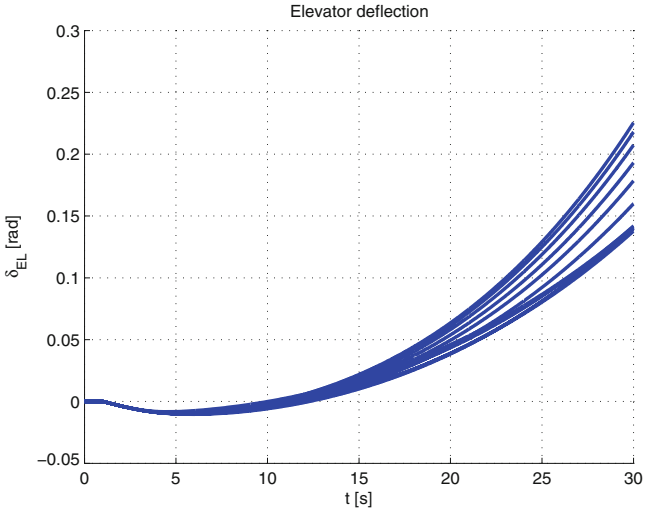

Fig. 6.59 Elevator command induced by step change in normal acceleration reference signal tracking (10 fueling cases are plotted)

Eventually, a MATLAB/Simulink® nonlinear model has been involved. Main sources of nonlinearity come from a fully nonlinear model of actuators, which considers control surface maximal deflections, maximal deflection rates, and aerodynamic effects. All nonlinear simulations are influenced by the unstable phugoid mode, but with a time constant of instability of less than 0.1 s it does not violate control constraints or requirements. Time responses of the aircraft's normal acceleration for all considered aircraft fuel cases are plotted in Fig. 6.56. The pitch rate and angle of attack responses are plotted in Figs. 6.57 and 6.58, again plotted for all considered cases. Finally, control law effort needed for such a maneuver, for all fuel cases, is plotted in Fig. 6.59.

References

1. Alazard D, Apkarian P (1999) Observer-based structures of arbitrary compensators. Int J Robust Nonlinear Control 9(2):101–118
2. Apkarian P, Noll D (2006) Controller design via nonsmooth multidirectional search. SIAM J Control Optim 44:1923–1949
3. Arzelier D, Deaconu G, Gumussoy S, Henrion D (2011) H_2 for HIFOO. In: IFAC world congress on automatic control
4. Balas GJ (2002) Linear, parameter-varying control and its application to a turbofan engine. Int J Robust Nonlinear Control 12:763–796
5. Balas G, Chiang R, Packard A, Safonov M (2010) MATLAB robust control toolbox 3, user's guide. MathWorks
6. Balas G, Doyle JC, Glover A (1991) The mu analysis and synthesis toolbox, Math Works and MUSYN
7. Bates D, Postlethwaite I (2002) Robust multivariable control of aerospace systems. DUP Science, Ios Pr Inc
8. Benatzky C (2006) Theoretical and experimental investigation of an active vibration damping concept for metro vehicles. Dissertation, Vienna University of Technology, Vienna
9. Bennami S, Looye G (1998) Design of flight control laws for a civil aircraft using mu synthesis. In: Proceedings of the AIAA conference on guidance, navigation and control
10. Bing-Fei Wu, Perng Jau-Woei (2004) Gain and phase margin analysis of pilot-induced oscillations for limit-cycle prediction. J Guidance Control Dyn 27:59–65
11. Blakelock JH (1965) Automatic control of aircraft and missiles. Wiley, New York
12. Boyd S, Barrat C (1990) Linear controller design: limits of performance. Prentice Hall, Englewood Cliffs
13. Brockhaus R (2001) Flugregelung (English: Flight control). Springer, Berlin
14. Bryson AE (1994) Control of spacecraft and aircraft. Princeton University Press, Princeton
15. Burke JV, Henrion D, Lewis AS, Overton ML (2006) HIFOO—a MATLAB package for fixed-order controller design and $\mathscr{H}_\infty$ optimization. In: IFAC symposium on robust control design, 2006
16. Burke JV, Lewis AS, Overton ML (2005) A robust gradient sampling algorithm for nonsmooth, nonconvex optimization. SIAM J Optim
17. Burke JV, Lewis AS, Overton ML (2006) Stabilization via nonsmooth, nonconvex optimization. IEEE Trans Autom Control 51:1760–1769
18. Chang Che-Hsu, Hant Kuang-Wei (1990) Gain margins and phase margins for control systems with adjustable parameters. J Guidance Control Dyn 13:404–408
19. Chopra I, Ballardf J (1981) A method for measuring the stability of a full-scale rotor control system. J Guidance Control Dyn

20. Dardenne I (1999) Développement de méthodologies pour la synthèse de lois de commande d'un avion de transport souple. Ph.D. thesis, Ecole Natrionale Supérieure de l'Aéronautique et de l'Espace (SUPAERO), France, 1999. (English: Development of methodologies for control law synthesis for a flexible transport aircraft)
21. Dehkordi VR, Boulet B (2009) Robust controller order reduction. In: Proceedings of the american control conference, pp 3083–3088
22. Delwiche T (2009) Contribution to the design of control laws for bilateral teleoperation with a view to applications in minimally invasive surgery. PhD thesis, Free University of Brussels
23. Demourant F, Ferreres G (2002) A frequency domain identification-control approach for a flexible aircraft. In: IEEE CCA'02
24. Demourant F, Ferreres G (2013) A linear parameter-varying multiobjective control law design based on Youla parametrization for a flexible blended wing body aircraft. In: Progress in flight dynamics, guidance, navigation, control, fault detection, and avionics, vol 6. EDP Sciences, pp 729–748
25. Dotta D, Silva AS, Decker IC (2009) Design of power systems controllers by nonsmooth, nonconvex optimization. In: IEEE power and energy society general meeting
26. Doyle JC (1979) Robustness of multiloop linear feedback systems. In: Proceedings of the 17th IEEE conference decision and control
27. Doyle JC, Mall J, Stein G (1982) Performance and robustness analysis for structured uncertainty. In: IEEE conference on decision and control
28. Doyle JC, Packard A (1987) Uncertain multivariable systems from a state space perspective. In: Proceedings of American control conference, Minneapolis
29. Doyle JC, Packard A, Zhou K (1987) Review of LFT's LMIs and mu. In: Proceedings of 30th IEEE conference on decision and control
30. Doyle JC (1982) Analysis of feedback systems with structured uncertainties. IEE Proc Part D 129(6):242–250
31. Doyle JC, Glover K, Khargonekar PP, Francis BA (1989) State-space solutions to standard $\mathscr{H}_2$ and $\mathscr{H}_\infty$ control problems. IEEE Trans Autom Control 34(8):831–847
32. Evans WR (1948) Graphical analysis of control systems. Trans AIEE 67:547–551
33. Ferreres G, Puyou G (2006) Flight control law design for a flexible aircraft: limits of performance. J Guidance Control Dyn 29(4):870–878
34. Ferreres G, Biannic JM (1998) A μ analysis technique without frequency gridding. In: American control conference. Proceedings of the 1998, vol 4. IEEE, pp 2294–2298
35. Fialho I, Balas G, Packard A, Renfrow J, Mullaney C (1997) Linear fractional transformation control of the F-14 aircraft lateral-direction axis during powered approach landing. In: Proceedings of the American control conference
36. Gawronski W (2004) Advanced structural dynamics and active control of structures. Springer, New York
37. Gu DW, Petkov PH, Konstantinov MM (2005) Robust control design with MATLAB, vol 1. Springer, London
38. Gumussoy S, Henrion D, Millstone M, Overton M (2009) Multiobjective robust control with HIFOO 2.0. In: IFAC symposium on robust control design
39. Gumussoy S, Millstone M, Overton ML (2008) $\mathscr{H}_\infty$ strong stabilization via HIFOO, a package for fixed-order controller design. In: Proceedings of CDC
40. Haddad WM, Chellaboina V (2008) Nonlinear dynamical systems and control: a Lyapunov-based approach. Princeton University Press, Princeton
41. Hanel M (2001) Robust integrated flight and aeroelastic control system design for a large transport aircraft. Number 866 in 8. VDI-Verlag, Düsseldorf
42. Haniš T, Kučera V, Hromčík M (2013) Low order $\mathscr{H}_\infty$ optimal control for ACFA blended wing body aircraft. In: Progress in flight dynamics, guidance, navigation, control, fault detection, and avionics, vol 6. EDP Sciences, pp 671–684
43. Hecker S (2006) Generation of low order LFT representations for robust control applications. PhD thesis, Technische Universität München, Lehrstuhl für Steuerungs- und Regelungstechnik
44. Hyde RA (1995) $\mathscr{H}_\infty$ aerospace control design: a VSTOL flight application. Springer, Berlin

45. Ito H, Ohmori H, Sano A (1993) Design of stable controllers attaining low $\mathscr{H}_\infty$ weighted sensitivity. IEEE Trans Autom Control 38(3):485–488
46. Jeanneau M, Lamolie J, Puyou G, Aversa N (2005) AWIATOR's design of multi-objectives control laws. IFAC
47. Knittel D, Henrion D, Millstone M, Vedrines M (2007) Fixed-order and structure $\mathscr{H}_\infty$ control with model based feedforward for elastic web winding systems. In: Proceedings of the IFAC/IFORS/IMACS/IFIP symposium on large scale systems
48. Kron A, de Lafontaine J, Alazard D (2003) Robust 2-DOF H-infinity controller for highly flexible aircraft: design methodology and numerical results. Can Aeronaut Space J 49:19–29
49. Kureemun R, Bates DG (2001) Aircraft flight controls design using constrained output feedback–a $\mathscr{H}_\infty$ loopshaping approach. In: AIAA guidance, navigation, and control conference
50. Kwakernaak H (2002) Mixed sensitivity design. In: Proceedings of the 15th IFAC world congress, Barcelona
51. Lewis AS, Overton ML (2009) Nonsmooth optimization via BFGS. SIAM J Optim
52. Lewis F (1986) Optimal estimation. Wiley, New York
53. Lewis FL, Vrabie D, Syrmos VL (2012) Optimal control. Wiley, New York
54. Magni J-F (2002) Robust modal control with a toolbox for use with MATLAB. Kluwer Academic Publishers, New York
55. McFarlane D, Glover K, Khargonekar PP, Francis BA (1992) A loop-shaping design procedure using $\mathscr{H}_\infty$ synthesis. In: IEEE transactions on automatic control
56. McRuer D, Ashkenas I, Graha D (1973) Aircraft dynamics and automatic control. Princeton University Press, Princeton
57. Mialon B, Hepperle M (2005) Flying wing aerodynamics studies at ONERA and DLR. In: CEAS Katnet conference on key aerodynamic technologies, Braunschweig
58. Miller JE (1966) Space navigation, guidance and control. AGARDograph
59. Millstone M (2006) HIFOO 1.5: structured control of linear systems with a non-trivial feedthrough. Master's thesis, Department of Mathematics, Courant Institute of Mathematical Sciences—New York University
60. Perkins CD (1970) Development of airplane stability and control. J Aircr 7:290–301
61. Pfifer H, Hecker S (2010) LPV controller synthesis for a generic missile model. In: IEEE international conference on control applications, Yokohama, pp 1838–1843
62. Postlethwaite I, Smerlas A, Walker A, Gubbels AW, Baillie S, Strange ME, Howitt J (1999) $\mathscr{H}_\infty$ control of the NRC Bell 205 fly-by-wire helicopter. J Am Helicopter Soc 44:276–284
63. Pouly G, Lauffenburger J-P, Basset M (2010) Reduced order $\mathscr{H}_\infty$ control design of a nose landing gear steering system. In: 12th IFAC symposium on control in transportation systems
64. Puyou G, Ferreres G, Chiappa C, Menard P (2004) A multiobjective method for flight control law design. In: AIAA guidance, navidation, and control conference, Providence
65. Robu B, Budinger V, Baudouin L, Prieur C, Arzelier D (2010) Simultaneous $\mathscr{H}_\infty$ vibration control of fluid/plate system via reduced-order controller. In: Proceedings of CDC
66. Rugh WJ, Shamma JS (2000) Survey paper: research on gain scheduling. Automatica 36:1401–1425
67. Safonov MG, Chiang RY (1988) Model reduction for robust control: a Schur relative error method. Int J Adapt Control Signal Process 2(4):259–272
68. Scherer C, Weiland S (2004) Linear matrix inequalities in control. Lecture notes. http://www.dcsc.tudelft.nl/cscherer/lmi.html, Accessed 16 May 2014
69. Schirrer A, Westermayer C, Hemedi M, Kozek M (2010) A comprehensive robust control design and optimization methodology for complex flexible-structure systems. In: Proceedings of the 18th mediterranean conference on control and automation, Marrakech
70. Schirrer A, Westermayer C, Hemedi M, Kozek M (2010) LQ-based design of the inner loop lateral control for a large flexible BWB-type aircraft. In: 2010 IEEE multi-conference on systems and control, Yokohama
71. Schirrer A, Westermayer C, Hemedi M, Kozek M (2010) Robust $\mathscr{H}_\infty$ control design parameter optimization via genetic algorithm for lateral control of a BWB type aircraft. In: IFAC workshop on intelligent control systems, Sinaia

72. Schirrer A, Westermayer C, Hemedi M, Kozek M (2011) Multi-model convex design of a scheduled lateral feedforward control law for a large flexible BWB aircraft. In: Preprints of the 18th IFAC world congress, Milano, pp 2126–2131
73. Schirrer A, Westermayer C, Hemedi M, Kozek M (2011) Robust convex lateral feedback control synthesis for a BWB aircraft. In: Preprints of the 18th IFAC world congress, Milano, pp 7262–7267
74. Schirrer A, Westermayer C, Hemedi M, Kozek M (2013) Robust lateral blended-wing-body aircraft feedback control design using a parameterized LFR model and DGK-iteration. In: Progress in flight dynamics, guidance, navigation, control, fault detection, and avionics, vol 6. EDP Sciences, pp 749–766
75. Skelton RE, Stoustrup J, Iwasaki T (2007) The hinf control problem using static output feedback. Int J Robust Nonlinear Control 4:449–455
76. Skogestad S, Postlethwaite I (2005) Multivariable feedback control: analysis and design, 2nd edn. Wiley, New York
77. Stevens BL, Vesty P, Heck BS, Lewis FL (1983) Loop shaping with output feedback. In: American control conference
78. Stevens BL, Lewis FL, Al-Sunni F (1992) Aircraft flight controls design using output feedback. J Guidance Control Dyn 15:238–246
79. Stevens BL, Lewis FL (2003) Aircraft control and simulation. Wiley, New York
80. Tobie HN, Elliot EM, Malcolm LG (1966) A new longitudinal handling qualities criterion. In: Proceedings of the annual national aerospace electronics conference, pp 93–99
81. Torczon V (1991) On the convergence of the multidirectional search algorithm. SIAM J Optim
82. Torczon V (1997) On the convergence of pattern search algorithms. SIAM J Optim
83. Torralba J, Demourant F, Puyou G, Ferreres G (2009) A method for flexible aircraft LFT modelling. In: Proceedings of the European control conference
84. Torralba J, Puyou G, Demourant F (2009) Self-scheduling multiobjective control law design for a flexible aircraft. In: AIAA guidance, navidation, and control conference, Chicago
85. Vanek B (2008) Control methods for high-speed supercavitating vehicles. PhD thesis, Graduate School of the University of Minnesota
86. Vidyasagar M (1988) Control system synthesis: a coprime factorization approach. MIT, Cambridge
87. Wang FC, Chen HT (2009) Design and implementation of fixed-order robust controllers for a proton exchange membrane fuel cell system. Int J Hydrogen Energy 34:2705–2717
88. Westermayer C (2011) 2DOF parameter-dependent longitudinal control of a blended wing body flexible aircraft. PhD thesis, Vienna University of Technology
89. Westermayer C, Schirrer A, Hemedi M, Kozek M (2010) Linear parameter-varying control of a large blended wing body flexible aircraft. In: 18th IFAC symposium on automatic control in aerospace, Nara
90. Westermayer C, Schirrer A, Hemedi M, Kozek M, Wildschek A, Robust $\mathscr{H}_\infty$ flight and load control of a flexible aircraft using a 2DOF multi-objective design. In: Proceedings of 2009 CACS international automatic control conference, Taipei
91. Whorton M, Buschek H, Calise AJ (1996) Homotopy algorithm for fixed order mixed $\mathscr{H}_2/\mathscr{H}_\infty$ design. J Guidance Control Dyn 19:1262–1269
92. Wildschek A, Maier R, Hromčík M, Haniš T, Schirrer A, Kozek M, Westermayer C, Hemedi M (2009) Hybrid controller for gust load alleviation and ride comfort improvement using direct lift control flaps. In: Proceedings of the 3rd EuCASS
93. Wu F (1995) Control of linear parameter varying systems. PhD thesis, University of California, Berkeley
94. Youla DC, Jabr HA, Bongiorno JJ (1976) Modern Wiener-Hopf design of optimal controllers. II. The multivariable case. IEEE Trans Autom Control 21(3):319–338
95. Zhou K, Doyle JC, Glover K (1996) Robust and optimal control. Prentice Hall, Upper Saddle River